



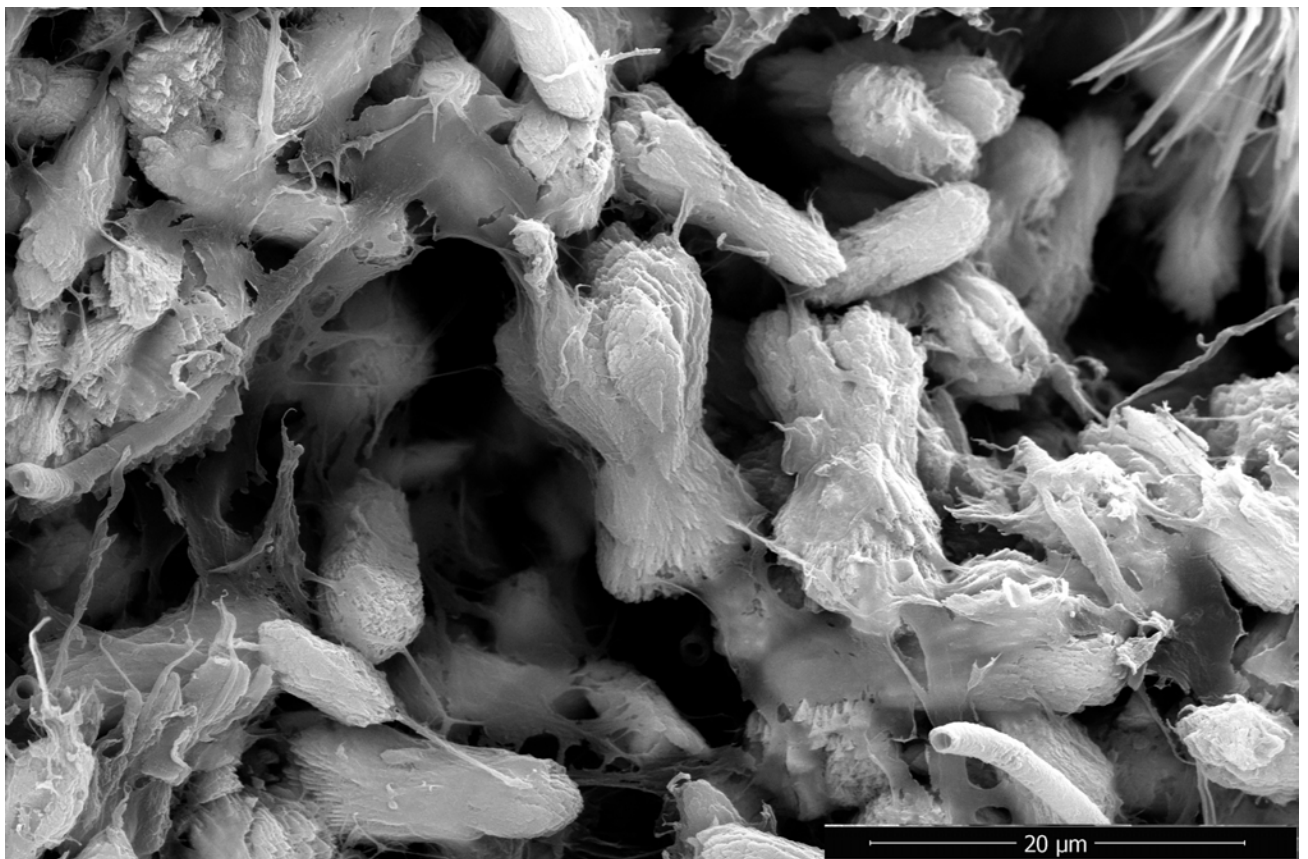
Stockholm
University

Master Thesis

Degree Project in
Geochemistry 60 hp

Early diagenesis, biosignatures and environmental proxies in stromatolitic microbial mat on Eleuthera, Bahamas

Bodil Häggström



Stockholm 2019

Department of Geological Sciences
Stockholm University
SE-106 91 Stockholm

Abstract

Early diagenetic changes in soft sediment can be affected by the presence of microbial communities. The aim of this project is to investigate early diagenetic changes of soft sediment in hypersaline lakes on Eleuthera Island, Bahamas. Sediment cores from two lakes, Big Pond and New Pond, were retrieved and described. Analyses of porewater, lake water, element distribution with depth and distribution of membrane lipids was made to further explore the development from top to bottom of the cores. Sediment profiles from both lakes display altering horizontal layers of organic material, in situ precipitated high magnesium calcium carbonate (Ca,Mg)CO₃ as well as oolitic and bioclastic sand. An early diagenetic feature present in both lakes is the fact that there is the organic matter disappearance with depth: More organic material than mineral matter in the top 10 cm, and less organic material in the bottom parts of the cores. Microbial mats have preserved weather events in the sediment record of the lakes by covering the surface of wind derived sediment. There is at least one of the thick carbonate sand layers that represents one single weather event in New Pond (hurricane deposit). The bottom surface of Big Pond is covered by a microbial mat that is unconsolidated and cannot carry an adult person's weight, while in New Pond the microbial surface is sturdy enough to walk on. The precipitation style in the sediment of the two lakes differ: In Big Pond the precipitates show an alternation between dense patches of high (Ca,Mg)CO₃ content (forming thin horizontal semi-coherent crusts) and mostly porous organic layers of varying thickness with low (Ca,Mg)CO₃ content. The carbonate precipitate in the dense patches show no visible crystalline structure (possibly amorphous) while the low carbonate content areas contain rods and dumbbell-shaped morphologies. Gypsum precipitation is only found in a few well-defined layers close to the surface with gravel-sized crystal clusters. In New Pond the precipitates are dominated by rods and spherulites. The denser areas contain clusters of rods and spherulites rather than non-crystalline (Ca,Mg)CO₃. There are no well-defined gypsum layers, but microscopic gypsum crystals are found at all depths.

Lake water chemistry differs too: Elemental concentrations in Big Pond are approximately twice that of New Pond. Porewater chemistry analyzed in two cores of Big Pond shows different patterns, indicating that pore water is heterogeneously distributed and mobile in a relatively porous sediment. Membrane lipids analyzed in New Pond sediment show an overall tendency of increasing occurrence with depth. Correlation tables of core scanning XRF-data from the two lakes show that there are overall more correlations of elements in New Pond than in Big Pond sediment.

In general, this study seems to indicate that although the two lakes are geographically very close to each other and present similar organosedimentary deposits, the evolution of the sediment at depth is relatively different. In Big Pond, no important alteration of the initial precipitate (at the top of the mat) seems to occur during the burial process (very early diagenesis). No dissolution, recrystallization, or additional precipitation have been observed at depth. In New Pond, the initial precipitation seems to have been influenced by further clustering of the initial crystals and further outgrowths during burial. The reason why the style of early diagenesis is different in between these lakes are not fully understood and will be the subject of further study. One possible explanation for differences in water chemistry and precipitation style, despite close proximity of the two lakes, could be different recharge ratio of ocean vs fresh water in the two lakes.

Abstract	II
Contents	III
1. Introduction	1
1.1 Project aims	1
2. Background	2
2.1 Geological setting	2
2.2 Eleuthera Island	5
2.3 Big Pond	6
2.4 New Pond	6
2.5 Microbial mats	7
2.5.1 <i>The microbial community</i>	7
2.5.2 <i>Extracellular organic matter (EOM)</i>	8
2.5.3 <i>Microbialites</i>	9
2.5.4 <i>Microbialite formation in Big Pond and New Pond</i>	10
2.6 Environmental proxies	10
2.6.1 <i>GDGT's</i>	10
2.6.2 <i>Elemental proxies</i>	11
3. Material and methods	11
3.1 Material	11
3.1.1 <i>Big Pond 2015</i>	11
3.1.2 <i>Big Pond and New Pond 2018</i>	11
3.1.3 <i>Sample sites</i>	12
3.2 Methods	12
3.2.1 <i>Microscopy</i>	12
3.2.2 <i>Fieldwork</i>	13
3.2.3 <i>Porewater sampling</i>	14
3.2.4 <i>Porewater DIC analysis</i>	14
3.2.5 <i>Core splitting and subsampling</i>	15
3.2.6 <i>X-ray fluorescence (XRF)</i>	15
3.2.7 <i>Scanning Electron Microscopy (SEM)</i>	15
3.2.8 <i>Lipid extraction</i>	15
3.2.9 <i>HPLC-APCI-MS</i>	16
3.2.10 <i>Analyses of anions and cations</i>	17
3.2.11 <i>Radiocarbon dating</i>	17

4. Results	18
4.1 Sediment core descriptions	18
4.1.1 <i>Core description C7A, Big Pond 2015</i>	20
4.1.2 <i>Detailed description of top and bottom part of core C7A</i>	21
4.1.3 <i>Core description NP18, New Pond 2018</i>	31
4.1.4 <i>SEM subsamples from NP18</i>	33
4.1.5 <i>Porewater chemistry, Big Pond core C3 (2015) and Big Pond core B2 (2018)</i>	39
4.2 ITRAX data	42
4.2.1 <i>Core BPC7A</i>	42
4.2.2 <i>Core NP18B</i>	45
4.3 GDGT results and correlations	49
4.4 Surface water chemistry	57
5. Discussion	58
5.1 Macroscopic diagenetic changes	58
5.2 Precipitation styles	58
5.3 The role of microbial mats in early diagenesis	59
5.4 GDGT's and degradation of OM	61
5.5 Lake water chemistry vs recharge	61
5.6 Porewater and ITRAX	63
5.7 Role of lake water chemistry for precipitation	65
6. Conclusions	68
Acknowledgements	69
References	70
Appendices	74
A) <i>Elemental ITRAX data from core BPC7A and NP18B</i>	74
B) <i>Complementary backscatter electron images from NP18B</i>	80
C) <i>The alkalinity engine</i>	86
D) <i>Islay freshwater stromatolite</i>	88

1. Introduction

A microbial mat or biofilm is a benthic ecosystem, which comprise a community including several different types of microbes, mainly prokaryotes, embedded in a matrix of extracellular organic matter (EOM) (Dupraz et al., 2009). These microbial ecosystems are strongly influencing most element cycling at the surface of the Earth and have greatly changed the geochemical condition of this planet over time, exemplified by production of free oxygen and hydrogen and fixing nitrogen (Dupraz et al., 2009). They do also affect sediment deposition and precipitation patterns in the basins they live in by trapping and binding particles and acting as cation sponge, as well as through passive and active control of microenvironmental chemistry by different metabolic processes (Dupraz et al., 2011). Microbially induced sedimentary structures (MISS) in soft sediment can be preserved and end up in the hard rock record called microbialites (Noffke et al., 2013), and when they are displaying lamination they are classified as stromatolites (Dupraz et al., 2011).

Microbial mats are regarded as the first ecosystems on Earth, and although some authors hold forward the possibility of abiotic origin of the laminated structures, there is evidence of the biogenicity of 3.5 Ga stromatolites. (Dupraz et al. 2009, Noffke et al., 2013). Evolution of more advanced life at the end of the Precambrian brought forth grazing and burrowing organisms that can disturb the development of microbial mats, and thus largely restrict stromatolite formation to settings that are hostile to many other life forms (extreme environments; Dupraz et al, 2009). Modern hypersaline lakes are examples of such type of setting (Dupraz et al., 2011), an environment that is plentifully represented in the many saline lakes on the carbonate islands of the Bahamian archipelago. Stromatolites can also form in freshwater as travertines (Pentecost 2005), where it is the

result of CO₂ degassing at cascades and waterfalls leading to calcite precipitation. Photosynthetic uptake of CO₂ can play a role in calcite precipitation in slow running and low-DIC (dissolved inorganic carbon) streams (Arp et al., 2001). An example of that is miniature stromatolites in a small freshwater spring on Islay, Scotland. A comparative study of these stromatolites is provided in appendix D.

A rich record of literature exists on the formation of modern and fossil microbialites (See Review in Riding 2011, Dupraz et al. 2009, 2011). However, little is known on the transition from modern systems to the fossil record, especially the very early stages of diagenesis. How does this early filter alter the original signal recorded in the initial precipitates, and how much these early processes (right after sedimentation) influence the following diagenetic steps (deep diagenesis)? These questions are extremely important when looking for biosignatures in the fossil record or on other planets. Here, we look at this early diagenetic window by studying two Bahamian lakes that record a long evolution of stromatolitic deposition (over 1000 years). The work is exploratory. Instead of focusing on one specific marker, a wider range of methods are applied in order to address the question from various angles. The work does not go into great detail of each result in the discussion, but rather aims to represent a road map for future work ahead.

1.1 Project aims

The overall aim of the project is to add knowledge of how the original precipitates in microbial mats are affected by early diagenesis. This is done by describing how stromatolitic microbial mats are affected by the very early stages of diagenesis in two saline lakes on Eleuthera, Bahamas. Descriptions are based on physical appearance, optical and electron microscopy, geochemical data, biomarker

data and lake water geochemistry. The goals are to:

- 1) Determine what diagenetic changes are present along an organosediment core.
- 2) Understand the possible role of microbial mats in these early diagenetic changes.
- 3) Relate the lake geochemistry to the sediment development.

2. Background

2.1 Geological setting

The Bahamas comprise an area of 300 000 km² of the carbonate platform archipelago south of Florida in the western North Atlantic Ocean. 136 000 km² are characterized by shallow banks and 11 400 km² is subaerial land distributed over 29 larger islands, hundreds of small islands and thousands of rocks (James, 1997). The Florida Strait and the Gulf stream effectively cuts off any sediment input from North America and the Greater Antilles, so that the Bahamas platform entirely comprises carbonate (James, 1997). The 5-10 km thick carbonate deposit banks started to form during Late Jurassic upon the tilted fault blocks of Jurassic volcanoclastic crust that got rifted during the opening of Atlantic Ocean in the northwest; and upon oceanic crust in the southeast area (James, 1997). There is a transition from skeletal and reef carbonates to oolitic and eolian carbonates between Pliocene (5.33-2.58 Ma) and Quaternary (2.58- present) deposits (James, 1997). The Quaternary deposits are 24-40 m thick (James, 1997) and comprises three main units, which are exposed on Bahamas today (Myrloie & Carew, 1995). The units are separated by erosional surfaces with or without paleosols (Myrloie & Carew, 1995). Reef growth occur on platform slopes and ooids are produced where cool CO₂-rich oceanic water and warmer bank water with aragonite supersaturation can mix; thereby ooid production is associated

with high ocean levels as illustrated by Kindler & Hearty (1996) (Fig.1).

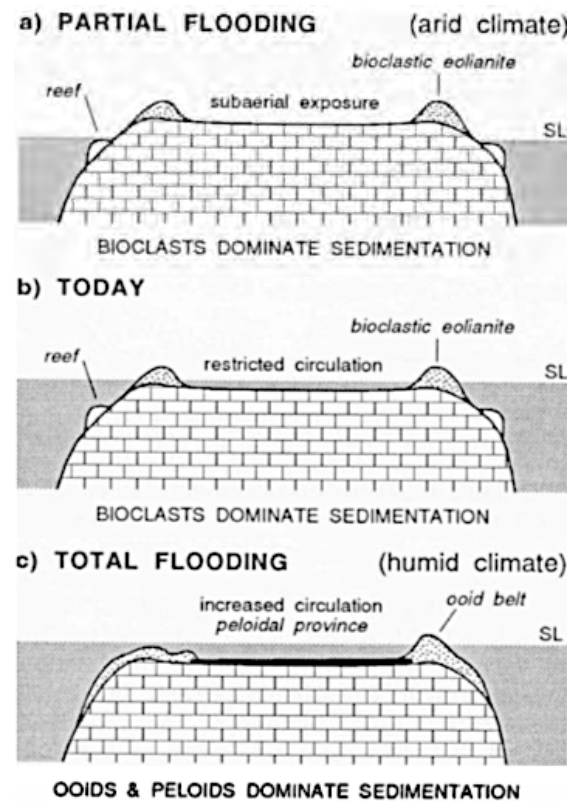


Figure 1: Model by Kindler and Hearty (1996) illustrating the impact of sea level change on carbonate grain composition.

The formation of the units exposed on the Bahamas today started during the late Pleistocene when several intervals of glaciation made the sea level fluctuates between high and low stands (James, 1997). The last interglacial stage with higher sea level than today occurred at ~125 ka (James, 1997). Supratidal (eolian), intertidal and subtidal carbonate deposits all form during transgressive, standstill and regressive phases (Myrloie & Carew, 1995).

During the last glacial low-stand, 17 000 BP, the sea level was 120 m below present sea level (Moore & Wade, 2013). The low sea level will expose the carbonate platform, leading to lithification (cementation) and dissolution processes (James, 1997).

When unconsolidated carbonate deposits emerge above sea level, the deposits are affected by meteoric water (Moore & Wade, 2013). Meteoric water is often undersaturated with respect to carbonates and will thereby dissolve carbonate rock and sediment at contact surfaces (Moore & Wade, 2013). On a carbonate island this meteoric water forms a fresh water lens that floats on top of marine water within the sediment (Moore & Wade, 2013, Mylroie & Carew, 1995). Below the water table in the phreatic zone all pore space is filled with water, while in the vadose zone above the pore space is only partially filled by water (Moore & Wade, 2013). Water moves through the vadose zone either by seepage through pores space or flow in solution channels, large fractures or sinkholes (Moore & Wade, 2013). As the water gets more and more saturated while percolating through carbonate sediment pore space; it can eventually lead to precipitation and cementation of carbonate grains (Moore & Wade, 2013). Both dissolution and precipitation activity most effective in a zone centered on the water table where water-sediment interaction is highest, which make the water table the center of diagenetic activity (Moore & Wade, 2013). The sediments of the Bahamian islands are composed mainly of aragonite and magnesian calcite (Moore & Wade, 2013). Mg-calcite is around 10 times more soluble and aragonite is twice as soluble than calcite (Moore & Wade, 2013). Where there is a mix of different carbonates, meteoric water will therefore substantially alter the porosity since the water cannot equilibrate with the surrounding rock until the more soluble phase is completely dissolved

(Moore & Wade, 2013). As Mg is replaced by Ca in the rock, diagenetic water will get a high Mg/Ca ratio downstream (Moore & Wade, 2013). When Mg-calcite is dissolved; aragonite will start dissolve and give an increased Sr/Ca ratio downstream (Moore & Wade, 2013). Where a rock is made of pure calcite the meteoric water will soon equilibrate with the surrounding rock and not alter the porosity as much as in a chemically heterogenous rock (Moore & Wade, 2013).

The modification of a landscape due to dissolution of carbonate rock is called karst formation (Mylroie & Carew, 1995). The weathered surface zone of carbonate rock is called epikarst and includes loose rocks and soil, and dissolution patterns on cm to m scale in the carbonate rock of the epikarst is called karren (Mylroie & Carew, 1995). Holes and tubes formed by dissolution leads meteoric water down into the underlying sediment/rock (Mylroie & Carew, 1995). Where meteoric water is collected in the epikarst, some holes can develop into vertical shafts called pit caves (Mylroie & Carew, 1995). Caves that develop on top of the freshwater lens are called phreatic caves (Mylroie & Carew, 1995). When sea level and freshwater lens lowers, these caves are left empty (Mylroie & Carew, 1995). Abandoned phreatic caves that have collapsed can collect a lot of soil and be ideal to plant crops in, why they are named banana holes by Bahamian residents (Mylroie & Carew, 1995). The relation of sea level, fresh water lens and karst features are illustrated in figure 2.

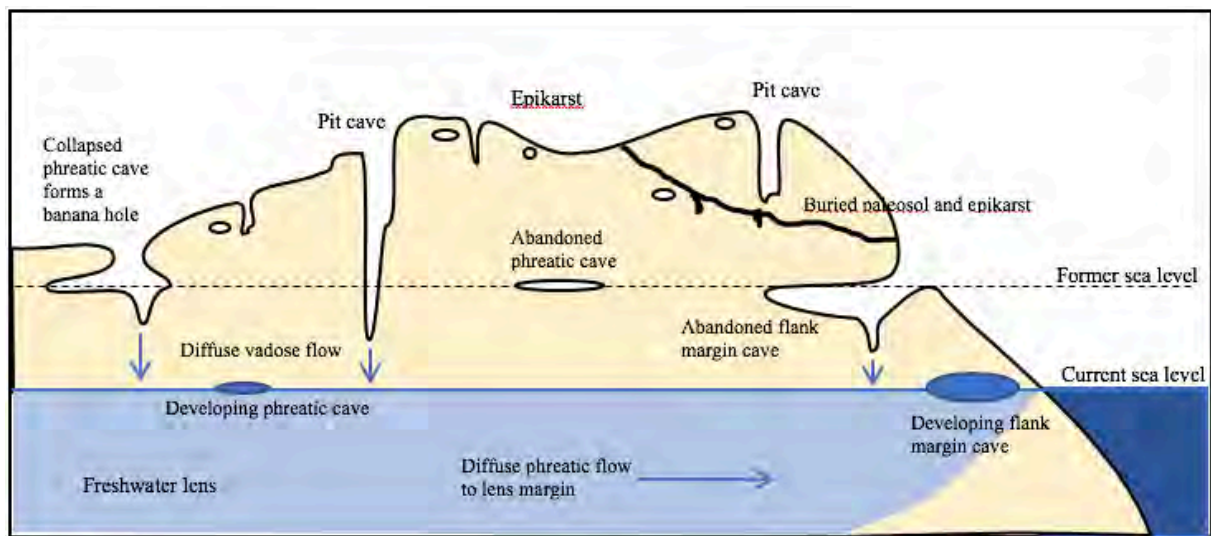


Figure 2: Schematic illustration of the relation of sea level, fresh water lens and karst development on a carbonate island. After illustration in Mylroie & Carew (1995).

Where fresh water and marine water mix in the rock, flank margin caves can develop (Mylroie & Carew, 1995). The size of the fresh water lens is depending on amount of rainfall, the size of the island and the porosity of the rock which determines the hydraulic conductivity (Moore & Wade, 2013a). The shape of fresh water lens is affected by differences in permeability of rocks (Mylroie & Carew, 1995). Lakes that forms in the depressions between ridges are often hypersaline due to evaporation that exceeds the precipitation or the seepage from open sea (Mylroie & Carew, 1995). Under such lakes the marine water can “cone” up underneath the freshwater lens and with further evaporation the water becomes more saline than sea water (Mylroie & Carew, 1995). When a lake is connected to the ocean by cave systems or conduits, the exchange of water from tidal pumping can keep the salinity near marine salinity (Mylroie & Carew, 1995).

The topography of the Bahamian islands is characterized by lithified dune ridges, commonly reaching an elevation of 30 m.a.o., with a peak elevation of 63 m on Cat Island, and lowland areas are mainly comprised of intertidal and subtidal

deposits (James, 1997). Radiometric dates from the fossil reefs in these deposits indicate that they formed during the last interglacial ocean level high stand (James, 1997). All intertidal and subtidal deposits exposed today and their contemporary eolianites are mainly oolitic in composition (Mylroie & Carew, 1995). Exposed deposits from earlier sequences of ocean level high stands are confined to eolianites because they form topographic highs, while intertidal and subtidal deposits from earlier ocean level high stands are not exposed since some earlier high stand did not reach higher than present sea level and due to slow platform subsidence (Mylroie & Carew, 1995). Substantial areas of the islands are covered by tidal creeks and lakes, of which many are hypersaline.

The Bahamian archipelago lies within the North Atlantic hurricane belt and have a tropical marine climate with a gradient of wetter and cooler to the northwest and drier and warmer to the southeast (Whitaker & Smart, 1997). The trade winds bring rain in the summer season while the winters are drier (Whitaker & Smart, 1997).

2.2 Eleuthera Island

Eleuthera is a long and narrow island located at the east edge of the Bahamas platform (Fig.3) and have a steep and narrow shelf towards the Atlantic Ocean (Kindler & Hearty, 1997). The island is thereby directly exposed to winds and waves from the open sea (Kindler & Hearty, 1997). Eleuthera has an annual mean precipitation of 1000-1250 mm (Whitaker & Smart, 1997). One estimate of the annual evapotranspiration on the Bahamas is 1150 mm though there are estimates as low as 540 mm for the southern islands (Whitaker & Smart, 1997). The main aquifer host rocks of the Bahamian islands belong to the Pleistocene formations which have a high hydraulic conductivity due to secondary porosity caused by dissolution (Whitaker & Smart, 1997). The rocks have a varying permeability with vug space and channels in the size range <1mm to 10 cm, and horizontal continuous channels and caverns produced by subaerial discontinuities and paleo water tables (Whitaker & Smart, 1997). The laterally continuous channels and caverns are suggested as the primary controls of hydraulic conductivity by Whitaker & Smart (1997).

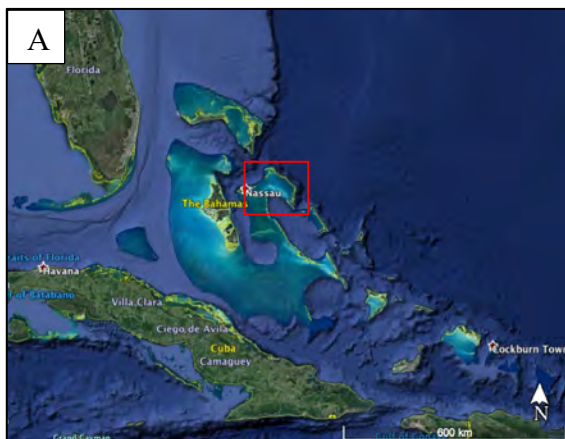


Figure 3: A) The Bahamas with a red inset showing the location of Eleuthera Island (Google Earth, 2018b). B) Eleuthera Island with red inset showing the location of Big Pond and New Pond (Google Earth, 2018b). C) The study sites Big Pond and New Pond on south Eleuthera (Google Earth, 2019a).

2.3 Big Pond

Big Pond is located on the southern end of the Eleuthera Island in Bahamas, (location Fig. 3, view from sampling site Fig.4). The lake stretches 2 km in N-S direction and have an elongated tip that is ca 45 m wide with an average depth of 1.20 m to the north, widening out to the south where the broadest part of the lake is 400 m wide and 0.3-0.8 m deep (Glunk et al., 2011). The distance to the east ocean shore at the north end is approximately 170 m and at the wide middle part approximately 550 m. A peninsula in the southern part leaves only a narrow and shallow (0.15 m deep) plateau connecting the southern basin to the rest of the lake (Glunk et al., 2011). The whole lake bottom is covered by microbial mats in the main basin, displaying different morphologies (e.g., “snake-like” and flat; Glunk et al., 2011). Water salinity and turbidity varies seasonably (Glunk et al. 2011). The southern basin is the deepest part of the lake (2m), where gypsum precipitation covers the sediment (Glunk et al., 2011). During fieldwork in November 2018, this part of the lake had clear water down to approximately 70 cm depth, below the water was turbid and had a blue color. The area close to the shore was approximately 40 cm deep and covered with flat microbial mat and gypsum. The gypsum cover was fine at the shallow part and became coarser grained with depth. In the deeper parts of the south basin there are karst formations of which the top parts were reachable from the surface, approximately at 40-50 cm depth, while the bottom parts were not visible from above due to the turbid water below 70 cm. The reachable

parts were covered with 5-10 cm of red microbial mat and gravel-sized gypsum grains.

A narrow rim (<2m) of the lake experiences seasonal desiccation while the remainder of the lake is water covered all year (Glunk et al., 2011). The water in Big Pond is clear with good light conditions at the bottom except at heavy rainfalls when the water becomes more turbid (Glunk et al., 2011). The salinity of the surface water varies between a minimum 80 PSU (average 132 PSU) during the wet season and a maximum 240 PSU (average 209 PSU) during the dry season (PSU = practical salinity units; g salt per liter solution) (Glunk et al., 2011). The bottom waters typically have an increase of 40 PSU compared to the surface waters and in dry season the southern basin is 40 PSU higher than the northern end of the lake (Glunk et al., 2011).

2.4 New Pond

New Pond is smaller than Big Pond with the northern end approximately 130 m south of Big Pond (location Fig.3, view from sampling site Fig. 4). The lake has no official name but is referred to as New Pond in this project. New Pond is 270 m in NNE-SSW direction; 170 m wide at the northern part and 95 m wide at the southern part. The southern end is 70 m from the south ocean shore of Eleuthera. Based on map image view color difference, the lake covers an area of approximately 110 x 125 m. The bottom is covered with microbial mat that is sturdy enough to walk on. The salinity was 84 PSU, which is approximately half of Big Pond salinity at the same day of sampling.



Figure 4: Big Pond (left) and New Pond (right). Middle: Microbial mat layering of the sediment, New Pond (top) and Big Pond (bottom).

2.5 Microbial mats

2.5.1 *The microbial community*

Three main components are required for a microbial community to function; how they are achieved depend on metabolic strategy (e.g., Dupraz et al., 2011):

- 1) Energy; received either from light (photo-) or chemical redox reactions (chemo-).
- 2) Electron donors to generate energy within the cells; either organic (organo-) or inorganic (litho-)
- 3) Carbon to form biomass; either by CO₂ fixation (autotrophy) or from consumption of already fixed carbon (heterotrophy)

Microbial communities in the studied hypersaline lakes can be classified into

several groups with different metabolic strategies and are often distributed along a geochemical gradient; oxygenic phototrophs (cyanobacteria), aerobic heterotrophs (aerobic respiration), anoxygenic phototrophs (green and purple sulfur bacteria), anaerobic heterotrophs (anaerobic respiration, mostly sulfate reducing bacteria), sulfide oxidizers (chemolithotrophs), fermenters (Dupraz et al., 2009). Each group takes advantage of other groups metabolic products in a well-organized community leading to a very efficient element cycling within the microbial mat (Fig. 5).

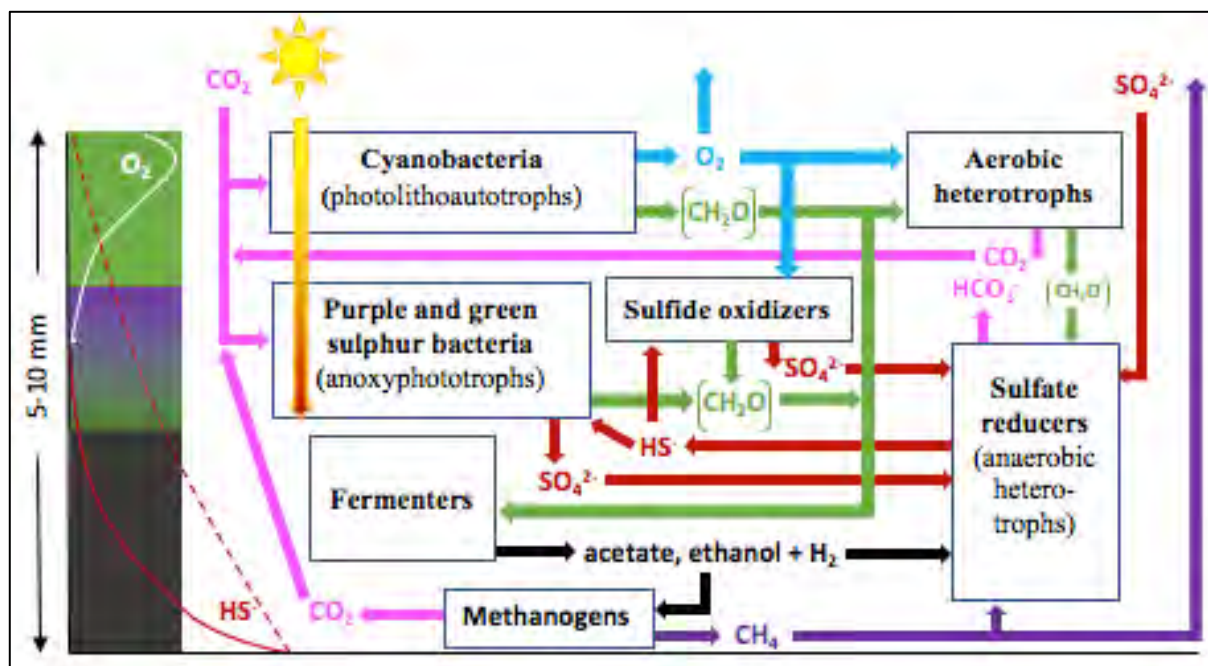


Figure 5: Simplified vertical profile and flow-scheme example of the metabolic pathways in a microbial mat. The vertical profile shows the different layers as described in text (2.5.1). During the night when there is no oxygen production; the sulfate reducing (HS^- producing) process begins higher up, marked by the dashed red line. CH_2O -notations refers to complex organic molecules (large font size) and simpler organic molecules like alcohols and fatty acids (small font size). The figure is based on figures and information in Dupraz et al. (2009) and Warren (2016).

Key for organism-describing words: (*photo-*) = Photosynthesizing, (*-litho-*) = dependent on inorganic compounds, (*-autotrophs*) = making their own organic carbon, (*aerobic*) = dependent on oxygen, (*heterotrophs*) = feeding on organic carbon made by other organisms, (*anoxyphototrophs*) = photosynthesizing with other oxidizing compound than oxygen (Warren, 2016)

Light availability is the key component for the internal organization of the microbes and Dupraz et al. 2009 describes the typical succession of bacterial groups within these hypersaline mats: The upper 1-2 mm have sufficient light for photoautotrophs; i.e. cyanobacteria. Since the cyanobacteria are the main CO_2 -fixation organisms, this layer also contains heterotrophic bacteria that feed on the organic matter produced. Noteworthy is that not only aerobic heterotrophs but also anaerobic heterotrophs such as sulfate reducers and methanogens can be found in this upper layer. Below is often a layer of purple sulfur bacteria and under that green sulfur bacteria (both anoxygenic photosynthetic bacteria) and a deeper black, sometimes grey-striped layer. The black color is due to sulfide (provided by initially high content of

organic material that have supplied sulfide production) and the grey stripes contain less organic material and more sediment. Major elements are generally very efficiently recycled within the mat so that the mat in practice only need sunlight for the community to function (Dupraz et al., 2011).

2.5.2 Extracellular organic matter

The extracellular organic matter (EOM) comprise extracellular polymeric substances (EPS) and soluble microbial products (SMP). The EPS is a solid substance that is produced by several types of microbes and serve as a framework matrix in which the microbes are protected from external environmental impact such as desiccation, UV-radiation and varying hydrodynamic circumstances (Dupraz et

al., 2009). Microenvironments in the EPS matrix enables for different types of bacteria to live in close proximity despite very different chemical environment preferences; such as oxygen sensitivity in an oxygen-rich area of the mat (Dupraz et al., 2009).

The exopolymer matrix also works as a host of nucleation sites for mineral precipitation in microbial biofilms (Arp et al., 2001, Dupraz et al. 2009). The acidic groups (negatively charged functional groups, e.g., carboxyl, thiols, amine groups) found within EPS can bind cations such as Ca^{2+} and Mg^{2+} (Arp et al., 2001). Biofilm EPS is not orderly arranged and therefore the acidic groups are not orderly distributed, why nucleation sites only occur randomly in the EPS (Arp et al., 2001).

Different estimations of the capacity of EPS to bind Ca^{2+} shows a variation of 53-183 mg Ca /g EPS (Dupraz et al., 2009). EPS produced by sulfate reducing bacteria show a tendency to attract iron cations; suggested by Braissant et al. (2007) to be due to the abundance of sulfur groups, which have a strong affinity for iron.

The negative charge is a result of deprotonation of functional groups at increasing pH; of which sulfate groups ($\text{R-O-SO}_3\text{H}$) and carboxylic acids (R-COOH) have over all lowest pK; 2,5 and 1-5 respectively; and is thereby considered most important as binding sites for metal ions (Dupraz et al., 2009).

Approximately 50 % of the organic matter degradation in a microbial mat is performed by aerobic heterotrophs and 50% by anaerobic heterotrophs, the latter mainly by sulfate reducing bacteria (SRB) (Dupraz et al., 2009). Aerobic heterotrophs and fermenters degrade the large molecules of EPS to low molecular weight organic carbon (LMWOC) which can then be further degraded by sulfate reduction and methanogenesis (Dupraz et al., 2009)

2.5.3 *Microbialites*

Organosedimentary deposits that are resulting from sediment trapping, binding and mineral precipitation by benthic microbial communities display different structure: laminated (stromatolites), clotted (thrombolites), structureless (leiolites) or dendritic (dendrolites) (Dupraz et al., 2011). For these microbially induced sedimentary structures to be preserved in the rock record as a microbialite, early lithification is crucial. Direct preservation of the organic matter is rare, though specific structures, organic biomarkers and stable isotope fractionation can serve as indirect evidence to prove the biogenicity of the microbialites (Dupraz et al., 2011).

The alkalinity engine and the organic matrix (EOM) where mineral precipitation takes place are the key components in the lithification process (Dupraz et al., 2011). The alkalinity engine can be extrinsically driven by evaporation, degassing and alkaline water input where precipitation initiates in/at the outer parts of the mat (Dupraz et al., 2009). This is called microbially influenced precipitation, where the microbes are not directly inducing precipitation, but the organic matrix are affecting the mineralogy and morphology of the deposit (Dupraz et al., 2011). The alkalinity engine can also be intrinsically driven; the microenvironments in the microbial community are controlled by the microbes' metabolism which affect the alkalinity engine so that precipitation might occur from within the mat (Dupraz et al., 2011). This more direct involvement of microbes is called microbially-induced precipitation (Dupraz et al., 2011). Several types of carbonate minerals can precipitate in microbial mats; including aragonite, calcite, monohydrocalcite, vaterite, high Mg-calcite to Ca-dolomite (Dupraz et al., 2009). The metabolic rates in microbial mats are very high which creates a dynamic geochemical environment where minerals can both precipitate and be dissolved

(Dupraz et al., 2009). The balance between metabolic processes that increase and decrease alkalinity is what eventually determines whether microbially induced precipitation occurs or not (Dupraz et al., 2009). For details on alkalinity, see appendix C) *The alkalinity engine*.

2.6 Microbialite formation in Big Pond and New Pond

Microbialite formation is an ongoing process in the two lakes and have been for approximately 1200 years in Big Pond. The processes behind the mineralization within the microbial mats have previously been investigated by Glunk et al. (2011)

Even though the bottom water above the mats are supersaturated with respect to calcite, aragonite and dolomite (carbonates), there is no precipitation of these minerals on top of the mat (Glunk et al., 2011). This seemingly contradictory phenomenon is explained by the decrease in calcium ion availability due to coupling to anions in the water column (for example SO_4^{2-}) and the binding capacity of the mat EOM (Glunk et al., 2011). A few mm below the mat surface, underneath the peak zone of photosynthesizing and aerobic respiration where sulfate reduction is at its peak level, high-Mg calcite is precipitated (Glunk et al., 2011).

2.7 Environmental proxies

2.7.1 GDGT's

A small part of the project entailed the analysis of a certain subset of microbial membrane lipids. Branched and isoprenoid glycerol dialkyl glycerol tetraethers (brGDGTs and isoGDGTs) are membrane lipids of certain (sub)groups of bacteria and archaea, respectively. The brGDGTs have branched alkyl core lipids while the isoGDGTs have isoprenoidal core lipids (Sinninghe Damsté et al., 2000, Schouten et al., 2013). The brGDGTs are commonly used as a temperature and pH proxy in soils,

peat bogs, rivers and lakes (Schoon et al. 2013, Schouten et al., 2013). In an investigation of brGDGT distribution in lakes by Schoon et al. (2013), the correlation between alkalinity and brGDGT ($r^2=0.83$) was found to be stronger than the correlation of pH and brGDGT ($r^2=0.72$). The lakes on Eleuthera Island and other Bahamian islands present a wide range of alkalinities and salinities. The fieldwork presented in the method section include a lake survey for a proxy development pilot project. The aim of the pilot project is to investigate to what extent the relative distribution of brGDGTs is related to alkalinity, pH, and possibly salinity, and might be useful in the interpretation of the sedimentary sequences. Approximately 40 lakes on Eleuthera Island and San Salvador were included in the survey. The lake survey results are not a part of this thesis, but initial results of membrane lipid analysis downcore in one lake, New Pond, are presented and discussed.

The alkyl chains are branched by between four and six methyl groups and contain one or two cyclopentyl moieties (Sinninghe Damsté et al., 2000, Schouten et al., 2013). The internal distribution between nine different varieties of brGDGTs vary with changing environments, where the grade of methylation is found to correlate with mean annual temperature (MAAT) changes and the grade of cyclization correlates to pH (Weijers et al., 2007). Different calibrations that relate temperature with the brGDGTs exist, depending on the environment, the most recent one being from African lakes (Russell et al., 2018).

Intact polar lipids (IPL) are the membrane molecules that still have their functional headgroups attached and represent (recently) living organisms, while core lipids (CL) are missing their functional headgroups and are considered to be fossil remnants (Schoon et al. 2013).

Which type of bacteria produce brGDGTs is yet not identified, though the highest abundance is in the anoxic part of peat bogs which indicates that anaerobes could be the main producers (Weijers et al., 2009, Naafs et al., 2017).

2.7.2 *Elemental proxies*

Variations, co-variations and ratios of elements can be used as environmental proxies (Croudace & Rothwell, 2015).

High Ti, Fe, Ti/Ca and Fe/Ca are commonly used as indications of periods of relatively higher input of terrigenous sediment supply, primarily as a proxy of rainfall (Croudace & Rothwell, 2015, Itambi et al., 2009) and aeolian dust input (Xu et al. 2008). Ti is not sensitive to changing redox conditions and is thereby a more reliable proxy for terrigenous sediment delivery than Fe which is redox sensitive (Croudace & Rothwell, 2015).

Organic bromine (Br) compounds are produced by mainly marine organisms; why this element gets concentrated in organic material (Croudace & Rothwell, 2015). Br content of >200 cps in XRF core scanning was used as an indicator of marine vs terrestrial organic material input in a study by McHugh et al. (2008)

Sr is correlated to aragonite precipitation and Mg concentrates more in calcite than in aragonite; Sr and Mg can therefore be used to distinguish aragonite from calcite (Sunagawa et al., 2007). Sr/Ca can be used as a seawater temperature proxy since Sr incorporation in aragonite is temperature dependent (Allison et al., 2001)

Oxidized metals that gets trapped on the microbial mat surface gets buried with time, and when they get below the level of oxygen production and HS⁻ increase they can dissolve and get incorporated in sulfide precipitates like pyrite (FeS₂), in this way the organic matrix can passively

concentrate metals and result in an increase of metal distribution with depth (Sforna et al., 2017). Compared to other metals; the rate of sorption is higher for Zn, Cu and Fe in the redox conditions in this zone (Sforna et al., 2017).

3. Material and methods

3.1 Material

3.1.1 *Big Pond 2015*

Sediment cores from Big Pond were collected and sampled at the Bahamas field trip 2015. This fieldwork was executed by Susanne Sjöberg, PhD at the Department of Geological Science, Stockholm University and Christophe Dupraz, senior lecturer at the Department of Geological Science, Stockholm University. ITRAX data, thin sections and radiocarbon dating made from the core C7A and pore water data from core C3A was used in this project.

3.1.2 *Big Pond and New Pond 2018*

At the Bahamas field trip in November 2018, one sediment core from Big Pond was collected for pore water sampling. One sediment core was collected from New Pond and brought back to Stockholm University. This field trip was part of a pilot project investigating branched GDTG's variability in different alkalinities. The goal was to recover water, sediment and organic material samples from lakes on the Bahamas islands San Salvador and Eleuthera to get a wide range of different alkalinities together with samples to extract organic molecules from. Samples and data from 23 lake sites on San Salvador and 14 lake sites on Eleuthera; including Big Pond and New Pond; were brought back to Stockholm University. Part of the material and data collected for the branched GDTG's is included in this project, primarily the Big Pond and New Pond data but also briefly from other lakes for comparison purposes.

3.1.3 Sample sites

The sites of core and water sampling in Big Pond and New Pond are marked out in figure 6. Site 1a, 1b and 3 are water sample sites from 2018. Site C3, C5, C6 are core sites from 2018 and B2, C, D and NP18 are core sites from 2018.

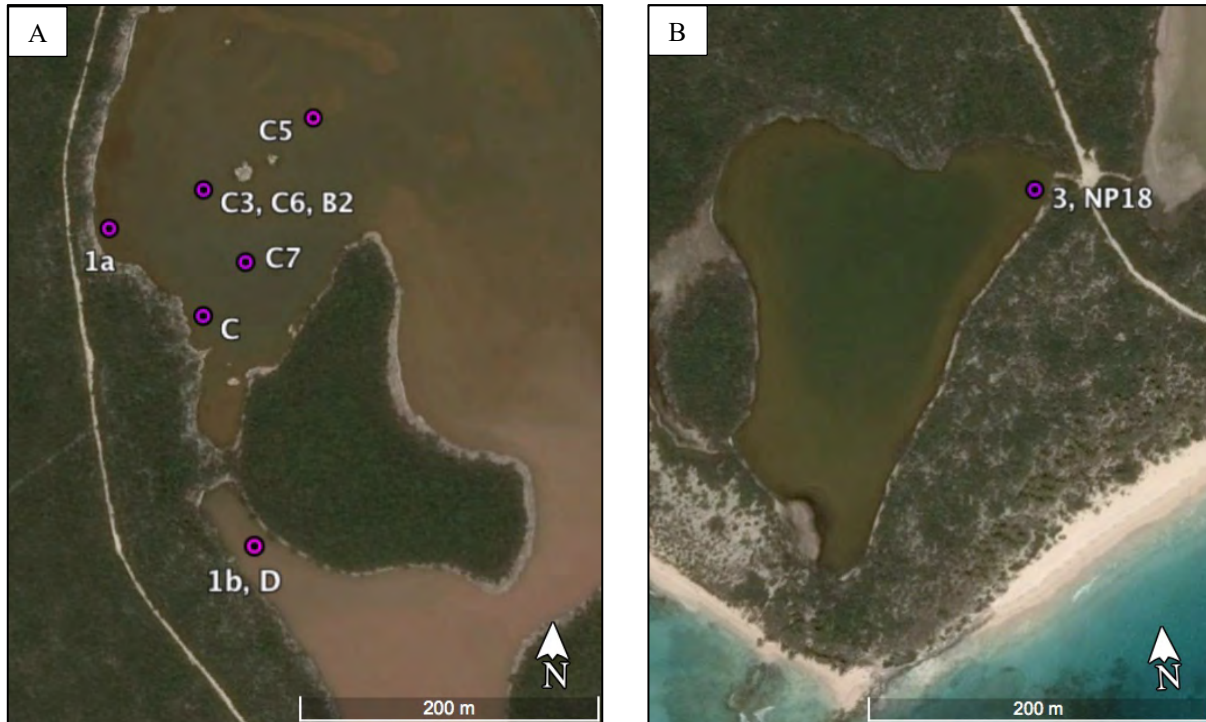


Figure 6: A) Big Pond (Google Earth, 2019c) and B) New Pond (Google Earth, 2019b) sample sites. The numbers mark out the location for water sampling 2018. The New Pond site was named 3 because the lake to the east was sampled as number 2 in the larger project of the field trip 2018. The markings starting with a letter are core sites. The C3, C5, C6 and C7 cores are from the 2015 field trip and the B2, C and NP18 cores are from the 2018 field trip

3.2 Methods

3.2.1 Microscopy

Previously prepared thin sections from core C7A was studied in two different microscopes: An Olympus BX51 microscope with up to 100X magnification at the Department of Palaeobiology, Swedish Museum of Natural History, where the software OLYMPUS cellSens Dimension was used to take photomicrographs; and a Nikon OPTIPHOT2-POL petrographic microscope with up to 40X magnification at the Department of Geoscience, Stockholm University where an attached Leica EC3-01110059601 camera and the software

Leica microsystems LAZ EZ was used to take photomicrographs.

3.2.2 Fieldwork

Fieldwork was conducted in November 2018 and included sampling of sediment cores, water, sediment and organic material from saline lakes on the Bahamian islands San Salvador and Eleuthera. The two sites from which samples are treated in this project are from the sites 1 (Big Pond) and 3 (New Pond). Sediment cores were retrieved by pushing down 45 or 55 cm long polycarbon tubes with 63 mm inner diameter (outer 65 mm) into the lake bottom sediment until hitting hard rock, putting a plug at the top and pull the core up. Another plug is put in the bottom of the core before bringing it over the water surface to keep it

in place. One sediment core from New Pond; named NP18; was brought back to Stockholm University for the purpose of comparing to a previously retrieved core from Bid Pond. One core; named B2; from Big Pond was used for porewater sampling. The polycarbon tube used to retrieve the core for porewater sampling is 65 cm long and has an inner diameter of 64 mm (outer 70mm) with pre-drilled 4 mm holes each cm. Sediment samples was collected with a spatula from the lake bottom and put in sample bags. Where there were microbial mats covering the bottom of the lake; the sediment sample was naturally a piece of microbial mat instead of actual sediment as in the case of Big Pond. Algae, water plant specimen and floating EOM samples was collected at a few lake sites where these were present and put in sample bags. Water samples were retrieved from the lake with a bucket.

Salinity was measured in field with a refractometer, either from a pipette drop directly from the lake surface water or from the bucket. Temperature, pH and conductivity was measured in field with a HI 991300 pH/EC/TDS meter. Both meters were rinsed with deionized water between the different lake sites. At each site unfiltered water was sampled in 50 ml falcon tubes or other containers for field station titration. Care was taken to fill the tubes with as little headspace as possible to avoid loss of DIC through exchange with air in the tube. A 50 ml syringe was used to sample water from the bucket to filter through 0.2 μm membrane filters for lipid extraction. The syringe was rinsed with lake water at each new site before retrieving the sample. The membrane filters were put in pre-numbered cryovials. The filtered water was collected in 1,5 ml glass vials for deuterium analyses and in 10 ml falcon tubes for laboratory alkalinity analyses, 0-3 tubes depending on if there was sufficient amount of water going through the filter. Some samples were too turbid to get more than 1 ml through the membrane filter.

A hand-pumped vacuum filtering unit was used to pump water through a glass-fiber filter for collecting biomass for DNA analyses. The glass-fiber filters were put in prenumbered cryo-vials. A GFF filter (0,7 μm) was used for all samples and for very turbid water a GFA (1,6 μm) filter was used to prefilter the water before GFF filtering. The filtered water was filled in 1-2 50 ml falcon tubes and/or 1-3 10 ml falcon tubes depending on amount of water going through the filter. The filters were wrapped in aluminum foil and placed in sample bags. On San Salvador all filtering was performed at the field sites. All samples were kept in a cooling bag during the fieldwork. At arrival on the field station at the end of each field work day; the sediment samples and sampled filters were put in the freezer and all filtered water samples were put in the fridge. On Eleuthera water was brought back in containers to the field work apartment before filtering and the filters were immediately put in the freezer and the water samples in the fridge until department. All filtered water, sediment and organic samples were brought back to Stockholm University and stored in fridge and freezer respectively until analyses were performed.

3.2.3 Porewater sampling

The length of the core B2 from Big Pond for porewater sampling was 52 cm. The top plug was kept on the tube from sampling until all porewater sampling was finished to avoid any change in water chemistry due to oxidation or CO_2 exchange. The porewater sampling was performed at the apartment used as field work base on Eleuthera. A rhizon was inserted in every second of the pre-drilled holes; connected with a 3-way stopcock to 10 ml syringe; for each 2nd cm (1-51 cm) and at 5 cm above the core top in the water (Fig.7). Vacuum was created in the syringes by pulling the plungers back while the stopcocks were closed. Sticks was used to fix the plunges in position. The stopcocks were turned when all syringes

were fixed to make the withdrawal of pore water at all levels simultaneous. Before removal of the syringes, the stopcocks were closed for and the samples were transferred to 5 ml polystyrene round-bottom Falcon tubes. The amount received for each level varied from 1,5 ml to 10 ml (15 ml was withdrawn from the top water).

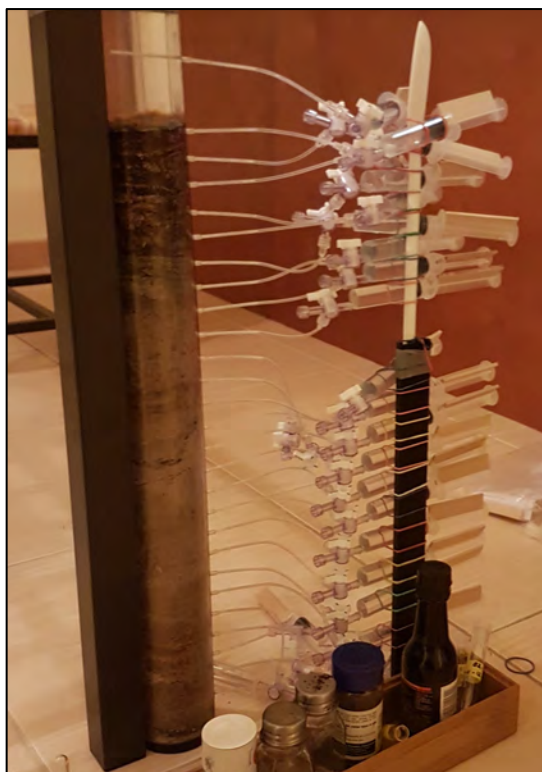
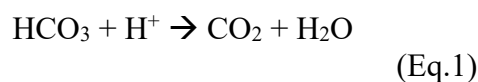


Figure 7: Porewater sampling setup at the fieldwork apartment on Eleuthera.

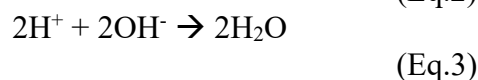
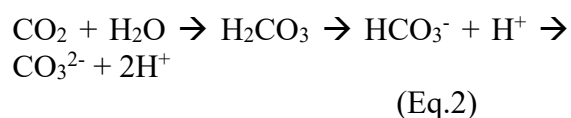
3.2.4 Porewater DIC analysis

Porewater dissolved inorganic carbon (DIC) was quantified by flow injection analysis (FIA) at Stockholm University. The method makes use of the carbonate equilibrium system and produces conductivity difference measurements. A set of standards is run before the samples and the received values are used to make a calibration curve to calculate the DIC content in mM. Each sample is injected into a 50 μ l closed loop. The loop is manually opened by a switch and the sample is loaded into a tubing system where it gets mixed with a 20 mM HCl solution which is used

as a carrier liquid. When the sample is mixed with the acid, all DIC in the sample transforms into CO₂, see equation 1.



The acid flow carries the sample at chosen rate in through the first of the two columnar chambers in a gas exchange cell. The two chambers are separated by a 0,075 mm Teflon membrane. The membrane is porous enough for gas diffusion but do not let liquid through. In the other chamber there is a flow of 5 mM NaOH solution which is used as a receiver liquid. The CO₂ that enters the base will transform into CO₃, which results in a removal of OH⁻, see equation 2 and 3.



The conductivity of the basic solution is continuously monitored by a JENCO conductivity controller 3101 that is installed in the tubing system after the column passage. The conductivity controller is connected to a 6230N pH/mV/TEMP meter and the conductivity values are registered. When OH⁻ decreases there will be a decrease in conductivity (Wolkersdorfer, 2008). The difference between the receiver liquid baseline and the minimum value measures when the sample passes through is used to calculate the DIC content from the standard curves.

Standards of 100, 10, 5, 2.5 and 1 mM NaHCO₃ were prepared to use for calibration curves. A new standard run was conducted after every 7 samples. A flow of 2,1 ml/min was created with a LABINETTE tube pump.

3.2.5 Core splitting and subsampling

Core NP18 was split in half into NP18A and NP18B in a core splitter at the Department of Geological Science at Stockholm University. NP18A was used for subsampling and NP18B was used for ITRAX analyses. Subsampling was made for lipid analysis and for SEM analysis. The subsamples intended for lipid analyses was retrieved with a spatula into 30 samples where the sample depth and thickness were determined by the stratification along the length of the core. The subsamples were named 01-30 from top to bottom of the core length, see table 1 and figure 21 in section 4.1.3. for details. The samples were placed in glass vials with snap-caps and stored in the fridge. For SEM analysis 12 subsamples were selected at specific parts of the core to include as many carbonate laminae as possible. The samples were cut out with scalpel into approximately 5 x 10 x 2 mm pieces and put with the top end of the sample towards the numbered end of pre-numbered aluminum trays. The SEM subsamples were immediately further prepared by chemical drying in a series of alcohol baths, 50%, 70%, 80%, 90%, 95% and 100% to replace the water in the samples step by step to keep as much of the original morphology of the sample as possible. The final bath before imaging was done in TMS (tetramethylsilane), followed by full evaporation.

3.2.6 X-ray fluorescence (XRF)

The cores C7A (2015) and NP18B (2018) was analyzed in an ITRAX XRF Core Scanner from Cox Analytical systems (Gothenburg, Sweden) by Malin Kylander at the Department of Geological Science, Stockholm University. A Mo X-ray tube was used. The XRF settings were 30 kV and 50 mA, exposure time 110 seconds. The radiography settings were 55kV and 50 mA, exposure time 600 ms. Step size (resolution) was 200 microns. Same settings were used for both cores.

3.2.7 Scanning Electron Microscopy

The 12 selected subsamples from the New Pond sediment core (NP18A) and two chosen thin sections from the top (BP151b) and bottom (BP1513b) of core C7A was analyzed in a Scanning Electron Microscope Quanta FEG 650 equipped with an Oxford instruments X-max backscatter electron (BSE) CBS detector at the Department of Geological Sciences, Stockholm University. The software used was AZTEC. The thin sections were masked off and gold coated along the length in the middle. The subsamples from NP18A were mounted on stubs with silver paint and gold coated. The samples were imaged in high vacuum, with a range of accelerating voltage from 5 to 30.00 kV and chemically analyzed using an X-Max Large Area EDS Silicon Drift Detector from Oxford equipped with the AZtecOne EDS software.

3.2.8 Lipid extraction

Lipid extraction was performed on the microbial mat sample from Big Pond, divided into three subsamples (BP1801-03), GFF filters from the filtered surface water from two parts of Big Pond (GFF1a and 1b) and from New Pond (GFF3), and lastly 12 of the subsamples from NP18A with high content of organic material. All samples were freeze-dried for 72 hours in a SCANVAC Coolsafe 55-4 Pro freeze-dryer at Stockholm University.

The freeze-dried samples were ground to a fine powder, and the filters were cut in small pieces before they were weighed on a R322a Sartorius Quintix 224-1s balance with 0.0001g resolution. All samples were split in two equal halves with the prefix A and B added to the sample numbers.

To obtain the CL-GDGT fraction, The A samples were extracted with a mixture of methanol/dichloromethane (MeOH/DCM), while bulk GDGTs, i.e. also those released from IPL's, were obtained from the B samples by acid hydrolysis followed by

MeOH/DCM-extraction, using a method modified from Ingalls et al. (2012).

The A samples were extracted in five steps:

- 1) 10 ml MeOH,
- 2) 5 ml MeOH + 5 ml DCM
- 3) 5 ml MeOH + 5 ml DCM
- 4) 8 ml DCM + 2 ml MeOH
- 5) 8 ml DCM + 2 ml MeOH

After each addition of solvent, the samples were put in an ultrasonic bath for 10 minutes and centrifuged for 5 minutes in an Eppendorf Centrifuge 5810R at 800 rcf (relative centrifugal force). The extract from each run was separated from the sediment, transferred and combined into a total lipid extract (TLE) and put under N₂ flow at 25°C for evaporation.

The B samples were hydrolyzed and extracted in four steps: The first step included acid hydrolysis to separate the polar head groups from the core lipids of the intact polar lipids, using the following scheme:

- 1) 10 ml of 5% HCl in MeOH. The samples were heated at 50°C for ca 20 hours in this solvent.
- 2) 3,5 ml MeOH + 3,5 ml DCM
- 3) 3,5 ml MeOH + 3,5 ml DCM
- 4) 7 ml DCM + 1 ml MeOH

After heating and after each subsequent solvent addition, the samples were put in an ultrasonic bath for 5 minutes and centrifuged for 5 minutes. The supernatants from the subsequent extractions were combined into a total lipid extract. The vial was topped by back-extracted water and centrifuged for 5 minutes, allowing an aqueous/apolar phase separation. The apolar phase was transferred into a new set of 40 ml glass vials. The vials were put under N₂-flow at 25°C for evaporation.

All TLE samples were purified by solid phase chromatography. Glass SPE columns were prepared with DCM-rinsed cotton in the bottom and filled approximately halfway with deactivated silica gel (95%).

Less than 1 ml DCM were added to dissolve the dry extract before adding 20 µl diol standard (4,92ng/µl) to each sample, this was adsorbed on silica gel, and subsequently dried under a very gentle flow of N₂ at 25°C. The adsorbed TLE was added on top of the pure silica gel in the glass columns. Two fractions were eluted from each sample into 12 ml bottles: fraction one (F1) was eluted with hexane to retrieve hydrocarbons and a second fraction (called F3 for technical purposes) with DCM/MeOH (1:1) to retrieve lipids. All F1 and F3 fractions were dried under N₂ at 25°C.

All tools used for handling the silica and samples were pre-rinsed with DCM. The A samples got the final prefix -CL (core lipids) and the B samples got the final prefix -AH (acid hydrolysis). The F3 samples were prepared for high performance liquid chromatography-atmospheric pressure chemical ionization-mass spectrometry (HPLC-APCI-MS). 500 µl hexane/isopropanol (99:1) was added to each F3 sample. The samples were sonicated for 10 minutes and transferred to Mini-UniPrep G2 Clear glass chambers which were sealed with a proprietary syringeless Mini-UniPrep filter device (0.45 µm pore size).

The F1 samples were prepared for gas chromatography mass spectroscopy (GC-MS) by transferring into GCMS autosampler vials, and reconstitution into 500 µl hexane.

3.2.9 HPLC-APCI-MS

GDGTs were analyzed by HPLC-APCI-MS (high performance liquid chromatography-atmospheric pressure chemical ionization-mass spectrometry) at the Department of Geological Sciences, using an HPLC Ultimate 3000 RS HPLC pump with autosampler, heated column compartment, an APCI interface operated in positive mode, linked to a Thermo TSQ Quantum Access MAX triple quadrupole mass spectrometer.

The solvent gradient used was: 0-15min isocratic at 18% B (i.e. 82%A), followed by a gradient to 35%B at 35 min, to 100% B at 55 min, followed by 15 min of reconditioning. Solvent A was hexane, solvent B hexane/isopropanol (9:1 v/v). The system was run by a combination of Chromeleon and Xcalibur software. Quantification of peak areas of interest was done using Xcalibur software, using the internal diol standard for quantitation. Response factors for different GDGTs compared to the diol standard were not known, and not applied.

3.2.10 Analyses of anions and cations

Porewater from core C3, B2 and surface water from New Pond, Big Pond main and south basin was analyzed for anions and cations at the Department of Geoscience, Stockholm University. The porewater from core C3 was diluted x 10000 for cations and x 1000 for anions, the porewater from core B2 and Big Pond surface water was diluted x 1000 and the New Pond surface water was diluted x500. Dilution was done based on salinity and which levels that are suitable for the analyze equipment. Anions were analyzed by ion chromatography performed by Pär Hjelmquist on an IC20 from Dionex. The IC20 was equipped with an IonPac AS22, 4x250 mm column and an AERS 500, 4 mm suppressor. The injection volume was 10 μ l. The eluent was 4,5 mM Na₂CO₃/1,4 mM NaHCO₃, and the flow rate was 1,2 ml/minute.

Cations were analyzed by inductively coupled plasma mass spectrometry (ICP) by Carl-Magnus Mörth.

3.2.11 Radiocarbon dating

Leaf fragments were collected from three different depths in core C7A, treated with HCl to remove carbonate and dried. The fragments were submitted for radiocarbon age analyses ($\Delta^{14}\text{C}$) to Lund University Radiocarbon Dating Laboratory, Sweden. The samples were pre-treated by the

laboratory with 0.5% NaOH (20° C) followed by 1% HCl (80° C), except for sample LuS-12173 that was only treated with 0.5% HCl because of the fragile character of the material. After drying, approximately 3 mg of each sample was weighed in and converted to graphite using an automated graphitization equipment (AGE-3) coupled to an elemental analyser (Wacker et al. 2010). The graphite was then pressed into targets, and carbon isotope ratios were measured by accelerator mass spectrometry using the SSAMS machine at the Department of Geology, Lund University, Sweden (Skog et al. 2010). Ages were calibrated using IntCal13.

4. Results

4.1 Sediment core descriptions

Sediment cores were retrieved from two lakes; Big Pond and New Pond. Sediment profiles from both lakes display altering horizontal layers of organic material, in situ precipitated calcium carbonate (CaCO_3) and oolitic sand. There is at least one thick carbonate sand layer that represents one single weather event, evident by a microbial mat piece that is buried perpendicular to the bedding in a New Pond core profile (Fig.9D).

In Big Pond the bottom surface (i.e top of microbial mats) is unconsolidated and cannot carry an adult person's weight, while in New Pond the surface is sturdy enough to walk on.

Cores retrieved in different parts of the basin can have different depths and varying in thickness and appearance of laminated and non-laminated layers. Figure 8 display whole cores to give examples of the heterogeneity of the lake sediment bedding. 8A and B show two cores from New Pond; NP18 is the core brought back to Stockholm University for analyses. Both cores were retrieved in the same area of the lake (Fig. 6B, site 3). The two cores show similar length but different appearance of layers. Figure 8C-F show cores retrieved in Big

Pond (Fig. 6A). Core B1 and B2 were retrieved in the same area of the main basin but show different depths. Core B2 was used for extraction of porewater that was brought back to Stockholm University for analysis. Core C was retrieved at another area of the main basin and core D in the south part of the basin. All cores from the two lakes except for core D show a similar pattern with 10-15 cm of organic lamination at the top and at least one layer with no lamination at all below. Several cores show organic lamination toward the bottom part of the core too. Core D differ from the other cores by being mainly composed of gravel sized clusters of gypsum crystals and the top part is rich in organic material and displays some lamination; though not as distinct as in the other cores. Figure 9 shows split cores to further display the similarities and differences between cores. 11A-C show cores from Big Pond 2015 and 11D shows the core NP18 from New Pond 2018 (sample locations Fig. 6). Red boxes mark out non-laminated beddings. These beddings represent single storm-events, as evident from a buried microbial mat slab crosscutting the beds (Fig. 11D). Features that crosscut the bedding are outlined with red dots (Fig. 11 C and D). Core C7 was used for ITRAX scanning and will be further described in detail.

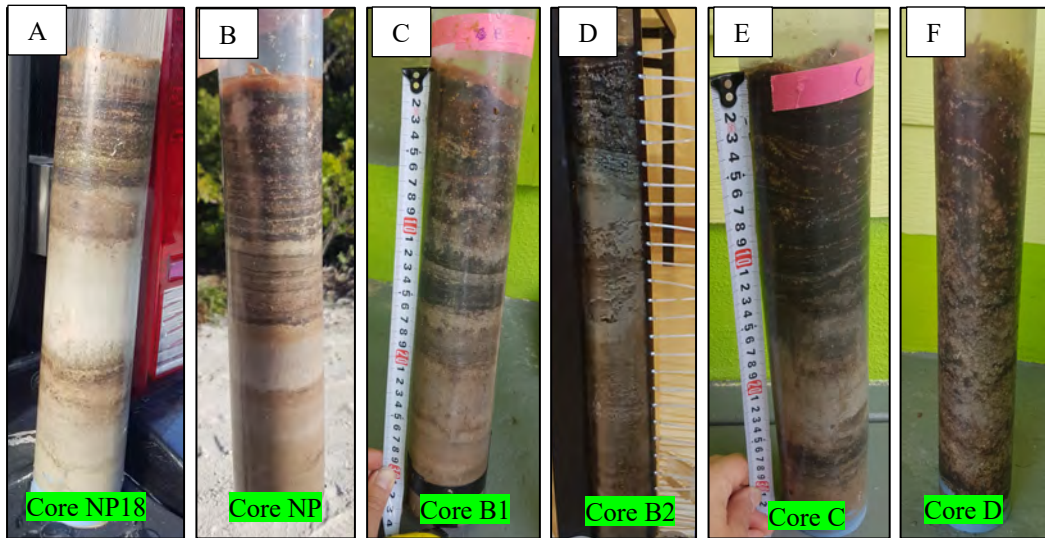


Figure 8: Whole cores. A and B show cores from New Pond and C-F cores from Big Pond, all retrieved from Big Pond 2018. Core NP18 was brought back to Stockholm University and core B2 was used for porewater analysis.

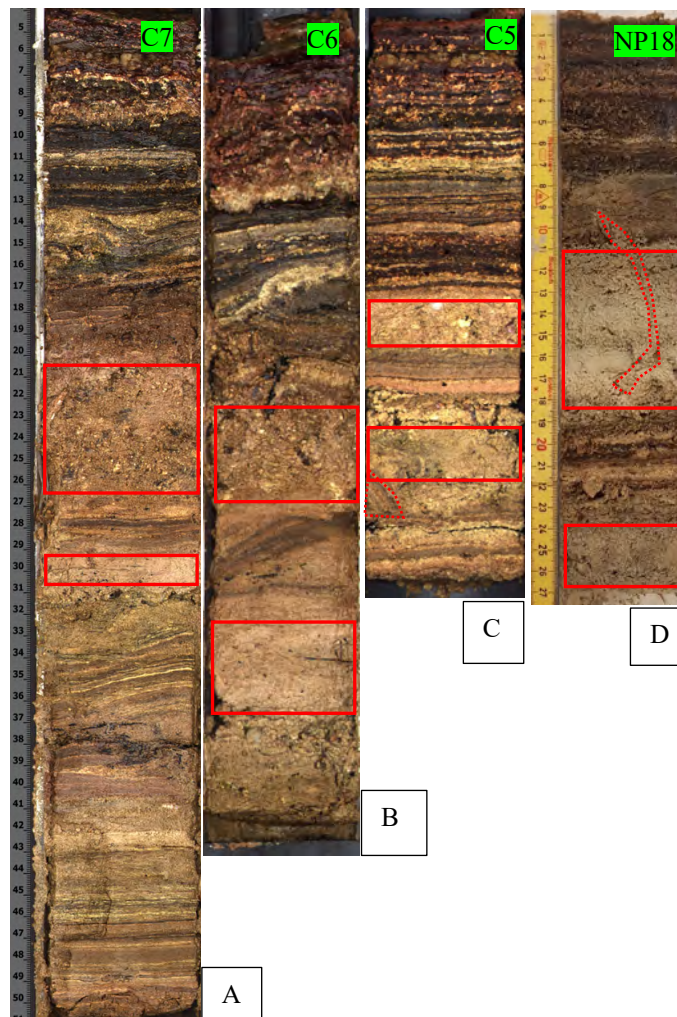


Figure 9: Split cores. A) Core C7 from Big Pond (2015), B) Core C6 from Big Pond (2015), C) Core C5 from Big Pond (2015), D) Core NP18 from New Pond (2018). Non-laminated layers are marked with red frames. Features that are crosscutting bedding planes are marked with red dashed lines. (Observe that the left measuring tape do not begin at zero.)

4.1.1 Core description C7A, Big Pond

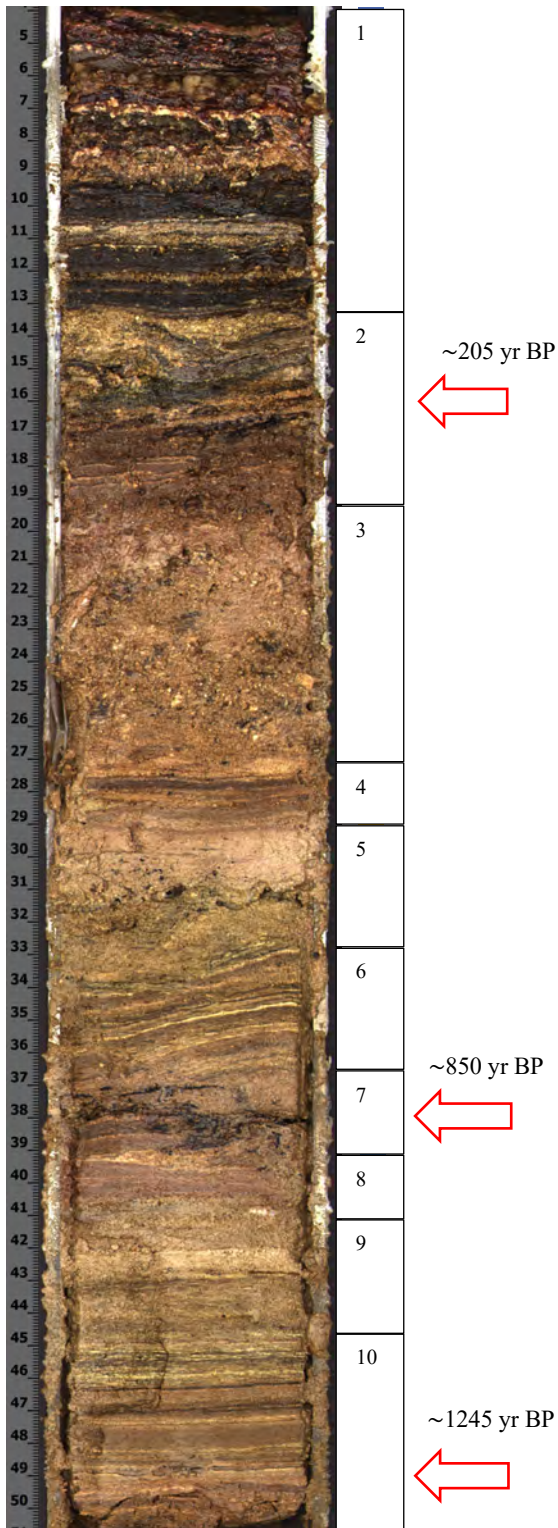


Figure 10: Core C7A with sections and ages marked out. Note that the measuring tape do not begin at zero.

Core C7 (2015) is the core from Big Pond that have the greatest depth of the retrieved cores and display rich lamination. The core half C7A was chosen for ITRAX scanning and in addition 13 thin sections were made along the length of the core. Radiocarbon dating was done for leaf parts found at three depths. The physical appearance of this core is described in this chapter. The description is divided into sections (Fig.10). Approximate distribution of organic matter, carbonate and gypsum in percentages in the top and bottom is based on visual appearance only since loss of ignition was not done.

Radiocarbon dates and calibrated ages from the Big Pond sediment core are listed in table 1. The data indicate an average sediment accumulation rate of 0.36 mm /yr, including mass deposits or erosion during storm events. For an accurate age model taking into account such deposits, much higher resolution dating is needed.

Table 1: AMS Radiocarbon dates of three macrofossil leaves from Big Pond, and their calibrated ages in yr BP and common era (CE) notations.

Depth (cm)	¹⁴ C age (yr BP)	±	1σ range (cal yr BP)	Cal age CE
11-13	205	35	85-287	1764 ± 101
32-34	850	40	727-829	1172 ± 51
44-46	1245	35	1127-1245	764 ± 59

Section 1: From 0 to 9 cm depth, the sediment core displays a well-defined horizontal lamination. Organic matter (OM, dark areas) constitute the dominant facies, approximately 60 %, with laminae up to 1 cm thick in which few, very thin carbonate laminae or small patches are present. Carbonate laminae (light colored areas) constitute approximately 30% of this section. Carbonate laminae between 0,5 and 1,5 cm are very thin and made up of non-coherent patches with a horizontal

alignment. At 3 cm depth carbonate make up a few mm thick semi-coherent crust. At 4-5 cm, 7 cm and 8 cm depth there are carbonate dominated but patchy/porous laminae with a few mm up to one cm thickness. The remaining 10 % constitute gypsum supported laminae up to 3 mm thick at 0,5 cm, 2 cm and 3,5 cm depth. The gypsum crystals that are in the size range of 0,5 to 1,5 mm, have a random orientation and sometimes grow rosette morphologies.

Section 2: The section between 9 and 15 cm first displays a few mm thick semi-coherent porous carbonate crust at the top. Then, one can see a downward alteration between thin non-coherent undulating carbonate patches and organic matter laminae. At the bottom, very thin carbonate laminae in a brown matrix are observed. The brown matrix is porous and is likely to be OM-rich and carbonate poor, there are only dispersed dark residues in these areas in the thin section.

Section 3: The interval between 15 and 23 cm depth does not show lamination. The top cm is brown (likely OM-rich), contain a few seemingly intact slater-like bugs and look burrowed. The remaining part of the section display a beige-brown color and contain randomly distributed patches of OM, shell clasts and grains.

Section 4: Interval between 23 and 25 cm displays a distinct lamination with altering brown and beige laminae, each a few mm thick. One of the brown laminae is darker (relatively more OM-rich).

Section 5: The section between 25 and 29 cm constitutes porous carbonate with a lot of carbonate bivalve shell parts. The top part displays a beige color and the bottom part is beige-green (relatively rich in OM). There is a vague tendency of non-coherent OM lamination and patches which is most concentrated in the middle where there is a layer containing large gastropod shells.

Section 6: Between 29 and 33 cm depth, there is a distinct undulating lamination with altering thin (~1 mm) light coloured carbonate laminae, beige-brown to green-brown (the darker, the higher relative OM-content), up to a few mm thick carbonate laminae and dark thin (~ 1 mm) OM laminae.

Section 7: 33-35 cm an irregularly distributed OM interrupting thin, light colored carbonate laminae in an otherwise brown-beige matrix.

Section 8: 35-37 cm similar to section 4 but without any distinctly darker laminae and with relatively thinner beige laminae.

Section 9: 37-41 cm similar to section 5 but with the beige/lighter colored carbonate as a 0,5 band in the middle.

Section 10: 41-46 cm similar to section 6 without undulation. The approximate distribution of carbonate/OM is 90/10 % based on visual appearance.

4.1.2 Detailed description of top and bottom part of core C7A

Thin sections were made along the length of core half C7A. This section focuses on the top and bottom thin sections and their physical appearance in photomicrographs and backscatter electron images. Elemental maps of chosen areas are included to give an idea about the elemental distribution. The thin sections were gold coated before SEM analysis, this is the reason why Au appears in the map sum spectra. Elemental spectra from SEM analyses of chosen features are marked in the figures and are summarized in table 2 where the values are normalized without Au.

The top ~3,5 cm is characterized by a high content of organic matter (OM). The OM is distributed in horizontal undulating laminae varying in thickness, seen as darker areas in figure 11a. In the thin section making

process the pure OM laminae were chemically dried and embedded in epoxy. The unavoidable shrinkage of the organic matter related to this process show high porosity visible in fig. 11b. The darkest patches in the photomicrographs (seen in the upper part in fig. 11e), contain mineral grains with Fe and Si content, (Fig. 13 and 14).

A gypsum filter is used for the photomicrographs to enhance the difference between carbonate and empty space/epoxy, which is otherwise both white when seen in microscope without gypsum filter. The epoxy areas and the lighter shade of pink in fig. 11c-e.

Between 0,5 and 1,5 cm depth there are semi-horizontally aligned unconsolidated patches of carbonate embedded within organic material. At 3 cm there is a 2-5 mm thick semi-coherent carbonate horizon with relatively low porosity. Pure carbonate shows a light color, while OM-containing carbonate show a pale green (low OM) to dark brown (high OM) hue in the photomicrographs. Some carbonate grains/patches have a netlike pattern (see upper part of figure 11f). SEM reveal this pattern as cracks and holes in the carbonate (Fig. 11g, h). Coherent carbonate patches are amorphous (Fig. 15-17), grading to rod-shaped in less dense area (fig 18).

At 0,5 cm, 2 cm and 3,5 cm there are ~ 3 mm thick gypsum supported laminae. These are seen as pale yellow-green in fig. 11a, elongated dark grey oblique crystals with a random orientation in fig. 11b and a darker shade of pink on fig. 11 c-e. The gypsum crystals have a size range of 0,5-1,5 mm. These are the only gypsum laminae in the whole core. SEM mapping reveals that there are only gypsum residues in part of the gypsum shaped casts, shown by the conformity of the S and Ca maps. The Si map reveal wholes where it is the thin section plate that is analyzed, and the C map represents epoxy and might contain organic matter residues (Fig. 12).

The bottom ~3,5 cm is characterized by a high content of porous carbonate; mainly composed of ~ 5 µm calcite rods with rounded edges. The carbonate rods are distributed in higher density in horizontal undulating laminae with varying thickness, seen as lighter areas between 1,5 and 3,3 cm depth in figure 19a, and lower density in the unlaminated areas. In the thin section making process frequently occurring uneven shaped particles were dissolved, leaving empty holes. The holes are black in fig. 19a and a dark shade of pink in 19 b and d.

Table 2: Normalized elemental composition in wt% summarized from SEM elemental spectrum analyses in core C7A.

Fig.	Feature	Spectr.	Ca (wt%)	O (wt%)	Mg (wt%)	S (wt%)	Na (wt%)	Fe (wt%)	Si (wt%)	Total (wt%)
16	patch	6	47,45	36,73	14,29	1,02	0,51			100
17	rod cluster	7	53,55	33,55	11,61	1,29				100
14	iron oxide	1	1,37	28,77				63,01	6,85	100
14	quartz	2		53,33					46,67	100
14	other	3	20,65	41,30				14,13	23,91	100

Figure 11,below: Top part of the core, scale to the left in cm valid for a)-c), scale to the right 1mm valid for d) and e). a) Photograph of the core, b) Thin section BP15C71b scan image with crossed polar filter, with insets showing the positions of c) (dashed line), d) (upper rectangle) and e) (lower rectangle). c) Transect of the thin section made of combined photomicrographs. d) Photomicrographs for enlarged details, black rectangle marks the position of figure f). e) Photomicrograph for enlarged details, insets showing the positions of figure 13 (lower rectangle) and 14 (upper rectangle). F) Photomicrograph for enlarged detail. g) Backscatter electron image from SEM showing approximately the same area as g), red rectangle marks the position of h). h) Enlarged detail from g), backscatter electron image showing close up of cracked carbonate.

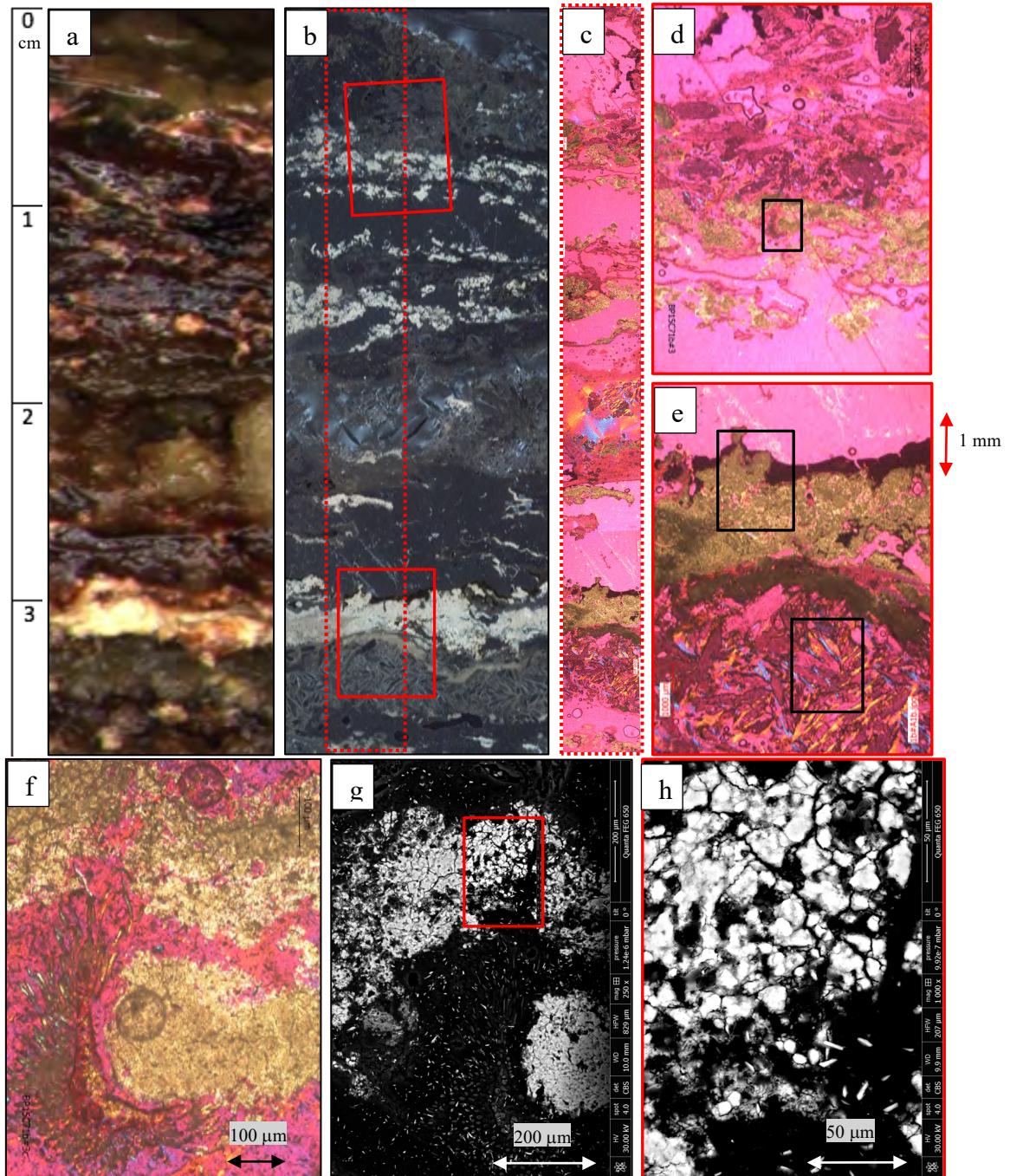
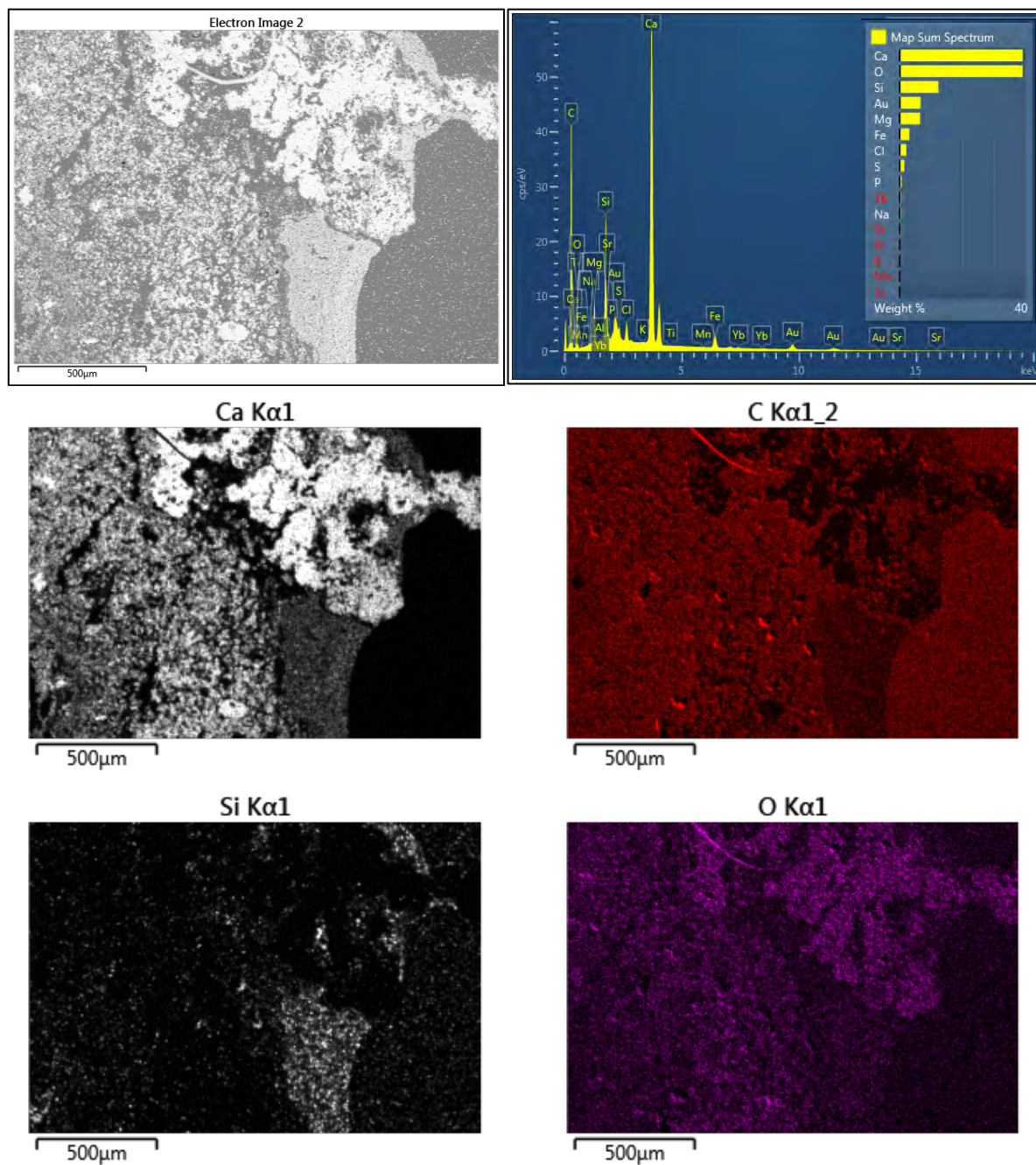


Figure 13, below: Backscatter electron image of upper area marked out in figure 11 e, located at approximately 3 cm depth in the core. Map sum spectrum and maps for C, Si, Ca, O, Mg, Fe, Ti and Al included.



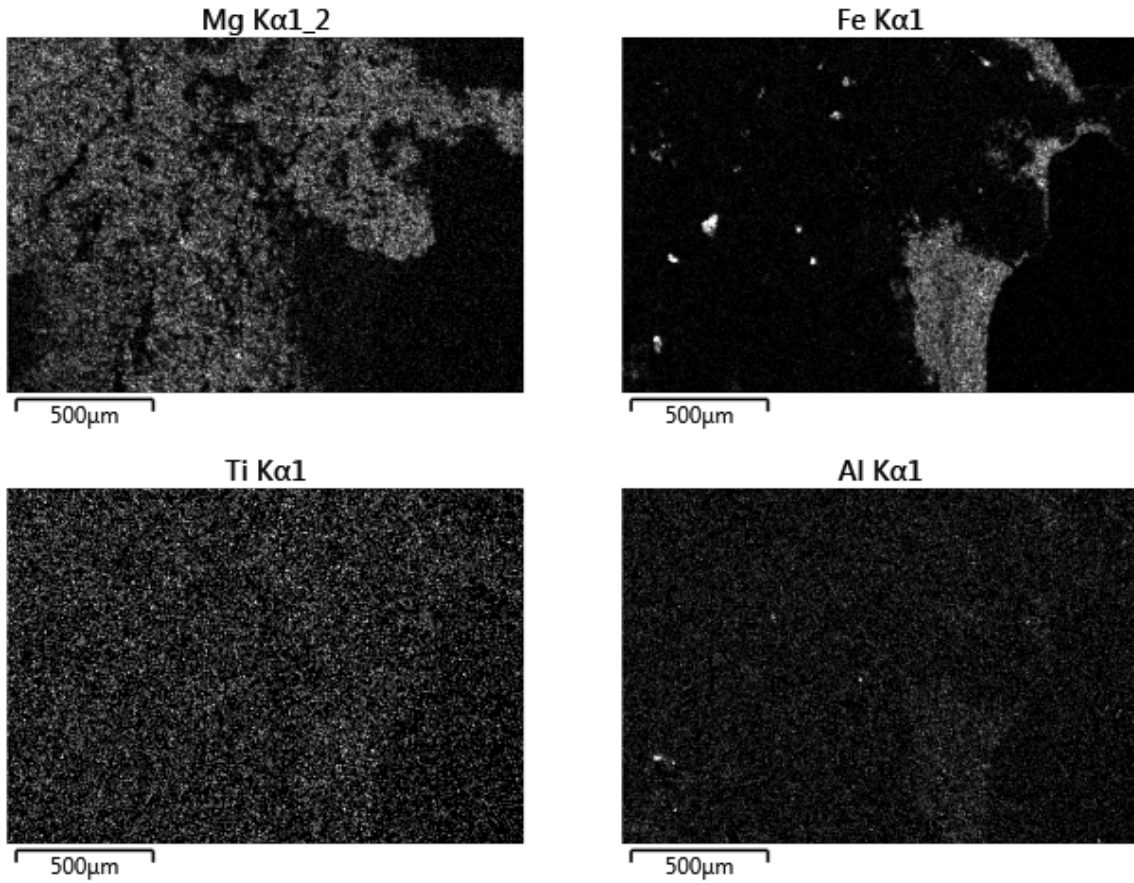
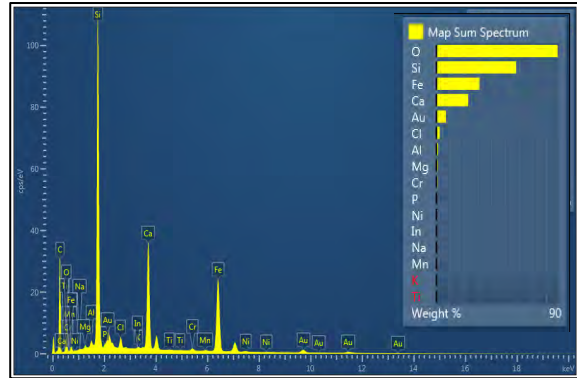
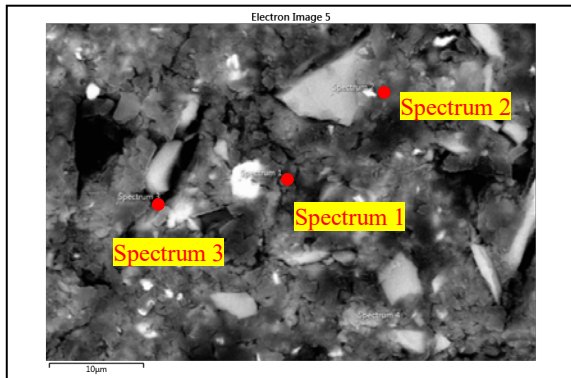


Figure 14, below: Backscatter electron image of close-up of Fe+Si-rich area in figure 13 with spectrum 1-4 marked out. Spectrum compositions is summarized in table 1. Map sum spectrum and map of Si, Ca, Fe, C, O, Al, Mg, Mn, Ti, Ni, Na, and Cr included.



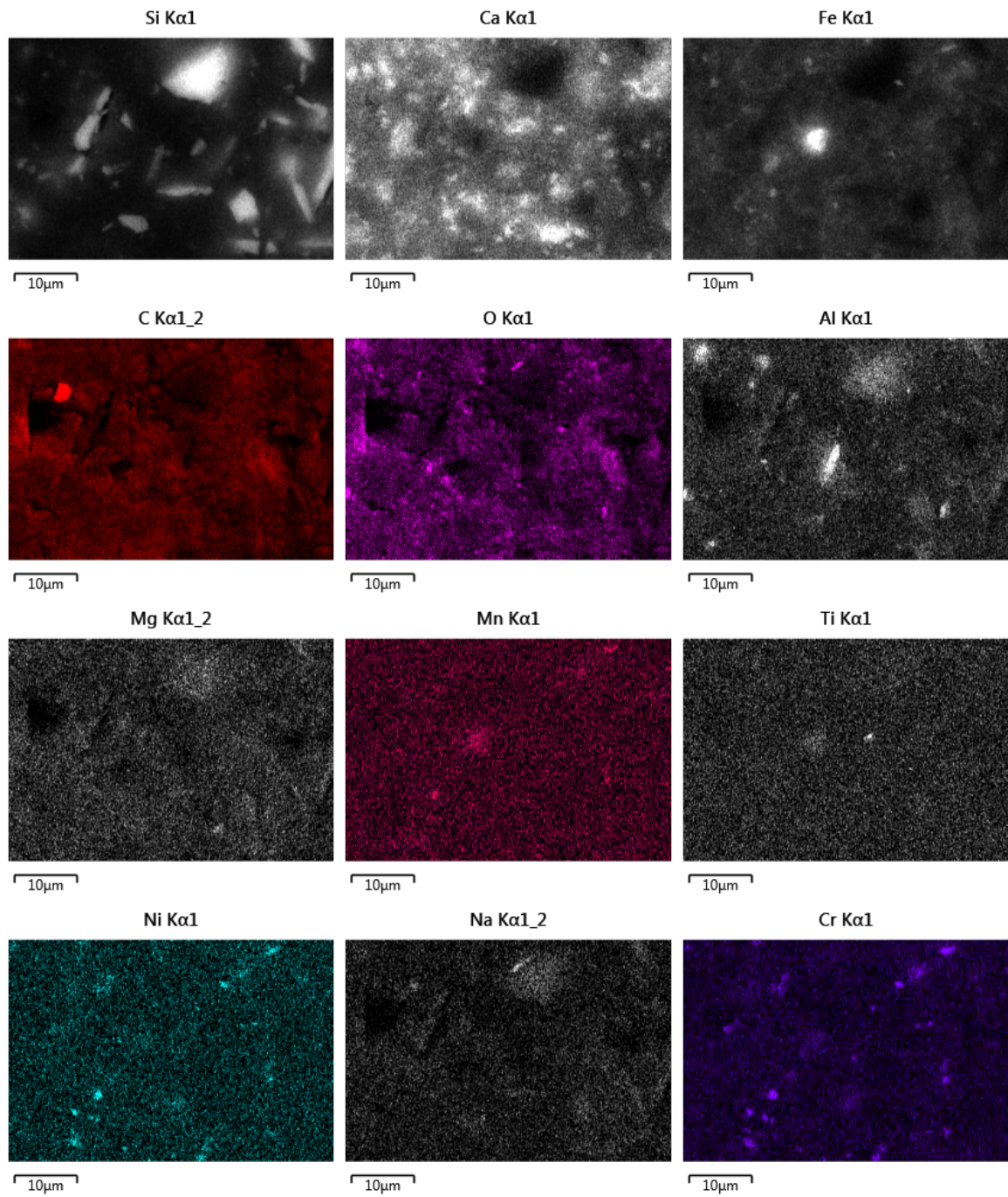


Figure 15, below: Backscatter electron image of close-up of Ca-rich area in figure 13 with map sum spectrum marked out. Spectrum composition is summarized in table 1. Map of Ca, C, Si, Mg, O, S, Fe, Ti, and Al included. Red rectangle marks out the position of figure 16.

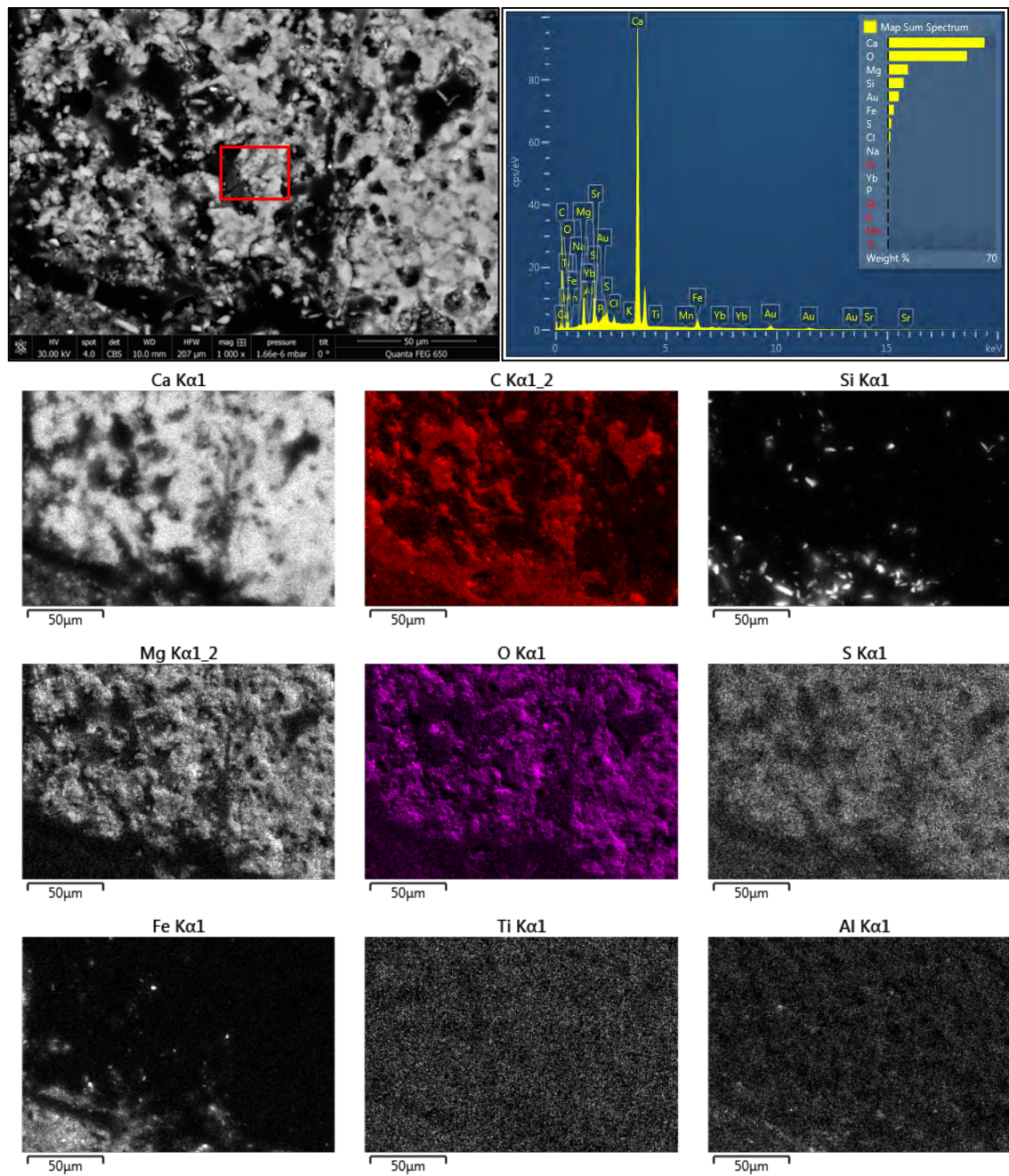


Figure 16, below: A) Backscatter electron image of denser carbonate area in figure 15 with spectrum 6 marked out. Spectrum composition is summarized in table 2. Red rectangle marking out close-up of carbonate in B) that reveal no crystalline structure

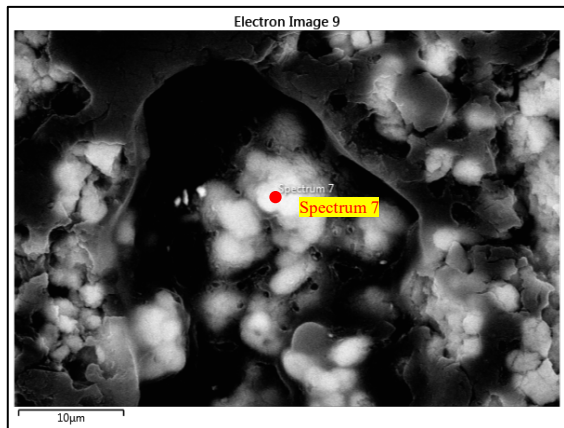
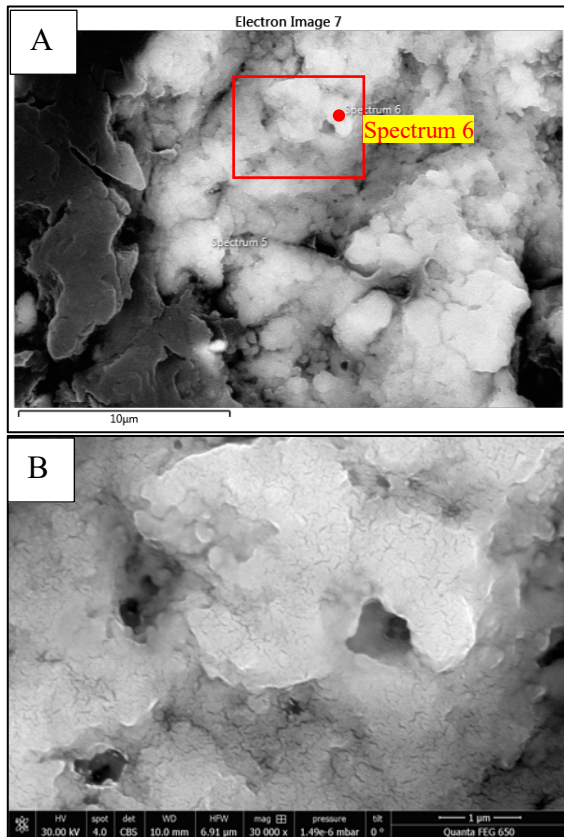


Figure 17: Close-up of an area with less density of calcium carbonate in figure 13, spectrum 7 marked out. Spectrum composition is summarized in table 2.

Figure 18: Bottom part of the core, scale to the left in cm valid for a) and b). a) Thin section BP15C71b scan image with crossed polar filter, with insets showing the positions of of b) (dashed line) and c) (solid line). b) Transect of the thin section made of combined photomicrographs. c) Photomicrograph for enlarged details, rectangle mark out the position of d). d) Backscatter electron image, rectangle mark position of figure 20.

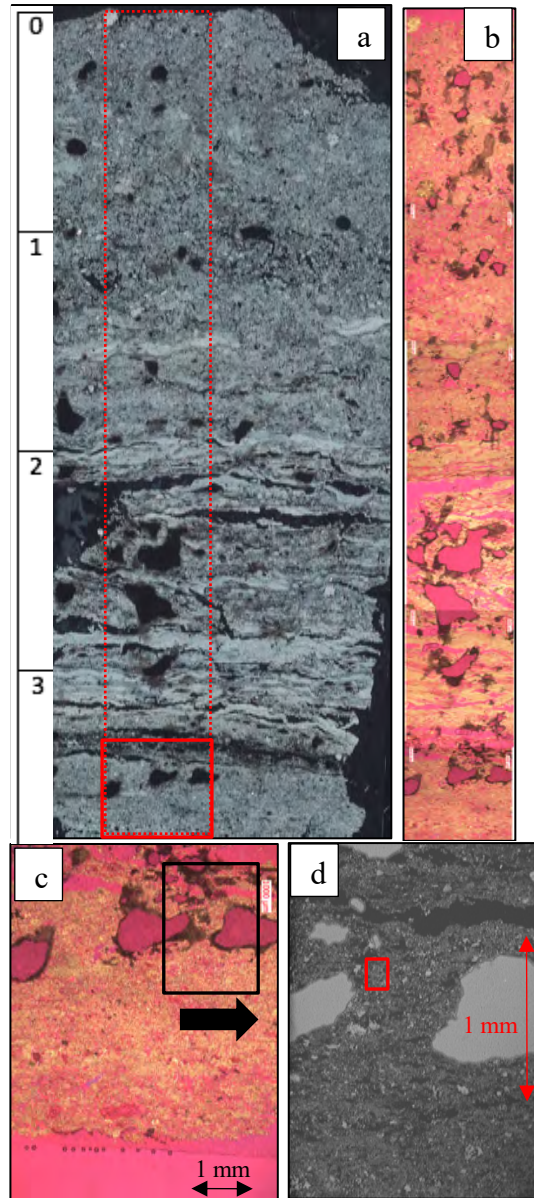
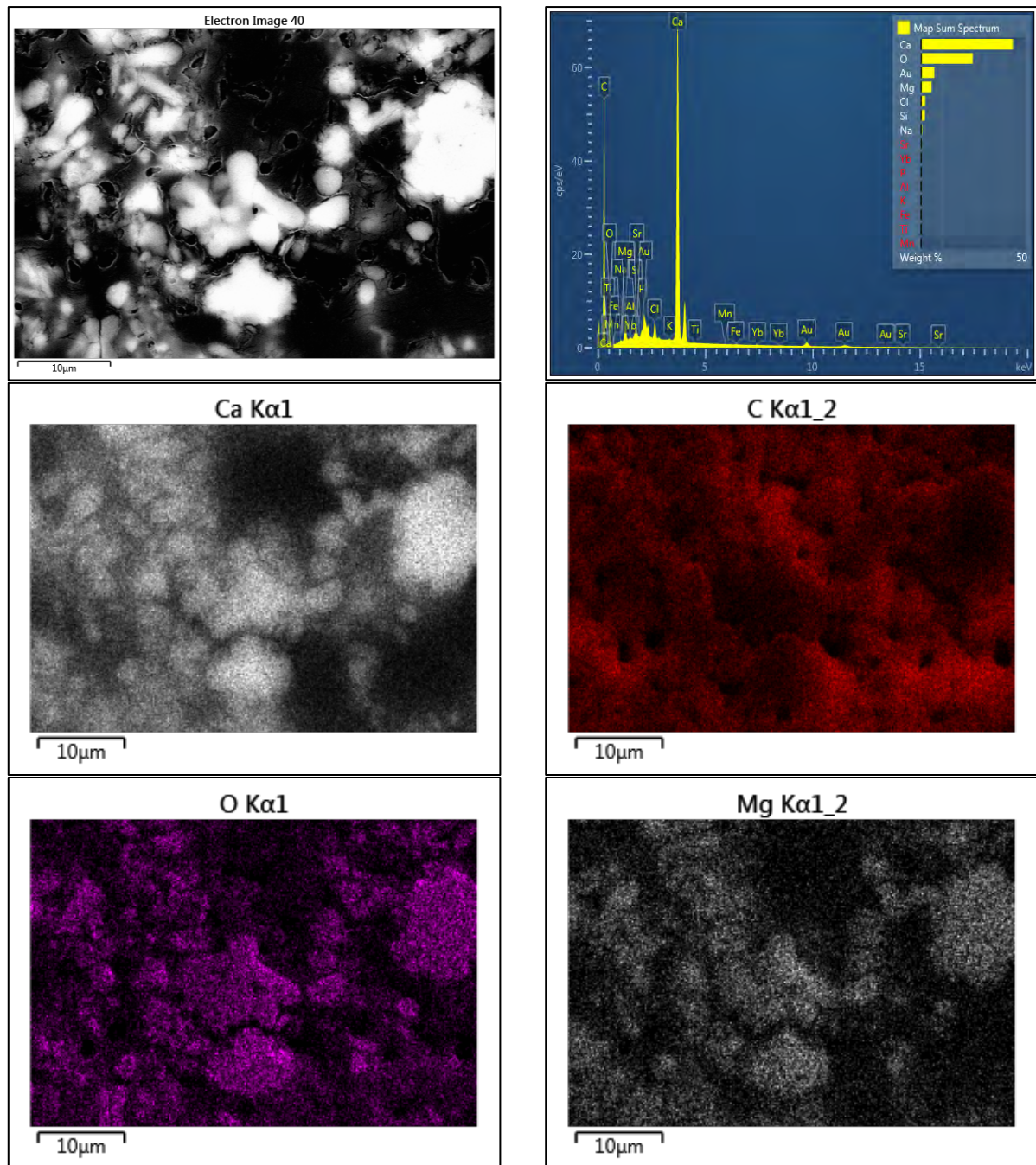


Figure 19, below: Backscatter electron image with map sum spectrum and maps of Ca, C, O and Mg included.



4.1.3 Core description NP18, New Pond 2018

Core NP18 was retrieved from New Pond 2018. The core half NP18A was chosen for subsampling and NP18B was chosen for ITRAX scanning. The subsamples are described in Table 3. Subsamples chosen for lipid extraction are marked with red circles in figure 21; where number S1-S12 are subsamples that were chosen for SEM analysis.

The physical appearance of NP18A is described in this chapter and the description is divided into sections (Fig.21). Approximate distribution of organic matter, carbonate and gypsum in percentages in the top and bottom is based on visual appearance only since loss of ignition was not done.

Section 1: From 0 to 7,5 cm depth, the sediment core displays a horizontal lamination. Organic matter (OM, dark areas) constitute the dominant facies, approximately 60 %. The OM laminae (dark green) is from 4 mm thick at the top to <1 mm at the bottom; separated by porous carbonate laminae with varying

thickness between <1 mm to 4 mm. The color of the OM varies from green at the top, through red to very dark. A gastropod shell was found at 4 cm. There are no visible gypsum laminae, though in scanning electron microscope (SEM) 5-25 μm gypsum crystals are frequently occurring.

Section 2: The section between 7,5 to 10,5 cm contains carbonate sand with gastropod shell parts and a few thin mat fragments in, with a brown mat at the bottom.

Section 3: The section between 11 and 19 cm contains carbonate sand with a large intraclast of mat flipped vertically, intruding up in section 2. The bottom 2 cm contain OM fragments.

Section 4: The section between 19 and 23 mm contains dark mat laminae, most very thin but two in the middle are a few mm thick. The mat laminae are either separated by very thin carbonate laminae or thicker (2-10 mm) carbonate sand laminae.

Section 5: The section between 22,5 to 27 cm contain carbonate sand with shell fragments.

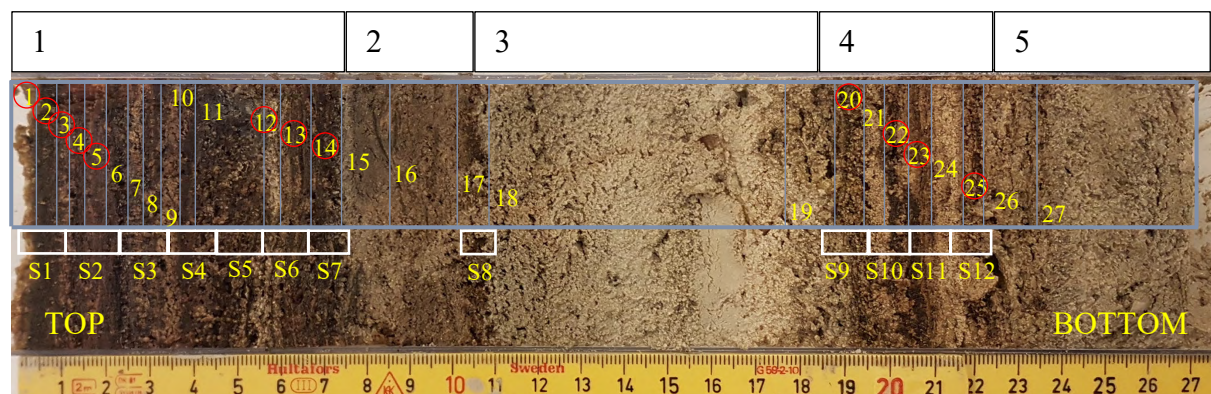


Figure 20: Core NP18A section 1-5 and subsamples. Subsamples 1-27 described in table 1 are marked with orange boxes. Red circles marks which subsamples were chosen for lipid analysis. S1-S12 marked with white boxes are the subsamples made for SEM analysis.

Table 3: Description of subsamples of core NP18A with depth intervals and lipid extraction sample numbers.

Sample	Depth (mm)	Description	Lipid extr.
NP18A01	0-4 mm	upper crust, soft mat + carbonate grains	1
NP18A02	4-8 mm	green jelly mat	2
NP18A03	8-11 mm	red jelly mat + carbonate grains	3
NP18A04	11-16 mm	red jelly mat + carbonate laminae	4
NP18A05	16-20 mm	red jelly mat + carbonate laminae	5
NP18A06	20-26 mm	red/black jelly mat + carbonate laminae	
NP18A07	26-29 mm	black jelly mat + micritic carbonate	
NP18A08	29-33 mm	dark mat with carbonate laminae	
NP18A09	33-37 mm	crusty carbonate	
NP18A10	37-40 mm	dark jelly mat with round carbonate grains	
NP18A11C	40 mm	gastropod shell	
NP18A11A	40-58 mm	blue-grey, sturdy jelly with undulating thin black mat laminae	
NP18A11B	40-58 mm	same as previous	
NP18A12	58-60 mm	leathery dark mats, peeling off	12
NP18A13	60-65 mm	leathery dark mats	13
NP18A14	65-70 mm	leathery dark mats	14
NP18A15	70-85 mm	silt/sand with a few dark thin mat fragments in	
NP18A16A	85-98 mm	silt/sand	
NP18A16B	95 mm	2 gastropod shells	
NP18A17	98-105 mm	brown mat	
NP18A18A	105-175 mm	oid sand, large intraclast of mat flipped vertically	
NP18A18B	105-175 mm	same as above, plastic bag	
NP18A19	175-185 mm	sand with inmix of organics	
NP18A20	185-190 mm	dark mat layers	20
NP18A21	190-195 mm	sand	
NP18A22	195-200 mm	dark thicker (2mm) mat layers	22
NP18A23	200-206 mm	fine mat laminae	23
NP18A24	206-213 mm	sand	
NP18A25	213-220 mm	dark mat	25
NP18A26	220-232 mm	mat mixed with sand, some crude lamination	
NP18A27A	232-265 mm	sand, at 25 mm crude organic layer	
NP18A27B	232-265 mm	same as previous, bag	
NP18A27C	255 mm	shell fragment, diameter 5 mm	

4.1.4 SEM subsamples

SEM analyses of the NP18A subsamples reveal further details of the mineral morphology and composition. Backscatter electron images from chosen features in subsamples S1-S12 are presented in figure 21-39. Depths for each sample is presented in Table 4. Because the original layering has been partially destroyed in the sample process, the features are not exactly marked out where they were found. Complementary backscatter electron images are provided in Appendix C).

Elemental spectra from SEM analyses of chosen features are marked in the figures and are summarized in table 5 where the values are normalized without Au. Elemental maps show the distribution of C, Ca, Fe, K, Na, O, P, S and Sb in an OM-rich part of sample S1 (Fig.21). Ca represents the carbonate rich parts and C the organic matter rich parts. O, P, S, K and Na is concentrated in the organic matter and Sb is concentrated in the calcium carbonate area, while Fe show no preferred concentration pattern. Strong S-concentration represents gypsum crystals.

Both CaCO₃ (Fig. 26) and gypsum (Fig. 25) is found nucleating within organic material (OM) in the upper part of the core (sample S1), though most gypsum occur mostly as small (~5-25 µm) prismatic crystals on top of rather than within OM (Fig. 22). Small (~250 µm) shell parts (Fig. 24) and diatoms in the size of ~30 µm (Fig. 25) occur occasionally. Carbonate occur mainly as rods and spherulites. Rods develop within or on organic material and by continued growth evolve into dumbbell-shapes and spherulites.

Single calcium carbonate rods which precipitates with random orientations develop into dumbbells that cluster together and assemble in shapeless multi-clusters.

The size of dumbbell-shapes varies. The size of dumbbell-shapes at spectrum 45 (S1) and spectrum 52 (S2) is ~15 µm (Fig. 26), while other rods in S2 have a uniform size of ~7 µm (Fig. 28). Calcium carbonate spherulites originate either as small rounded carbonate grains or rods, that develop into spherulites by on-growths in multiple directions with a starry appearance. Spherulites do appear in both rounded and shapeless clusters already in the top part of the core, in S1 (0-12 mm) there are examples of spherulite sizes of ~5-10 µm and cluster sizes of ~25-50 µm (Fig. 24). Other occasional calcium carbonate morphologies can be found, for example a carbonate “star” ~45 µm in diameter in sample S1 (Fig. 27) and carbonate particles ~1 µm (Fig. 37). Deeper in the sediment there is a trend towards more on-growth on dumbbells and larger clusters, although there is an inmix of smaller rods too. Occasional gypsum needle bundles (Fig, 33) and framboidal pyrite clusters (Fig. 35) are found at depths below 2,5 cm.

Table 4: Depths in core NP18A of sample S1-S12.

Sample	Depth (mm)
S1	0-12
S2	13-23
S3	24-33
S4	34-44
S5	45-55
S6	56-66
S7	67-76
S8	102-110
S9	184-194
S10	195-204
S11	205-213
S12	214-223

Table 5: Normalized (tot. wt% 100) elemental composition in wt% summarized from SEM elemental spectrum analyses of subsamples from core NP18A.

Samp., spectr.	Feature	Ca (wt%)	O (wt%)	Mg (wt%)	Na (wt%)	S (wt%)	Sr (wt%)	Fe (wt%)	Si (wt%)	K (wt%)
S1, 45	rod	58,6	33,3	3,4		2,3			2,3	
S1, 42	spherulite	56,1	37,8	3,7		2,4				
S1, 39	shell part	89,1	10,9			0,0				
S1, 36	gypsum	64,4	12,2			23,3				
S1, 37	gypsum	35,1	25,8		3,1	33,0				3,1
S1, 44	gypsum	39,6	28,6			30,8			1,1	
S2, 51	rod	53,3	41,3	3,3		2,2				
S2, 49	star	54,8	45,2			0,0				
S2, 52	dumbbell	63,0	31,5	3,3		2,2				
S4, 53	gypsum	38,7	32,3	0,0		29,0				
S5, 40	spherulite	58,9	34,4	4,4		2,2				
S5, 54	spherulite cluster	71,1	25,8	1,0		1,0	1,0			
S5, 55	spherulite cluster	55,8	37,9	3,2		2,1	1,1			
S7, 56	rod	61,7	33,0	3,2		2,1				
S8, 1	pyrite	4,7	3,5	0,0		47,7		44,2		
S9, 12	rod cluster	51,6	38,9	7,4		2,1				
S10, 14	particles	36,3	42,5	12,5		1,3			7,5	
S10, 16	rod	47,2	46,1	6,7		0,0				
S11, 18	gypsum	22,6	42,9	10,7	2,4	21,4				
S12, 28	spherulite	52,6	37,9	7,4		2,1				

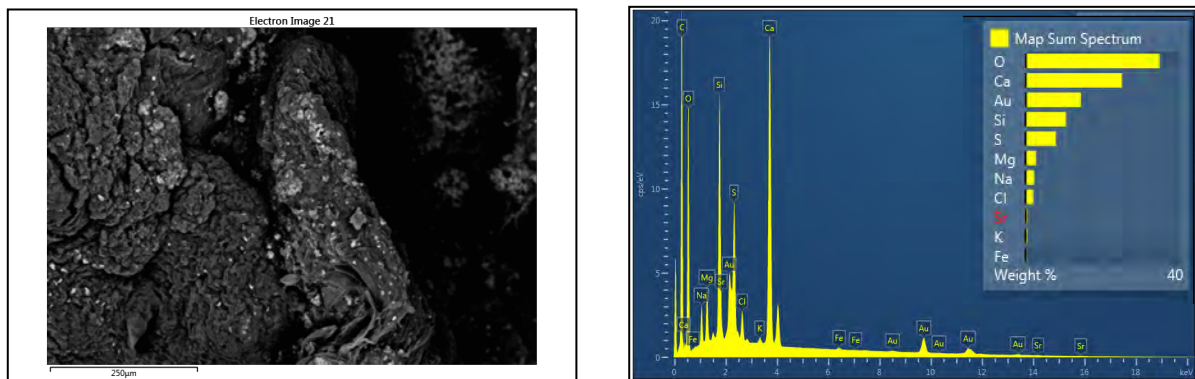
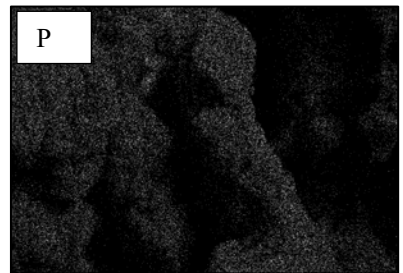
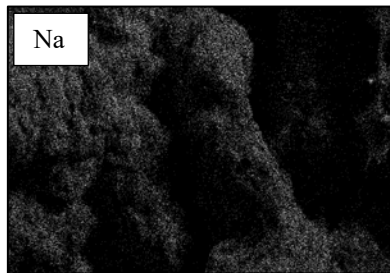
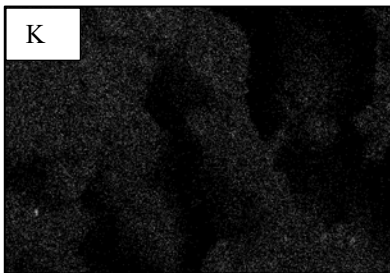
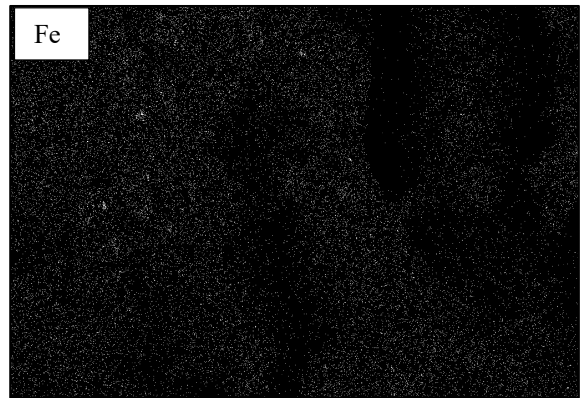
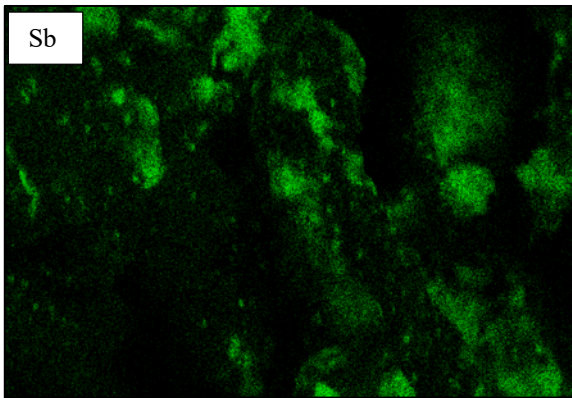
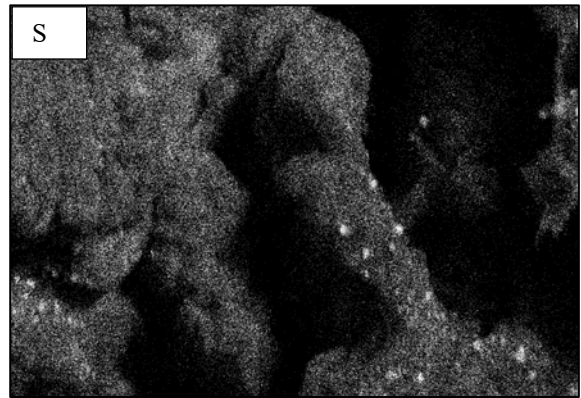
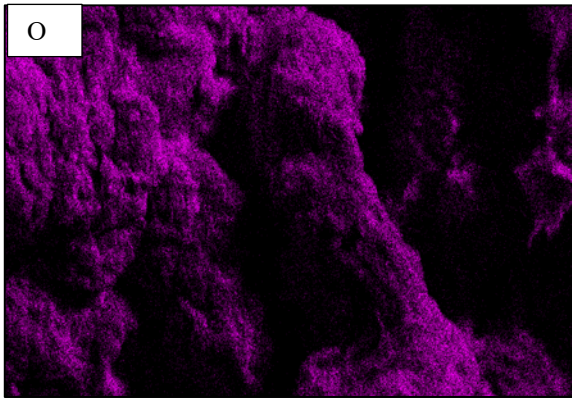
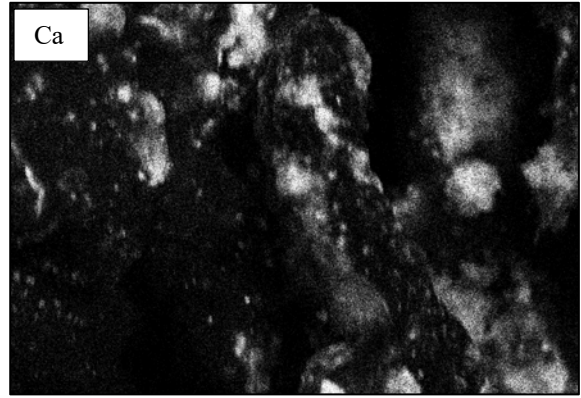
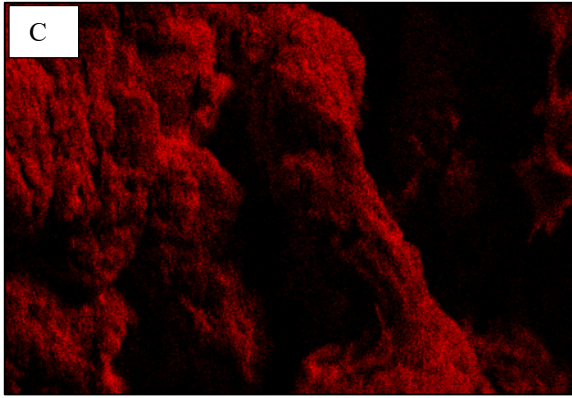


Figure 21, Above: Backscatter electron image from SEM analysis (left) of subsample S1 from core NP18A on carbonate and gypsum and map sum spectrum for the image area (right). Below: Map data for C, Ca, Fe, K, Na, O, P, S and Sb.



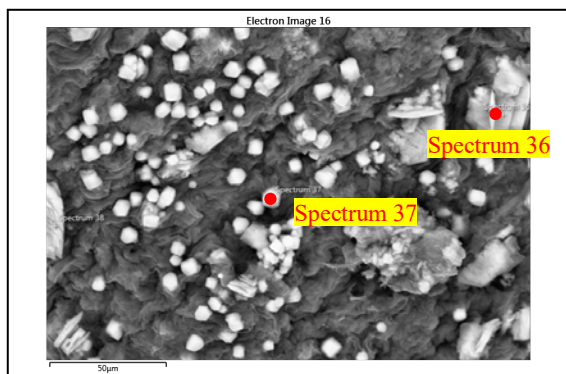


Figure 22: Backscatter electron image of subsample S1 from core NP18A. Gypsum crystals within organic material, size ~ 5-25 µm. Elemental spectra are summarized in table 5.

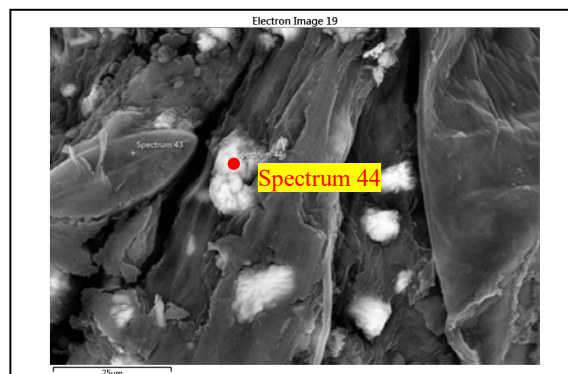


Figure 25: Backscatter electron image from SEM analysis of subsample S1 from core NP18A. Diatom in the left side ~30 µm and gypsum clusters enclosed within organic material ~5-15 µm. Elemental spectra are summarized in table 5.

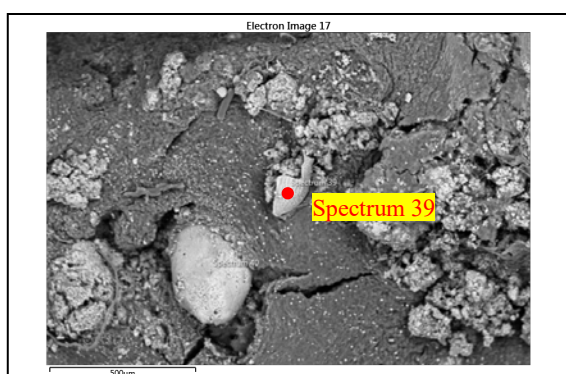


Figure 23: Backscatter electron image from SEM analysis of subsample S1 from core NP18A. Calcite shell parts within organic material, size ~250 µm. Elemental spectra are summarized in table 5.

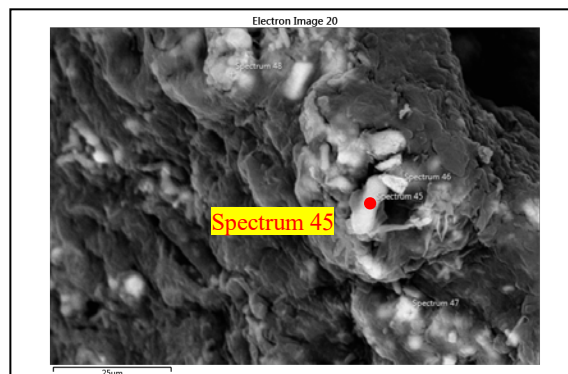


Figure 26: Backscatter electron image from SEM analysis of subsample S1 from core NP18A. Size of dumbbell-shape at spectrum 45 ~15 µm and size of carbonate cluster at spectrum 47 ~5 µm. Elemental spectra are summarized in table 5.

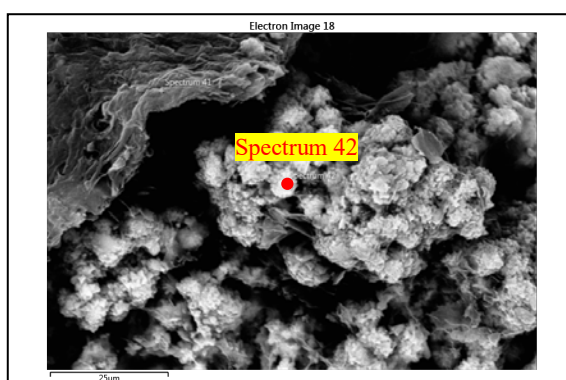


Figure 24: Backscatter electron image from SEM analysis of subsample S1 from core NP18A. Carbonate crystal spherulite cluster within organic material, size of spherulites ~5-10 µm and size of clusters ~25-50 µm. Elemental spectra are summarized in table 5.

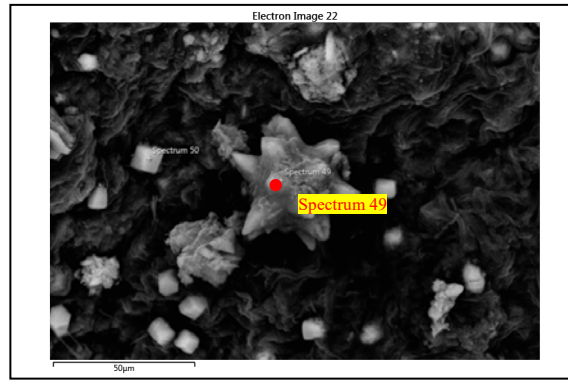


Figure 27: Backscatter electron image from SEM analysis of subsample S1 from core NP18A with carbonate "star" ~ 45 µm in diameter; and gypsum crystals ~ 5 µm on organic material. Elemental spectra are summarized in table 5.

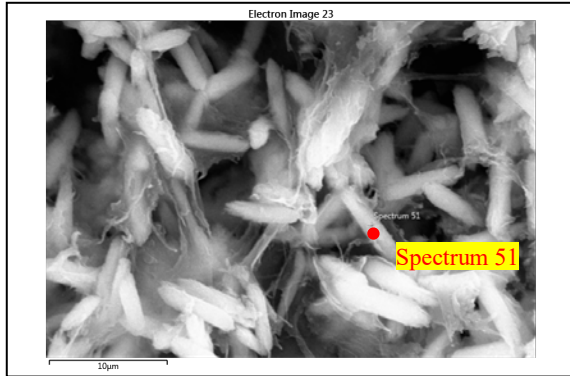


Figure 28: Backscatter electron image from SEM analysis of subsample S2 from core NP18A showing carbonate rods with uniform size of $\sim 7 \mu\text{m}$. Elemental spectra are summarized in table 5.

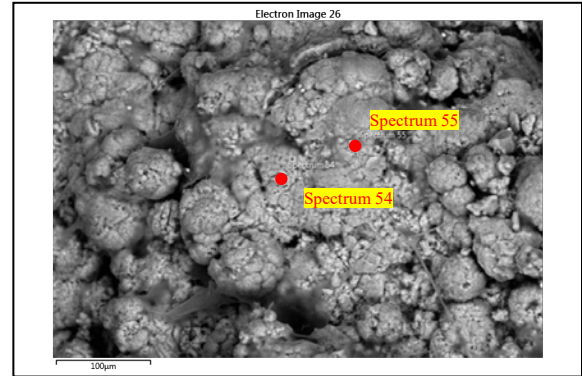


Figure 31: Backscatter electron image from SEM analysis of subsample S5 from core NP18A showing merged carbonate cluster spherules. Size of spherules $\sim 50 - 90 \mu\text{m}$. Elemental spectra are summarized in table 5.

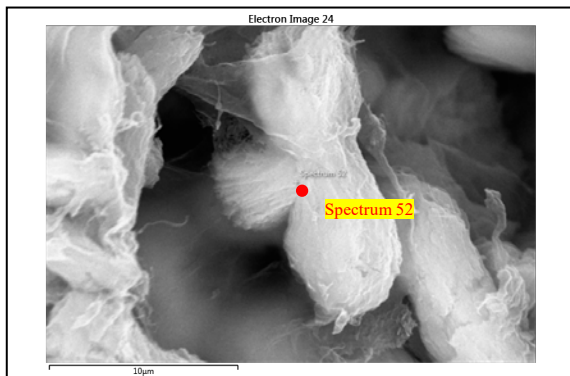


Figure 29: Backscatter electron image from SEM analysis of subsample S2 from core NP18A showing a carbonate dumbbell with an outgrowth on the middle. Size of dumbbell $\sim 15 \mu\text{m}$. Elemental spectra are summarized in table 5.

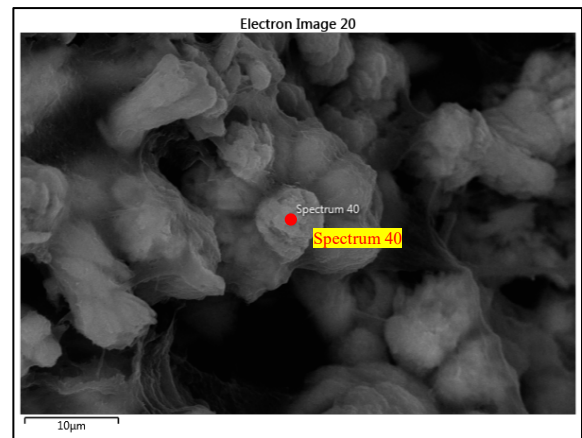


Figure 32: Backscatter electron image from SEM analysis of subsample S5 from core NP18A showing carbonate rod/dumbbell clusters, size of individual rods $\sim 15 \mu\text{m}$. Spectrum 40 showing composition of carbonate.

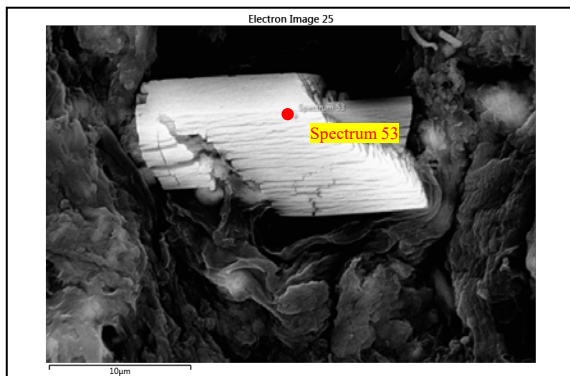


Figure 30: Backscatter electron image from SEM analysis of subsample S4 from core NP18A showing a gypsum crystal with cracks. Size of crystal $\sim 20 \mu\text{m}$. Elemental spectra are summarized in table 5.

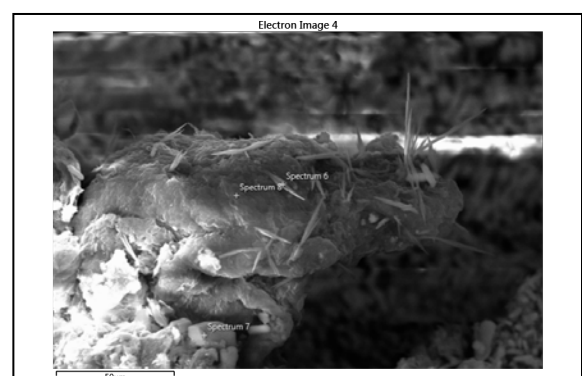


Figure 33: Backscatter electron image from SEM analysis of subsample S6 from core NP18A showing gypsum needles $\sim 20-25 \mu\text{m}$ on organic material.

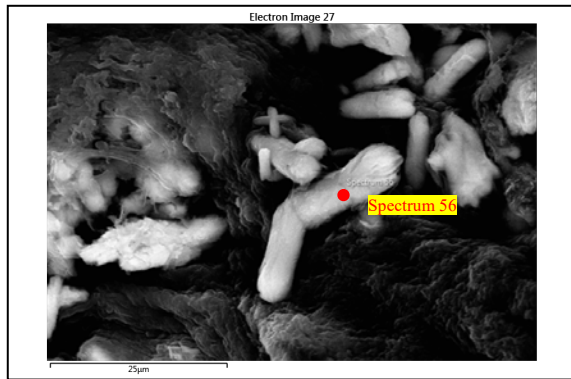


Figure 34: Backscatter electron image from SEM analysis of subsample S7 from core NP18A showing carbonate rods in various sizes 5-20 μm of which some are grown together, some have outgrowths and one is cross-shaped. Elemental spectra are summarized in table 5.

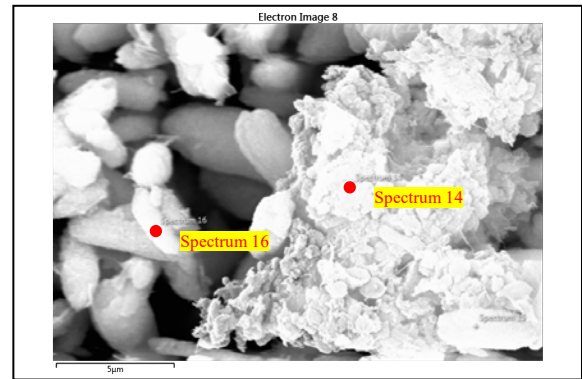


Figure 37: Backscatter electron image from SEM analysis of subsample S10 from core NP18A showing clustered carbonate particles $\sim 1 \mu\text{m}$ and carbonate rods. Size of rod at spectrum 16 $\sim 3 \mu\text{m}$. Elemental spectra are summarized in table 5.

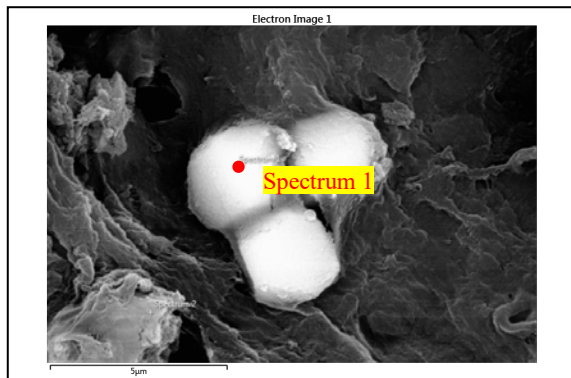


Figure 35: Backscatter electron image from SEM analysis of subsample S8 from core NP18A showing framboidal pyrite. Size of individual pyrite crystals $\sim 3 \mu\text{m}$. Elemental spectra are summarized in table 5.

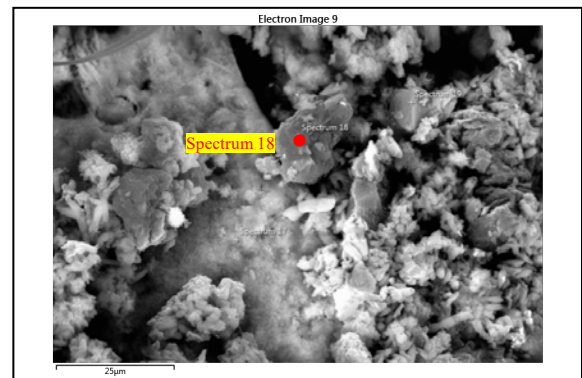


Figure 38: Backscatter electron image from SEM analysis of subsample S11 from core NP18A showing clustered carbonate particles and rods in size range $\sim 1-3 \mu\text{m}$ and gypsum- and Mg-rich particles 15-25 μm . Elemental spectra are summarized in table 5.

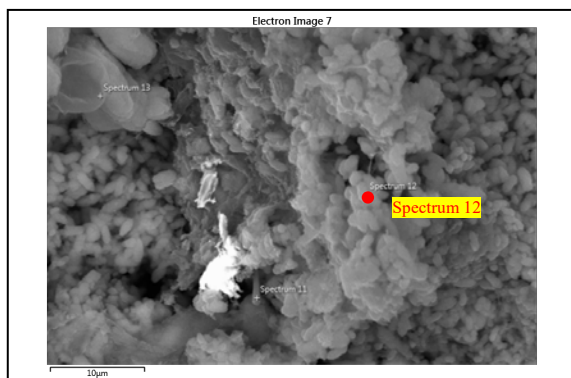


Figure 36: Backscatter electron image from SEM analysis of subsample S9 from core NP18A showing clustered carbonate rods. Size of individual rods $\sim 3 \mu\text{m}$. Elemental spectra are summarized in table 5.

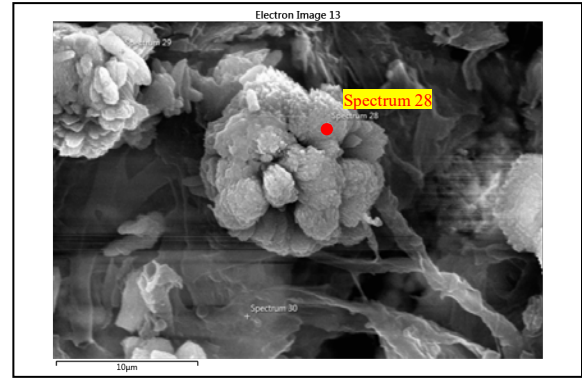


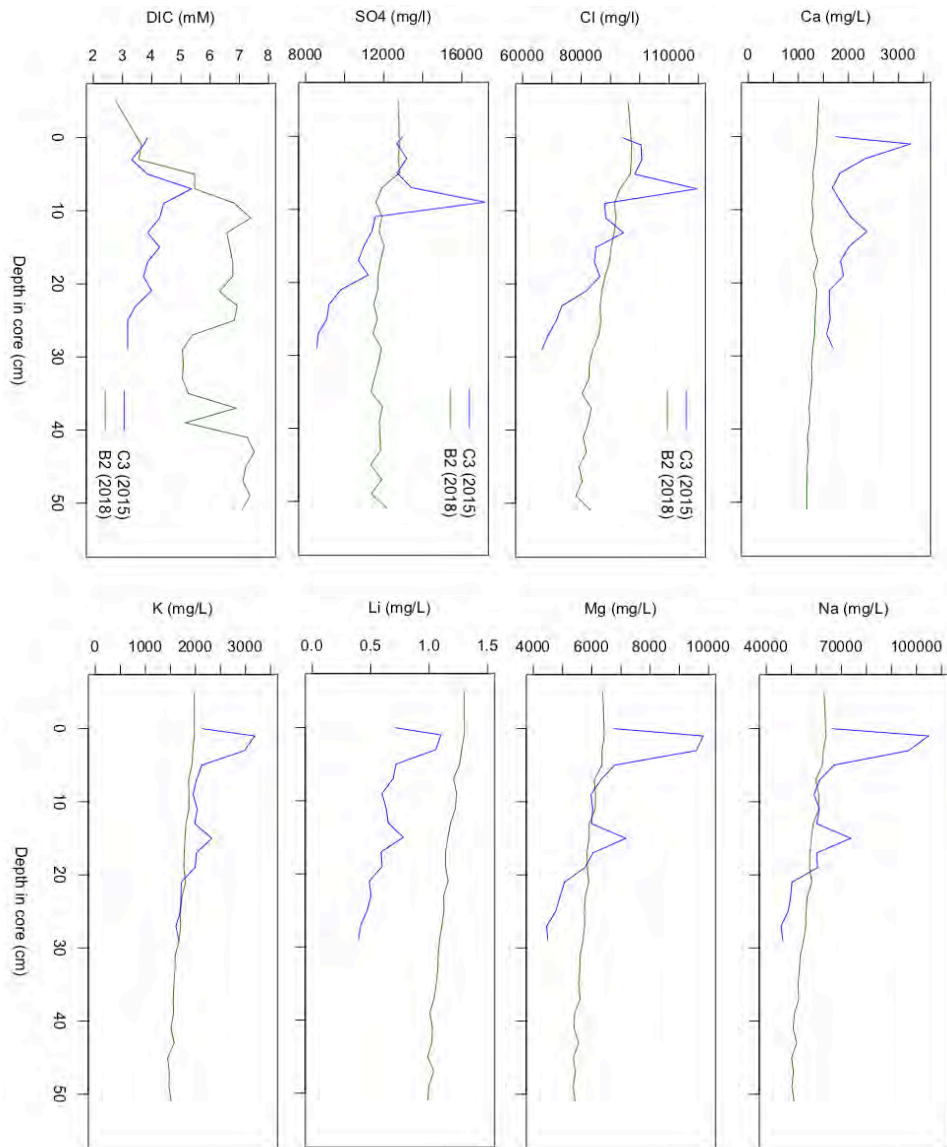
Figure 39: Backscatter electron image from SEM analysis of subsample S12 from core NP18A showing a carbonate cluster $\sim 12 \mu\text{m}$ in diameter. Elemental spectra are summarized in table 5.

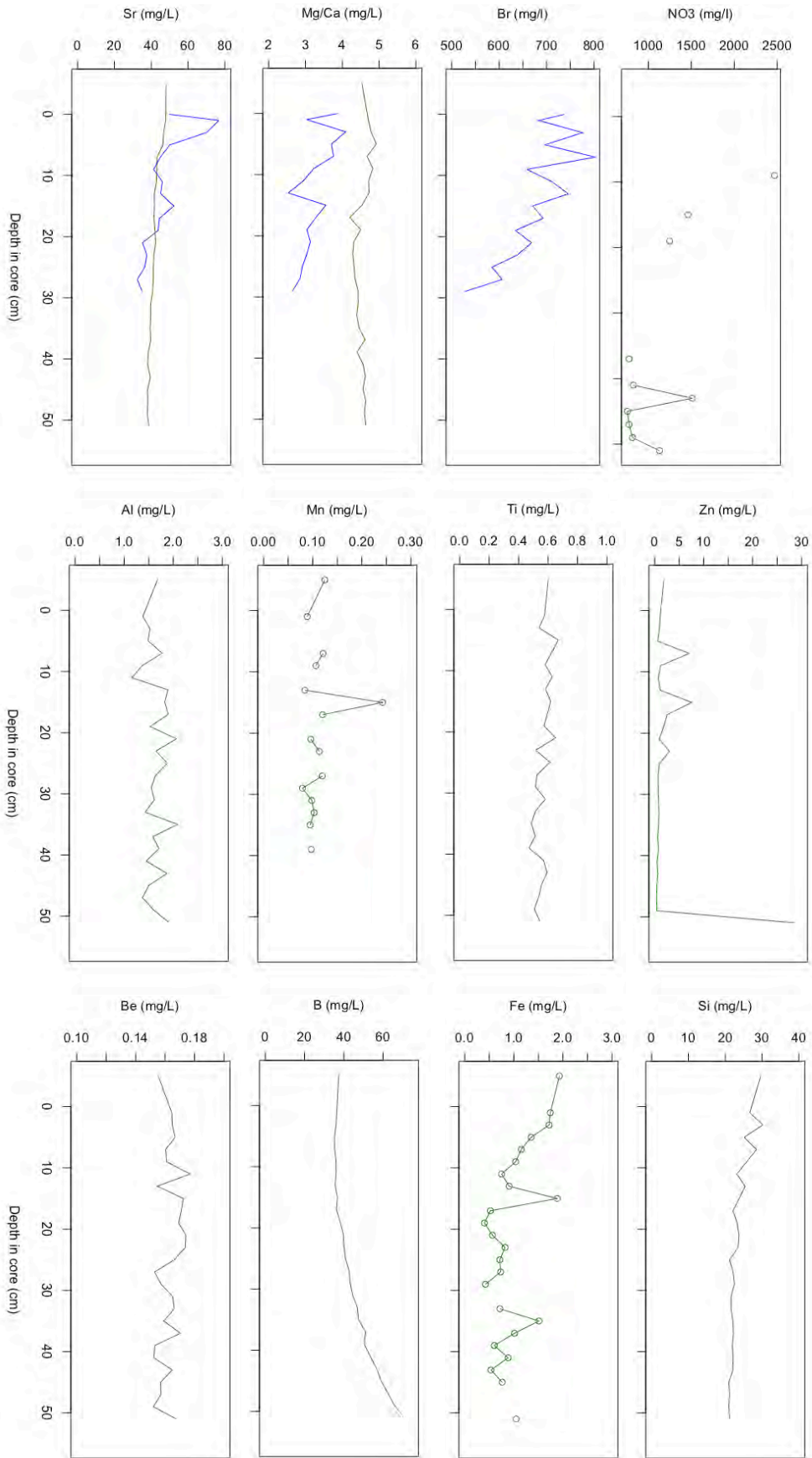
4.1.5 Porewater chemistry, Big Pond core C3 (2015) and Big Pond core B2 (2018)

Porewater was analyzed for dissolved inorganic carbon (DIC), cations and anions. Anions detected in core B2 was Cl, NO₃ and SO₄. Cations detected in core B2 was Al, B, Ba, Be, Ca, Fe, K, Li, Mg, Mn, Na, S, Si, Sr, Ti and Zn. Anions detected in core C3 was Cl, Br and SO₄. Cations detected in core C3 was Ca, K, Li, Mg, Na and Sr.

The results from core B2 (green) and C3 (blue) are presented together graphically (Fig.40). Each measured compound is presented in a separate graph. Some compounds were only found in one of the cores. Correlation matrices for dissolved inorganic carbon (DIC), anion and cation data of core C3 (2015) are shown in table 6 and core B2 in table 7.

Figure 40: Porewater DIC, anions and cations (SO₄, Cl, Ca, K, Li, Mg, Na, Mg/Ca, NO₃, Al, Mn, Ti, Zn, Be, B, Fe, Si, S and Ba) from core B2 (Big Pond, November 2018) are presented in green and (SO₄, Cl, Ca, K, Li, Mg, Na, Mg/Ca and Br) from C3A (Big Pond, July 2015) in blue.





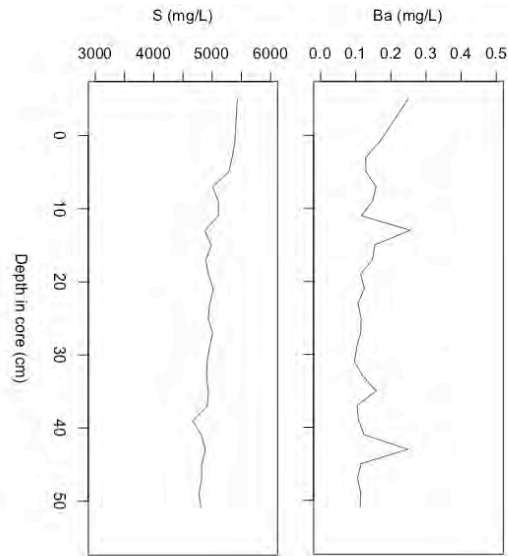


Table 6: Correlation matrix for dissolved inorganic carbon (DIC), anion and cation data of Big Pond core C3 (2015). Weak correlations between the presented elements are shown in pale gray, moderate correlations in dark gray and good correlations in black.

	Ca	K	Li	Mg	Na	Sr	Cl	Br	SO4
Ca	1,00								
K	0,86	1,00							
Li	0,82	0,98	1,00						
Mg	0,81	0,99	0,99	1,00					
Na	0,85	1,00	0,99	0,99	1,00				
Sr	0,86	0,99	0,99	0,99	1,00	1,00			
Cl	0,43	0,60	0,70	0,67	0,61	0,62	1,00		
Br	0,31	0,50	0,62	0,58	0,51	0,52	0,89	1,00	
SO4	0,32	0,47	0,53	0,54	0,48	0,46	0,69	0,58	1,00
DIC	-0,01	0,07	0,17	0,14	0,08	0,07	0,70	0,61	0,58

Table 7: Correlation matrix for dissolved inorganic carbon (DIC), anion and cation data of Big Pond core C3 (2015). Weak correlations between the presented elements are shown in pale gray, moderate correlations in dark gray and good correlations in black.*Pairwise complete observations.

	B	Ca	K	Li	Mg	Na	S	Si	Sr	Cl	NO3*	SO4
B	1,00											
Ca	-0,83	1,00										
K	-0,87	0,80	1,00									
Li	-0,84	0,76	0,98	1,00								
Mg	-0,81	0,74	0,98	0,99	1,00							
Na	-0,85	0,77	0,99	0,99	0,99	1,00						
S	-0,63	0,67	0,85	0,90	0,92	0,88	1,00					
Si	-0,63	0,55	0,83	0,85	0,85	0,83	0,80	1,00				
Sr	-0,74	0,76	0,95	0,96	0,98	0,96	0,96	0,86	1,00			
Cl	-0,80	0,72	0,97	0,96	0,97	0,97	0,85	0,85	0,95	1,00		
NO3*	-0,62	0,61	0,84	0,81	0,85	0,83	0,86	0,88	0,82	0,79	1,00	
SO4	-0,31	0,36	0,63	0,65	0,71	0,65	0,75	0,67	0,77	0,74	0,04	1,00
DIC	0,41	-0,54	-0,51	-0,54	-0,55	-0,51	-0,66	-0,63	-0,65	-0,51	-0,35	-0,58

4.2 ITRAX data

4.2.1 Core BPC7A

Core BPC7A was scanned for Al, Si, P, S, CL, Ar, K, Ca, Ti, V, Cr, Fe, Ni, Cu, Zn, Br, Sr, Zr and Sb. A correlation matrix of the analyzed elements is presented in table 4. Elements with a significant positive correlation (p-value < 2.2e-16) with $r = 75$ or higher are presented in bold black in table 4 and in correlation plots in figure 41; Sb-

Ca (r^2 0.77) and Fe-Ti (r^2 0.74). Elements with a significant negative correlation (p-value < 2.2e-16) and with $r < -75$ or lower are presented in bold black in table 8 and in correlation plots in figure 42; Br-Sr (r^2 0.59) and Br-Ca (r^2 0.56). Moderate positive correlation (r between 50 and 74) and negative correlations (r between -50 and -74) are presented in dark gray in table 9. Of the elements that show similar or opposite peak patterns; a few are presented graphically together with an image of the core in figure 43,44 and 45.

Table 8: Correlation matrix for the ITRAX data of Big Pond core BPC7A. Elements with only weak correlations (r between -49 and 49) are eliminated from the table. Weak correlations between the presented elements are shown in pale gray, moderate correlations in dark gray and good correlations in black.

	Si	P	K	Ca	Ti	Fe	Ni	Cu	Br	Sr
Si	1,00									
P	-0,28	1,00								
K	-0,15	0,26	1,00							
Ca	0,48	-0,61	-0,24	1,00						
Ti	-0,03	0,01	0,40	0,01	1,00					
Fe	-0,02	-0,01	0,36	0,02	0,86	1,00				
Ni	-0,25	0,36	0,09	-0,56	-0,11	-0,06	1,00			
Cu	-0,43	0,40	0,69	-0,37	0,48	0,44	0,15	1,00		
Br	-0,52	0,64	0,51	-0,75	0,26	0,26	0,51	0,73	1,00	
Sr	0,46	-0,55	-0,27	0,65	-0,22	-0,19	-0,37	-0,51	-0,77	1,00
Zr	0,13	-0,09	0,01	0,09	-0,04	-0,01	-0,11	-0,03	-0,21	0,51
Sb	0,37	-0,52	-0,33	0,88	-0,03	0,01	-0,49	-0,31	-0,64	0,53

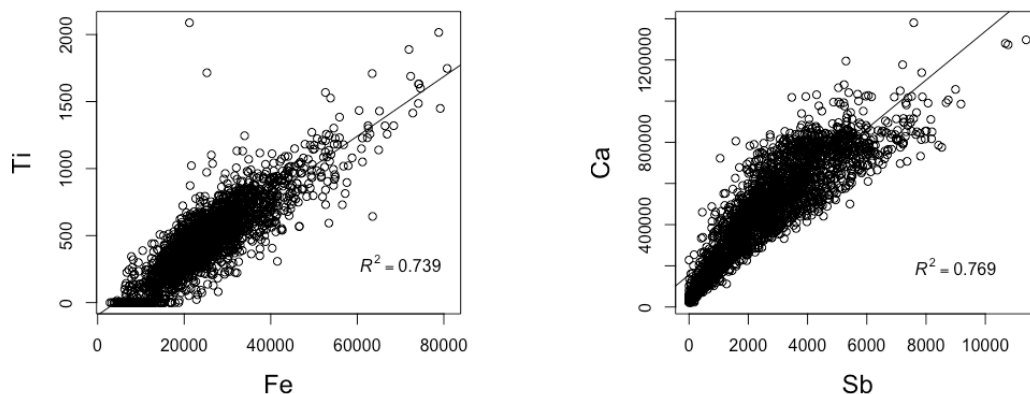


Figure 41: Correlation plots of elemental ITRAX data for core BPC7A for significant (p-value < 2.2e-16) positive correlation of Ti-Fe (r^2 0.74) and Ca-Sb (r^2 0.77).

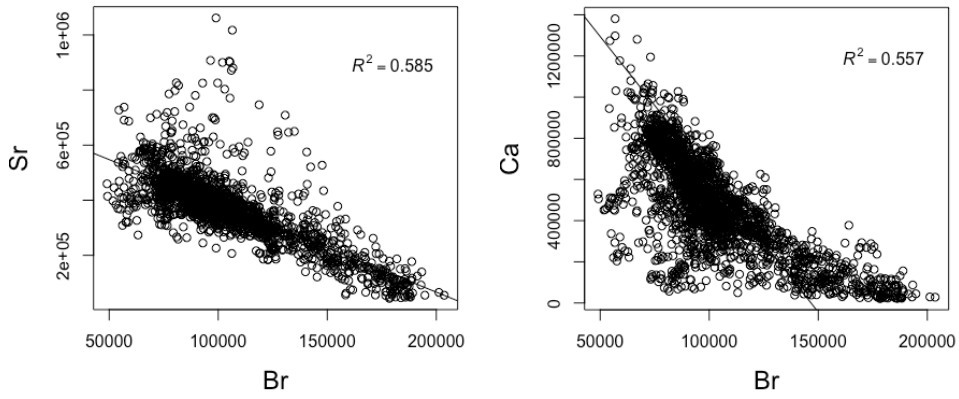


Figure 42: Correlation plots of elemental ITRAX data for core BPC7A for significant (p -value $< 2.2e-16$) negative correlation of Sr-Br (r^2 0.59) and Ca-Br (r^2 0.56).

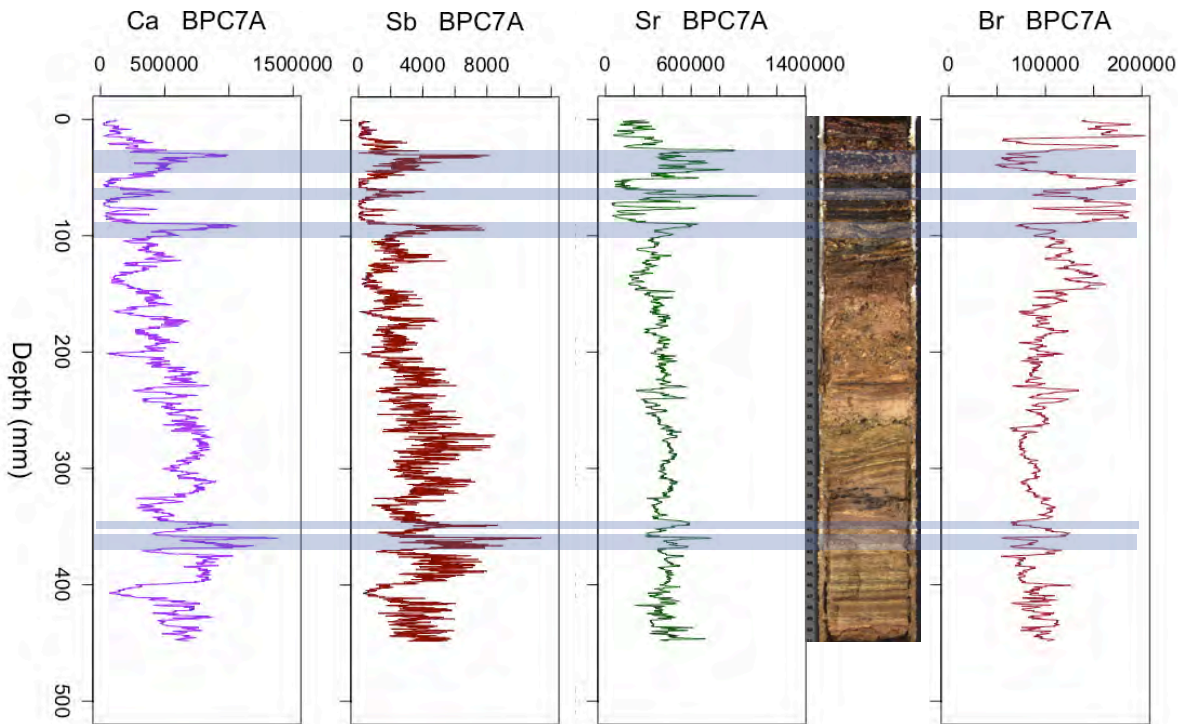


Figure 43: Variation of elemental ITRAX data with depth for Ca, Sb, Sr and Br in core BPC7A adjacent to a photograph of the core. Blue shaded areas highlight a few of the correlations between the four elements and the appearance of the core.

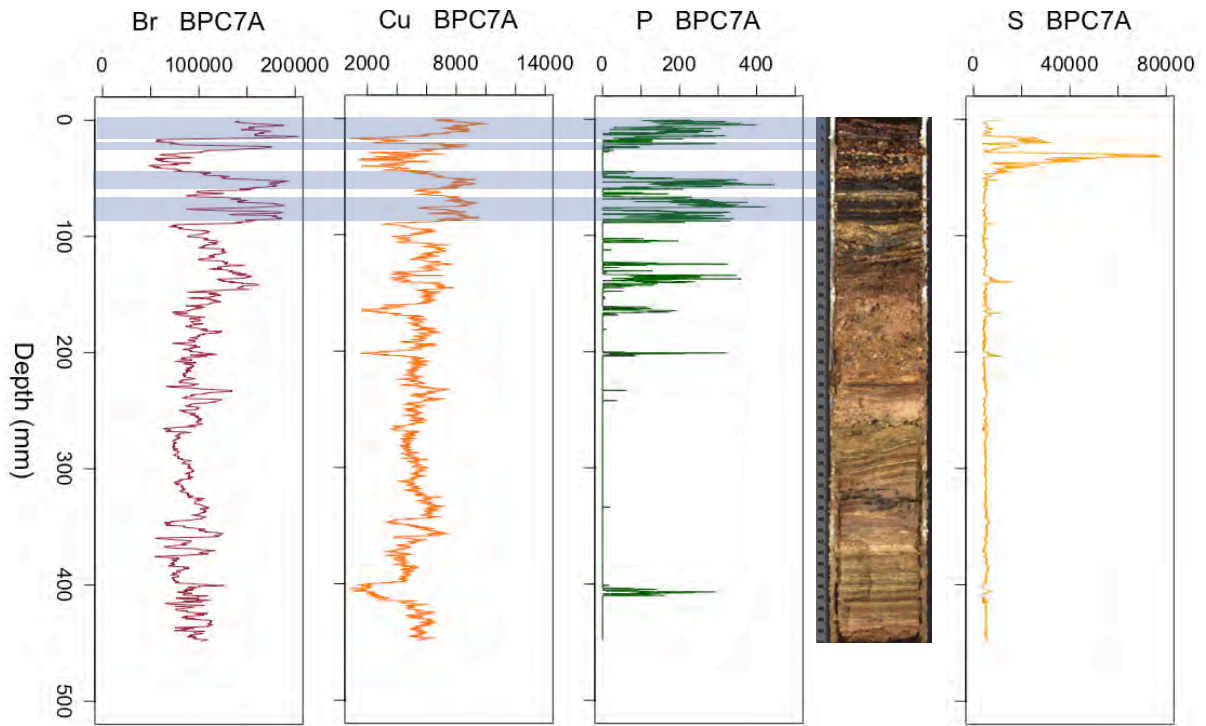


Figure 44: Variation of elemental ITRAX data with depth for Br, Cu, P and S in core BPC7A adjacent to a photograph of the core. Blue shaded areas highlight a few of the correlations between the elements and the appearance of the core.

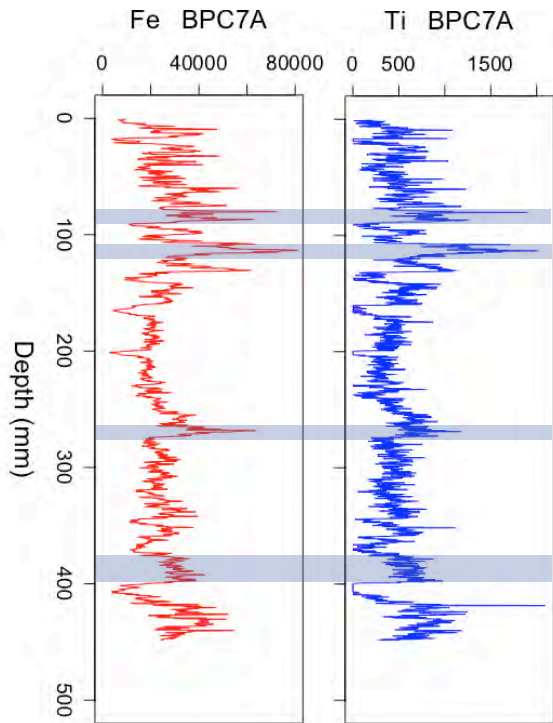


Figure 45: Variation of elemental ITRAX data with depth for Fe and Ti in core BPC7A. Blue shaded areas highlight a few of the correlations between Fe and Ti.

4.2.2 Core NP18B

Core NP18B was scanned for Al, Si, P, S, Cl, Ar, K, Ca, Sc, Ti, V, Cr, Mn, Fe, Ni, Cu, Zn, Ga, As, Br, Sr, Y, Zr, In, Sb, Ba and Pb. A correlation matrix of the analyzed elements is presented in table 9 and 10. Elements with a significant positive correlation (p -value $< 2.2e-16$) and with $r = 75$ or higher are presented in bold black in table 5 and 6 and in correlation plots in figure 46; Br-Cu (r^2 0.83), Ca-Si (r^2 0.72), Sc-Ca (r^2 0.60), Fe-Ti (r^2 0.65), Ga-Br (r^2 0.58), Zr-Cu (r^2 0.60), Zr-Ga (r^2 0.64) and Zr-Br (r^2 0.67). Elements with a significant

negative correlation (p -value $< 2.2e-16$) and with r -75 or lower are presented in bold black in table 5 and 6 and in correlation plots in figure 47; Cu-Si (r^2 0.56), Cu-Ar (r^2 0.70), Cu-Ca (r^2 0.60), Br-Si (r^2 0.58), Br-Ar (r^2 0.69), Br-Ca (r^2 0.68). Moderate positive correlations (r between 50 and 74) and negative correlations (r between -50 and -74) are presented in dark grey in table 9 and 10. Of the elements that show similar or opposite peak patterns; a few are presented graphically together with an image of the core in figure 48 and 49. The remaining elements are presented graphically in Appendix A).

Table 9: Correlation matrix for elemental ITRAX data for core NP18B. Elements with only weak correlations (r between -49 and 49) are eliminated from the table. Weak correlations between the presented elements are shown in pale gray, moderate correlations in dark gray and good correlations in black.

	Al	Si	P	S	Cl	Ar	K	Ca	Sc	Ti
Al	1,00									
Si	0,64	1,00								
P	-0,30	-0,53	1,00							
S	0,28	0,30	-0,13	1,00						
Cl	0,15	0,07	0,00	0,67	1,00					
Ar	0,35	0,56	-0,46	-0,09	-0,10	1,00				
K	-0,15	-0,26	0,13	0,42	0,50	-0,55	1,00			
Ca	0,63	0,85	-0,52	0,11	-0,18	0,61	-0,51	1,00		
Sc	0,46	0,63	-0,53	0,09	-0,10	0,46	-0,40	0,77	1,00	
Ti	-0,14	-0,04	-0,14	0,08	0,03	-0,24	0,56	-0,25	-0,18	1,00
Cr	-0,08	-0,15	0,02	0,01	-0,11	-0,56	0,42	-0,16	-0,02	0,38
Mn	0,32	0,57	-0,50	0,21	-0,08	0,25	0,06	0,54	0,58	0,28
Fe	-0,04	0,08	-0,22	0,16	0,03	-0,23	0,44	-0,07	0,02	0,81
Cu	-0,50	-0,75	0,58	-0,15	-0,11	-0,84	0,48	-0,78	-0,65	0,29
Ga	-0,33	-0,61	0,69	-0,10	-0,08	-0,65	0,26	-0,56	-0,54	-0,06
Br	-0,46	-0,76	0,64	-0,01	0,14	-0,83	0,54	-0,82	-0,70	0,21
Sr	0,48	0,61	-0,42	0,08	0,00	0,48	-0,42	0,70	0,59	-0,31
Zr	-0,41	-0,71	0,73	-0,19	-0,09	-0,61	0,25	-0,67	-0,67	0,00
In	0,24	0,39	-0,18	0,12	-0,05	0,19	-0,52	0,46	0,51	-0,19
Sb	0,42	0,68	-0,41	0,17	-0,10	0,41	-0,40	0,72	0,63	-0,10
Pb	0,19	0,34	-0,46	-0,19	-0,21	0,60	-0,35	0,39	0,33	0,03

Table 10, continued from table 5: *Correlation matrix for elemental ITRAX data for core NP18B. Elements with only weak correlations (r between -49 and 49) are eliminated from the table. Weak correlations between the presented elements are shown in pale gray, moderate correlations in dark gray and good correlations in black.*

	Mn	Fe	Ni	Cu	Ga	Br	Sr	Zr	In
Mn	1,00								
Fe	0,42	1,00							
Ni	-0,50	-0,07	1,00						
Cu	-0,44	0,15	0,61	1,00					
Ga	-0,47	-0,12	0,47	0,72	1,00				
Br	-0,52	0,07	0,59	0,91	0,76	1,00			
Sr	0,12	-0,22	-0,12	-0,58	-0,49	-0,68	1,00		
Zr	-0,52	-0,15	0,56	0,77	0,80	0,82	-0,66	1,00	
In	0,22	-0,04	-0,12	-0,33	-0,20	-0,34	0,31	-0,27	1,00
Sb	0,64	0,10	-0,40	-0,60	-0,45	-0,62	0,33	-0,52	0,65
Pb	0,18	-0,06	0,02	-0,43	-0,61	-0,56	0,41	-0,46	0,09

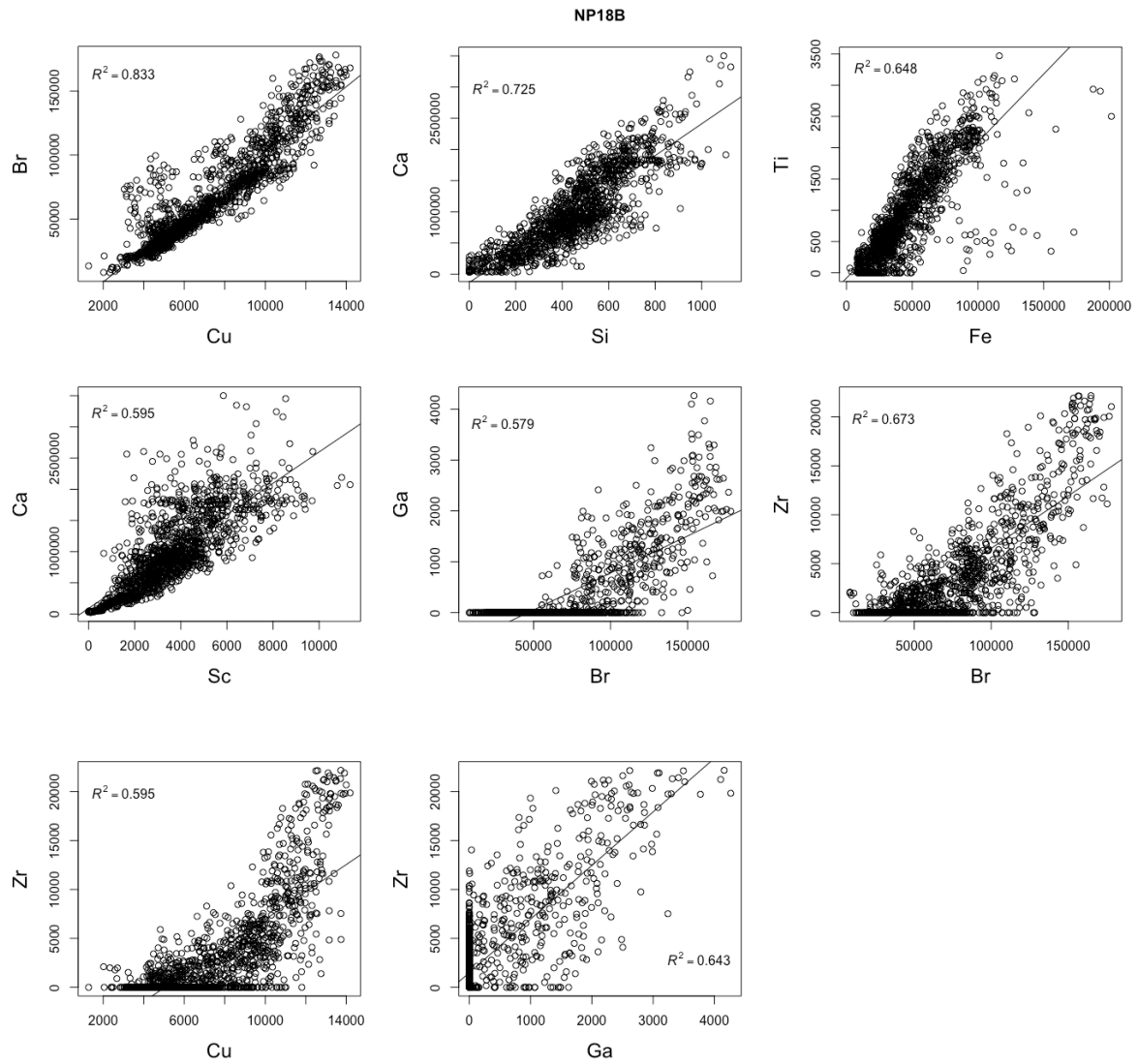


Figure 46: Correlation plots of elemental ITRAX data for core NP18B for significant (p -value $< 2.2e-16$) positive correlation of Br-Cu (r^2 0.83), Ca-Si (r^2 0.72), Sc-Ca (r^2 0.60), Fe-Ti (r^2 0.65), Ga-Br (r^2 0.58), Zr-Cu (r^2 0.60), Zr-Ga (r^2 0.64) and Zr-Br (r^2 0.67).

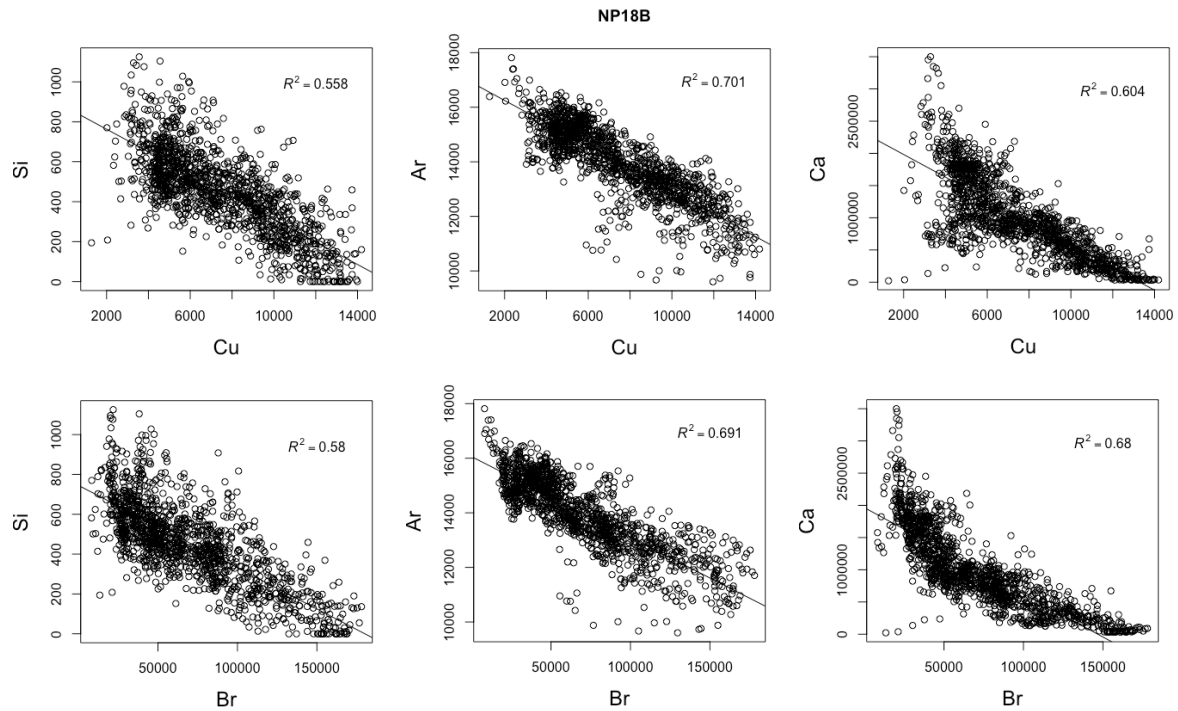


Figure 47: Correlation plots of elemental ITRAX data for core NP18B for significant (p -value $< 2.2e-16$) positive correlation of Cu-Si (r^2 0.56), Cu-Ar (r^2 0.70), Cu-Ca (r^2 0.60), Br-Si (r^2 0.58), Br-Ar (r^2 0.69), Br-Ca (r^2 0.68).

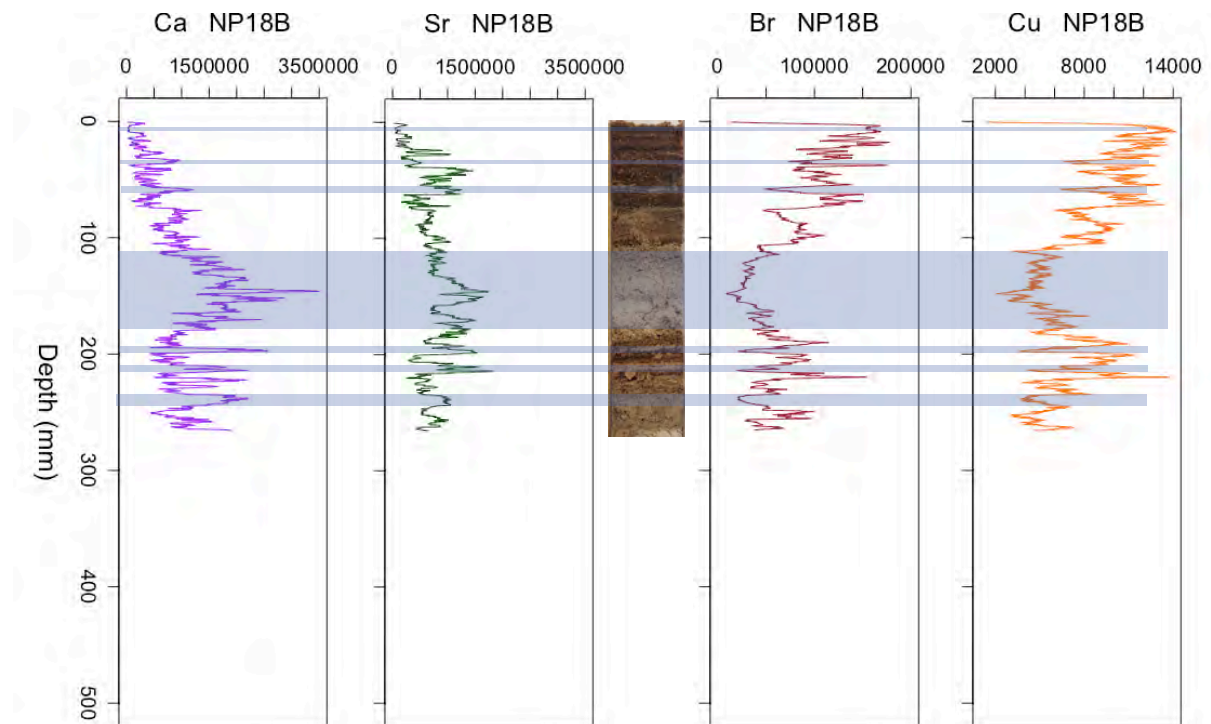


Figure 48: Variation of elemental ITRAX data with depth for Ca, Sr, Br and Cu in core NP18B adjacent to a photograph of the core. Blue shaded areas highlight a few of the correlations between the four elements and the appearance of the core.

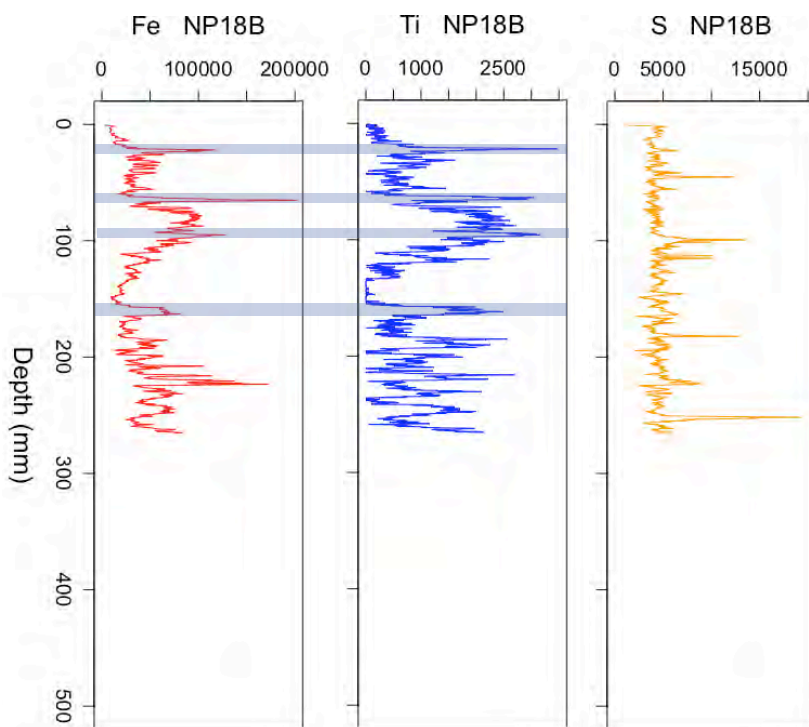


Figure 49: Variation of elemental ITRAX data with depth for Fe, Ti, and S in core NP18B. Blue shaded areas highlight a few of the correlations between Fe and Ti.

4.3 GDGT results and correlations

The species detected in the HPLCMS analysis were the isoprenoid GDGTs with mass over charge (m/z) 1302, 1300, 1298, 1296, 1292, and 1292r and the branched GDGTs with m/z 1050a-e, 1046, 1036 a-d, 1034 b,c,d,g, 1022 a-c, 1020 a,b, and 1018. The samples that are treated with acid hydrolysis (AH) represents the bulk GDGT content and core lipids (CL) represents fossil GDGTs. For sample NP18A04 and NP18A20 the core lipid results and for sample NP18A12 the acid hydrolysis results were not retrieved from the data analysis program. The results are presented in nanogram per gram freeze-dried sediment and the average depth of each sample is used in both correlation tables and graphical presentation of occurrence with depth of the most common GDGT species. Descriptions of the subsamples taken from core NP18A for lipid analysis are presented in table 3 and figure 20 in section 4.1.3 (*Core description NP18, New Pond 2018*).

Chromatograms that show where the different species eluate are presented in figure 51. The abundance of the different GDGT species for chosen depths is graphically presented in figure 52. The most abundant of the isoprenoid GDGT's (1302) and branched (1050e, 1022c and 1020a) are presented graphically with concentration of AH and CL with depth and the ratio of fossil (CL) to bulk (AH) GDGT's in (Fig. 53), and a principal component analysis plot of the most abundant GDGTs, average depth and the elements that show correlation to average depth (Fig.50)

Correlation of GDGT species with average depth and ITRAX element data are presented in table 12 and 13. Species and elements with only weak correlation values (r between -0,59 and 0,59) are eliminated from the tables. In the tables weak correlation values are light grey, moderate correlation values (r between -0,6 and -0,79/0,6 and 0,79) dark grey and good correlation values ($r > 80$ and < -80) are marked with bold black. The highest correlation values for table 12 and 13 are

presented with plots in figure 54 and 55. Adjusted r^2 , p-values for each correlation are presented in the captions. Correlation between GDGT species show various correlation. There are many correlations to 1302 AH, 1050e AH and 1046 AH, these are presented in table 11 A-C.

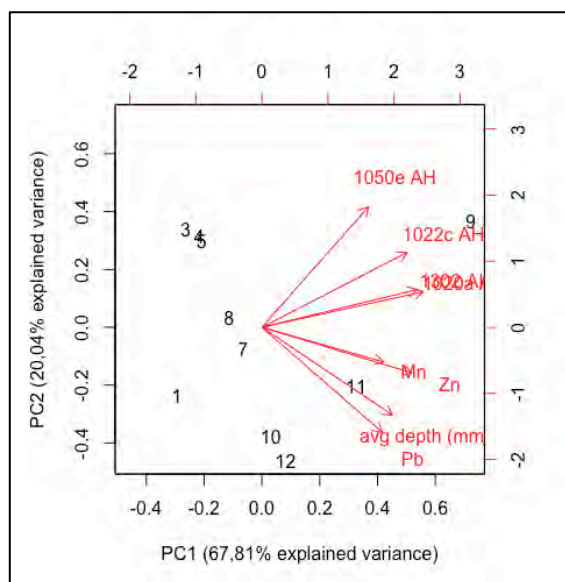


Figure 50: Principal component analysis of the most abundant GDGTs, average depth and the elements that show correlation to average depth. The most abundant species do not correlate very strong with depth.

Table 11: A) 1302 AH correlation to other GDGT species, B) 1050e AH correlation to other GDGT species, C) 106 AH correlation to other GDGT species.

1302 AH vs	Adj. R ²	p-value
1298 AH	0.7983,	5.54e-05
1296 AH	0.8159,	3.483e-05
1292 AH	0.8433,	1.539e-05
1292r AH	0.8704,	5.885e-06
1050a AH	0.8151,	3.567e-05
1046 AH	0.8697,	6.049e-06
1036d AH	0.6174,	0.001488
1034d AH	0.8002,	5.282e-05
1034g AH	0.796,	5.879e-05
1022c AH	0.7322,	0.0002357
1020a AH	0.9386,	1.365e-07
1020b AH	0.8747,	4.962e-06
1018 AH	0.8725,	5.417e-06

A

1046 AH vs	Adj. R ²	p-value
1018 AH	0.9996,	< 2.2e-16
1302 AH	0.8697,	6.049e-06
1298 AH	0.9183,	5.728e-07
1296 AH	0.9183,	5.728e-07
1292 AH	0.9793,	5.834e-10
1292r AH	0.9805,	4.386e-10
1050a AH	0.7119,	0.0003434

B

1050e AH vs	Adj. R ²	p-value
1298 AH	0.6109,	0.001626
1036c AH	0.9129,	7.913e-07
1036d AH	0.8284,	2.437e-05
1022b AH	0.9516,	4.125e-08
1022c AH	0.8146,	3.614e-05

C

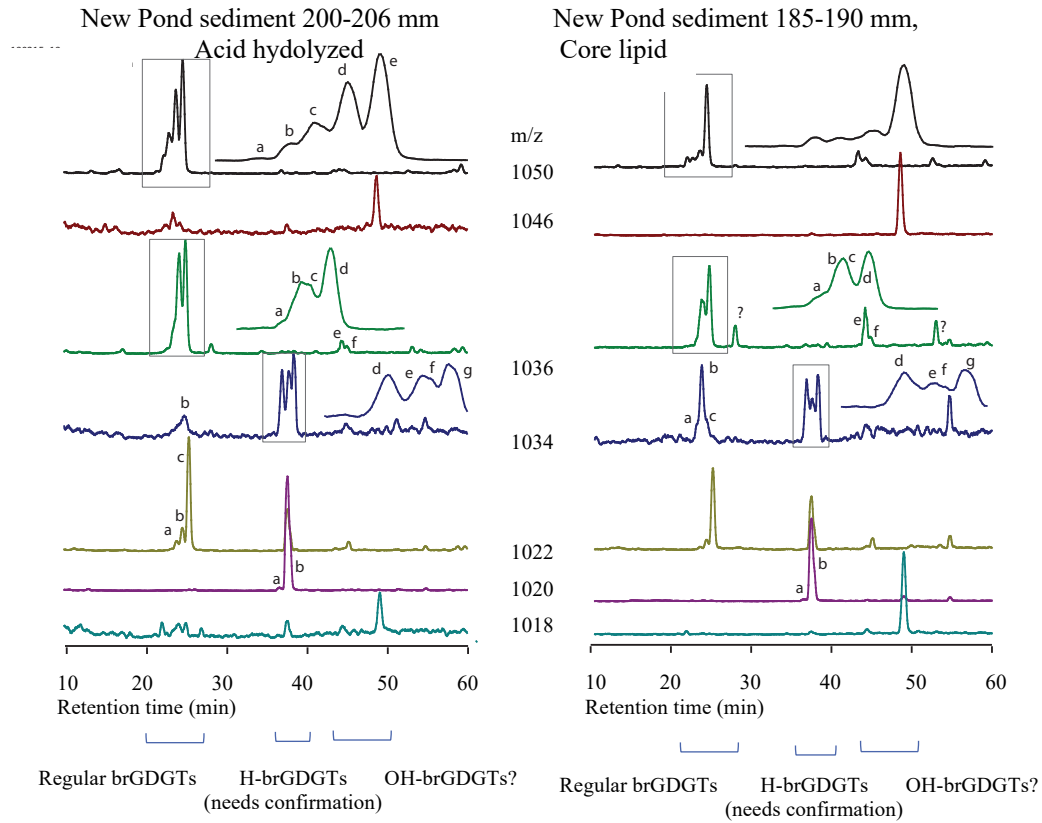


Figure 51: HPLC-MS ion chromatograms of one acid hydrolysed (left) and one core lipid (right) extract, showing the various branched GDGTs. Isoprenoid GDGTs are not shown. The brGDGTs elute in three groups, indicated by the grey boxes under the time axis: a) the ‘traditional’ brGDGTs published by Weijers et al (2007), b) H-shaped GDGTs, and c) hydroxy GDGTs. Groups 2 and 3 are tentatively assigned. Lowest panel shows the spread in the relative abundance of structural isomers of the hexamethyl GDGT 1050 between samples. The microbial and environmental meaning of these differences is subject to further investigation.

Figure 52, below: Abundance of GDGT species in ng/g sediment. A) 0-4 mm. B) 8-11 mm. C) 60-65 mm. D) 200-206 mm.

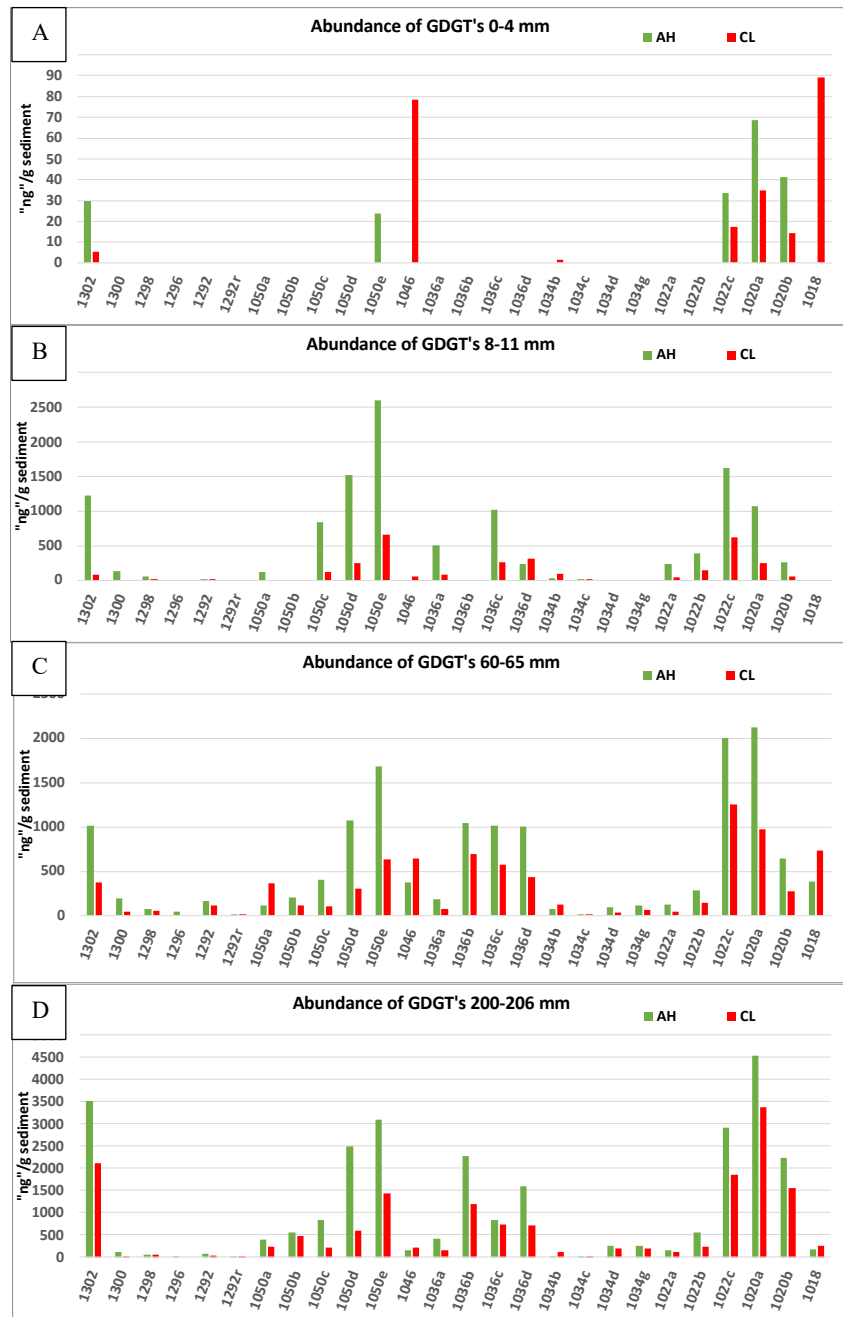
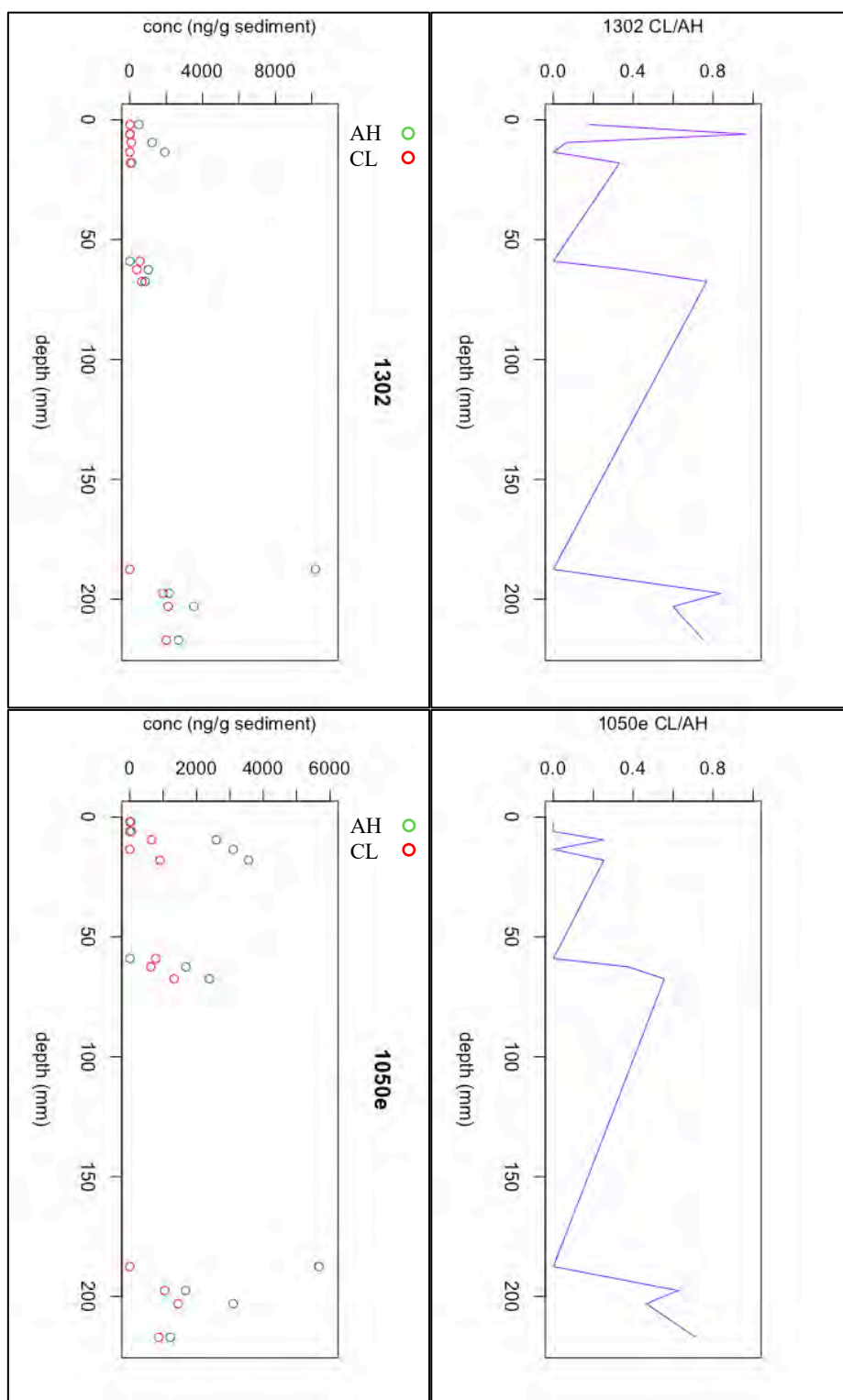


Figure 53, below: Concentration of AH (green) and CL (red) with depth and fraction CL/AH with depth for the four most abundant GDGT species.



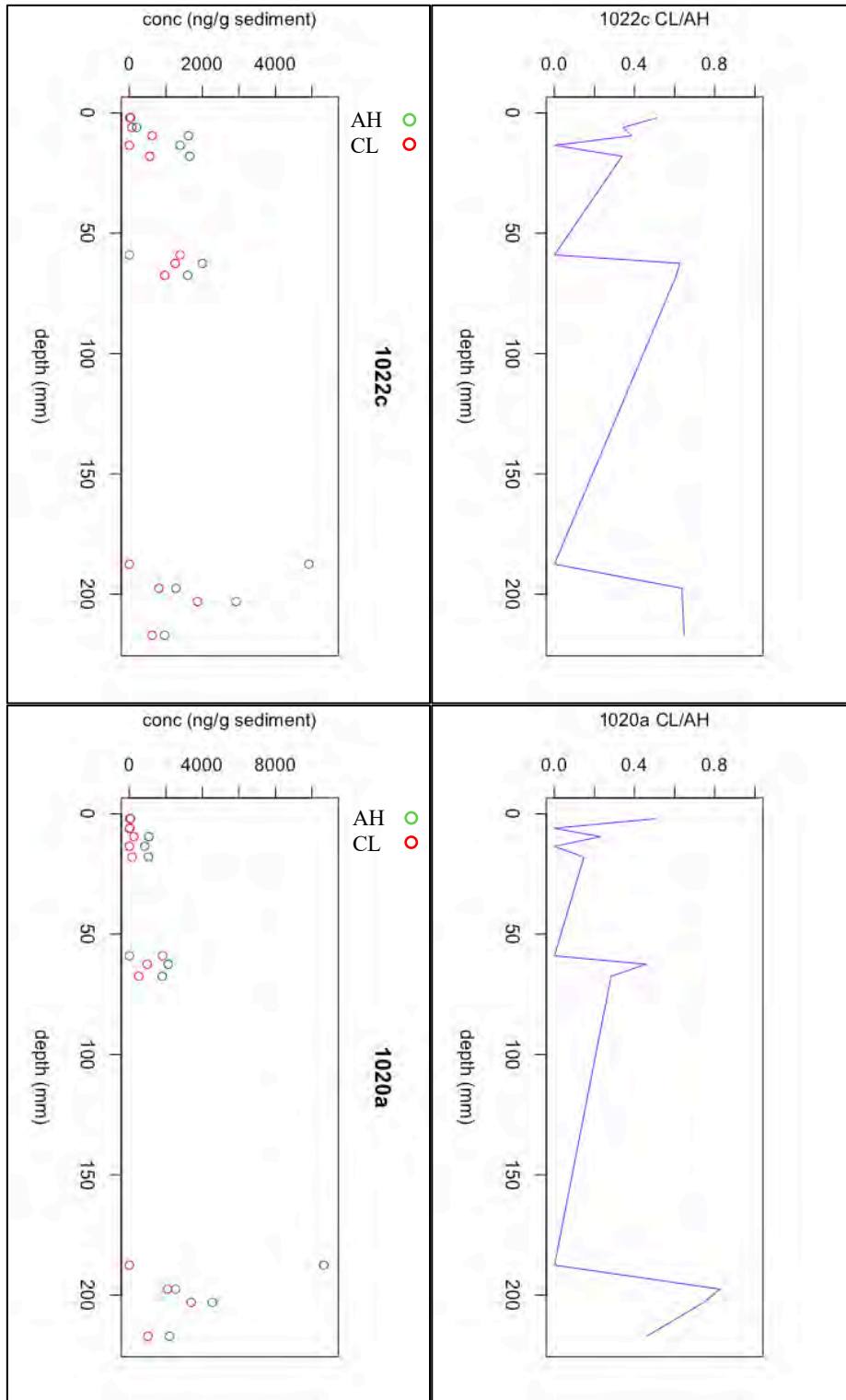


Table 12: Correlation matrix for average depth, elemental ITRAX data for Al, Si, Ar, Ca, Ti, V, Mn and GDGTs for core NP18B. Elements and GDGT species with only weak correlations (r between -0.59 and 0.59) are eliminated from the table. Weak correlations between the presented elements and GDGT species are shown in pale gray, moderate correlations in dark gray and good correlations in black.

	avg depth (mm)	Al	Si	Ar	Ca	Ti	V	Mn
avg depth (mm)	1,00	0,78	0,83	0,66	0,68	0,29	0,75	0,66
1302 AH	0,63	0,62	0,48	0,27	0,23	0,23	0,38	0,61
1050a AH	0,75	0,78	0,61	0,38	0,44	0,27	0,38	0,53
1050b AH	0,49	0,28	0,15	0,06	0,05	0,27	0,27	0,71
1050c AH	-0,11	0,02	-0,47	-0,60	-0,28	-0,15	-0,43	-0,07
1036b AH	0,69	0,53	0,36	0,33	0,32	0,27	0,38	0,71
1034d AH	0,79	0,70	0,56	0,43	0,41	0,28	0,46	0,70
1034g AH	0,80	0,64	0,53	0,38	0,33	0,39	0,56	0,79
1020a AH	0,65	0,64	0,46	0,27	0,26	0,32	0,38	0,64
1020b AH	0,72	0,66	0,48	0,32	0,31	0,24	0,40	0,68
1302 CL	0,81	0,55	0,65	0,60	0,66	0,11	0,62	0,41
1292r CL	0,43	0,10	0,18	0,18	0,10	0,66	0,47	0,43
1034c CL	0,16	-0,03	-0,04	0,01	-0,03	0,70	0,20	0,23
1034d CL	0,62	0,42	0,43	0,52	0,63	-0,13	0,33	0,36
1034g CL	0,75	0,42	0,47	0,48	0,50	0,20	0,58	0,54
1020a CL	0,61	0,42	0,50	0,58	0,72	-0,13	0,38	0,29
1020b CL	0,64	0,42	0,43	0,50	0,61	-0,11	0,38	0,40

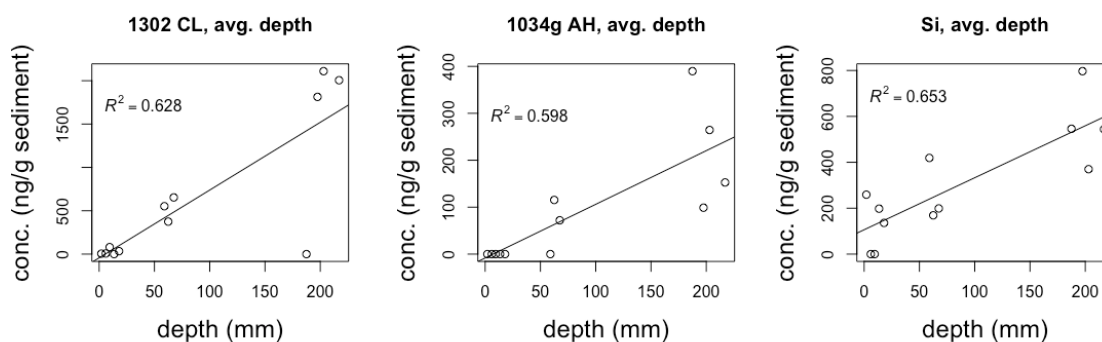


Figure 54: Significant correlation of 1302 CL (p-value: 0.00128), 1043g AH (p-value: 0.001928) and Si (p-value: 0.0008908) with depth.

Table 13: Correlation matrix for elemental ITRAX data for Cu, Zn, Ga, Br, Sr, Zr, Sb, Pb and GDGTs for core NP18B. Elements and GDGT species with only weak correlations (r between -59 and 59) are eliminated from the table. Weak correlations between the presented elements and GDGT species are shown in pale gray, moderate correlations in dark gray and good correlations in black.

	Cu	Zn	Ga	Br	Sr	Zr	Sb	Pb
avg depth (mm)	-0,64	0,76	-0,72	-0,72	0,58	-0,70	0,66	0,90
1302 AH	-0,25	0,76	-0,36	-0,33	0,17	-0,36	0,49	0,48
1296 AH	-0,13	0,67	-0,36	-0,20	0,12	-0,26	0,42	0,40
1292 AH	-0,10	0,66	-0,29	-0,18	0,07	-0,22	0,39	0,32
1292r AH	-0,14	0,69	-0,32	-0,22	0,10	-0,25	0,44	0,36
1050a AH	-0,39	0,73	-0,42	-0,43	0,35	-0,42	0,59	0,63
1046 AH	-0,16	0,69	-0,36	-0,24	0,15	-0,29	0,42	0,41
1036b AH	-0,32	0,75	-0,56	-0,38	0,16	-0,43	0,61	0,68
1034d AH	-0,41	0,85	-0,58	-0,48	0,29	-0,50	0,66	0,72
1034g AH	-0,34	0,83	-0,59	-0,44	0,22	-0,49	0,59	0,71
1020a AH	-0,25	0,76	-0,43	-0,32	0,17	-0,35	0,54	0,56
1020b AH	-0,32	0,80	-0,47	-0,39	0,19	-0,39	0,61	0,62
1018 AH	-0,17	0,69	-0,37	-0,25	0,15	-0,30	0,42	0,42
1302 CL	-0,62	0,41	-0,58	-0,66	0,56	-0,62	0,49	0,75
1292r CL	-0,02	0,14	-0,52	-0,09	0,06	-0,26	-0,04	0,48
1050a CL	-0,37	0,28	-0,64	-0,38	0,44	-0,49	0,29	0,68
1036b CL	-0,28	0,31	-0,49	-0,30	0,20	-0,34	0,40	0,60
1034d CL	-0,62	0,50	-0,53	-0,62	0,48	-0,56	0,69	0,68
1034g CL	-0,48	0,43	-0,59	-0,54	0,37	-0,55	0,46	0,72
1020a CL	-0,67	0,49	-0,60	-0,67	0,61	-0,62	0,71	0,72
1020b CL	-0,59	0,50	-0,54	-0,60	0,46	-0,55	0,65	0,68

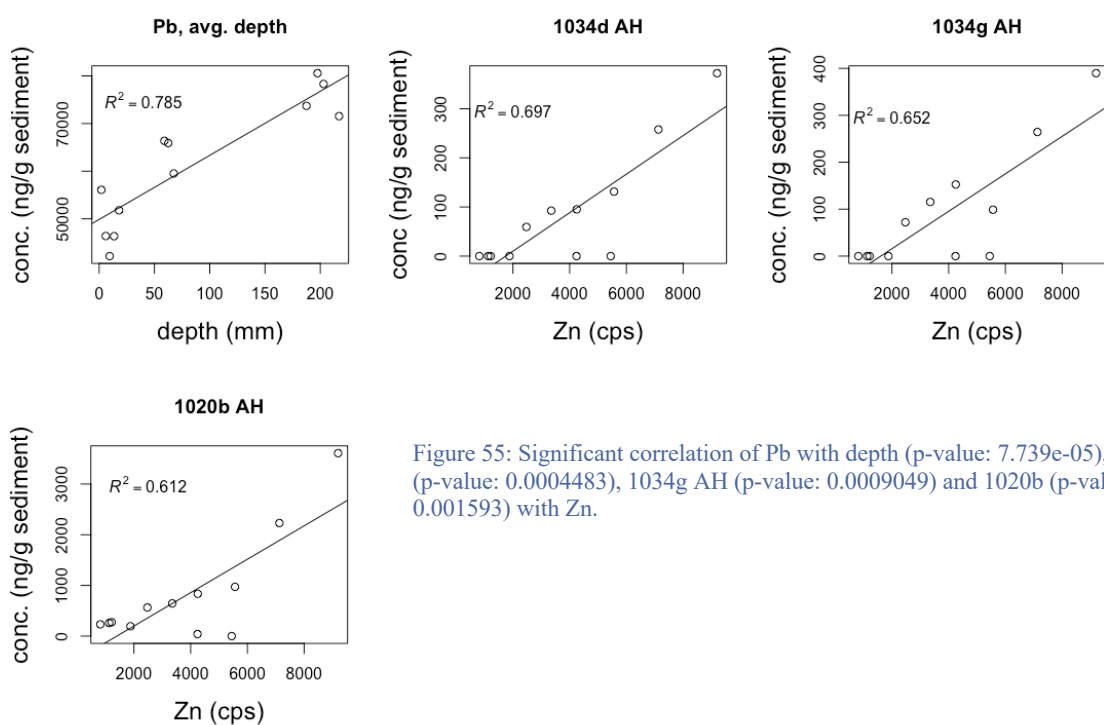


Figure 55: Significant correlation of Pb with depth (p-value: 7.739e-05), 1034d AH (p-value: 0.0004483), 1034g AH (p-value: 0.0009049) and 1020b (p-value: 0.001593) with Zn.

4.4 Surface water chemistry

Surface water samples from New Pond and from the main and south basin in Big Pond were analyzed for temperature, salinity and

pH in field and anions, cations and alkalinity at the Department of Geoscience, Stockholm University. The results are presented in table 14 together with Big Pond dry and wet season averages (Glunk et al., 2011).

Table 14: Surface water chemistry in Big Pond main basin, Big Pond south basin and New Pond, compared to seasonal averages in Big Pond by Glunk et al. (2011).

	Big Pond main, 2018	Big Pond south, 2018	New Pond, 2018	Big Pond main (Glunk et al., 2011)	
				Dry Season avg.	Wet season avg.
pH (field)	7,86	7,9	8,44	7,53	7,91
T (°C)	30,5	30,5	30,5	36	34
Salinity field (PSU)	154	170	84	209	132
NaCl * (per mille)	148,76	159,62	79,49		
pH (auto titr. initial)	8	7,93	8,26		
Alkalinity (auto titraton)	4,33	5,44	3,58		
Total alkalinity (mg as HCO ₃ ⁻)				614	769
Dil. factor (anions/cations)	1000	1000	500		
Al (mg/l)	2,81	2,17	0,85		
B (mg/l)	34,57	38,14	16,57		
Ba (mg/l)	0,40	0,24	0,16		
Be (mg/l)	0,17	0,16	0,08		
Ca (mg/l)	1342,30	1449,14	1101,12	1640	1200
Fe (mg/l)	2,26	2,36	0,96		
K (mg/l)	1797,58	2047,12	1006,89	2870	1460
Li (mg/l)	1,17	1,35	0,63		
Mg (mg/l)	5784,34	6581,61	2996,49	9580	5580
Mn (mg/l)	0,23	0,16	0,04		
Na (mg/l)	56876,80	64701,15	31260,23	84520	43850
S (mg/l)	5007,76	5628,26	2799,56		
Si (mg/l)	31,13	40,93	17,47		
Sr (mg/l)	43,57	49,91	21,93		
Ti (mg/l)	0,72	0,69	0,43		
Zn (mg/l)	3,45	1,86	0,59		
SO ₄ (mg/l)	11615,60	12887,03	6554,89	18530	9860
Cl (mg/l)	90242,04	96827,00	48218,29	150390	78020
Mg/Ca	4,31	4,54	2,72	5,8	4,65
SI _{calcite}				2	>1,5
SI _{gypsum}				>0,5	<0

*calculated from Cl

5. Discussion

5.1 Macroscopic diagenetic changes

The most apparent visual diagenetic effect is the change in organic content from the top of to the bottom of the sediment stack in both Big Pond and New Pond. In Big Pond the top 3,5 cm contain approximately 60% OM, 30% carbonate and 10% gypsum; to the bottom 3,5 cm which contain approximately 90% carbonate and 10% OM. In the top part of New Pond, the OM/(Ca,Mg)CO₃ relation is approximately 60/40 and the bottom part lack visible OM. The bottom part of New Pond core NP18 is sand, whereas the bottom part of Big Pond core display lamination. In New Pond, the thickness of microbial mat layer change with depth: above ca 16 cm depth mat thickness is around 1 mm while below this limit, they are <1mm. This change in mat thickness can be explained by compaction. This process is not as apparent in the New Pond core, where the mat thickness remains the same down to the lowest occurring mat at 22 cm. Even though the Big Pond OM seem compacted with depth, the carbonate is still very porous. This observation seems to indicate that this decreases in mat content might be more related to breakdown of organic material than actual compaction. The mineral grain and water within the sediment would in this case still be able to support the overlying sediment weight without pressing the minerals together. The lamination in Big Pond sediment is well defined, characterized by clear alternation of OM and precipitated carbonate in specific horizons, while the precipitates in the New Pond sediment is more evenly distributed within the organic material. This observation may explain the lower apparent compaction in New Pond mat compare to Big Pond. Indeed, the more evenly distributed carbonate precipitates still support the mat layer even though the OM gets degraded. There is no visible indication of secondary infilling of minerals such as sparry calcite in pore space between in situ

precipitates and other grains such as shell parts and there is no evidence of diagenetic recrystallization.

5.2 Precipitation styles

In Big Pond there is carbonate precipitation making up a micritic crust just below the active surface mat (Glunk et al., 2011; figure 56). This crust is made of not well crystallized carbonate, as seen in figure 17 in chapter 4.1.2. These crusts represent denser carbonate areas in thin section; while the less dense areas contain rod-shaped carbonate precipitation. The rods have a random orientation and distribution; and occur both dispersed and in small clusters.

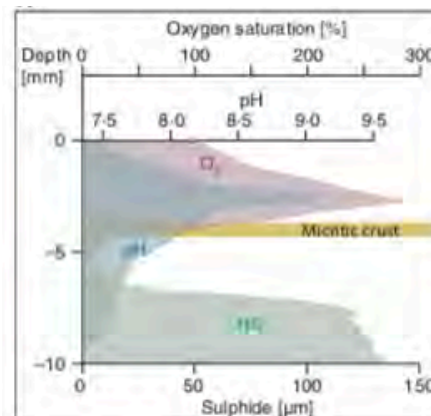


Figure 56: Oxygen, pH and sulphide in the upper 10 mm of the sediment in Big Pond (Glunk et al., 2011).

In New Pond there is no micritic crust, but very abundant carbonate rods and spherulites that randomly precipitate in the organic material. Already in the uppermost 0-4 mm, clusters of rods and spherulites are forming. Rods develop very early into various dumbbell-shapes. The only good examples of sharp carbonate rod shapes, which do not show any on-growth development, were observed in the first 0-4 mm (Fig. 67, Appendix B).

Although the two lakes are geographically very close to each other and present similar organosedimentary deposits, the evolution

of the sediment at depth looks different. In Big Pond, no important alteration of the initial precipitate (at the top of the mat) seems to occur during the burial process (very early diagenesis). No dissolution, recrystallization, or additional precipitation have been observed at depth. In New Pond, the initial precipitation seems to have been influenced by further clustering of the initial crystals and further outgrowths during burial. Why the early diagenesis seem different in between the two lakes is not easily explained with the data collected here. This difference might be related to the dynamic of the pore water that is different in between the two lakes (see below). It is however quite startling to see how much the original precipitation in Big Pond remains unchanged after more than 1000 years of slow burial by the successive microbial growth.

5.3 The role of microbial mats in early diagenesis of sediment in Big Pond and New Pond

The initial onset of carbonate precipitation within microbial mat often is characterized by amorphous calcium carbonate (ACC; Huang and Zhang, 2012). ACC can later transform into dumbbell, bouquet-shaped and spherical aragonite nanorod aggregates (ANA) in the presence of amino acid residues. The negatively-charged carboxyl groups in amino acid bind cations. In some cases, the geometry of the carboxyl-calcium complex can present similar feature as the aragonite lattice and can initiate the growth

of aragonite nanocrystals in ACC (Huang & Zhang, 2012). Fig. 57 illustrates different resulting morphologies from an organomineralization experiment by Huang & Zhang (2012) that is using as a nucleation template, a novel fibrous protein K58 from bivalve *Siliqua radiata* ligament. In the control, only calcite rhombs were formed, which indicate that amino acid residues may have a strong control on dumbbell and spherical growth of calcium carbonate.

The growth of rods and dumbbells in the New Pond core seems to show great similarity with the morphologies of the aragonite nanorod aggregates (ANA) as described by Huang & Zhang (2012). These features are not as obvious in the thin sections of core C7A (Big Pond); but the outlines of soft-edged rod-shaped calcite are visible. The presence of these features indicates that the organic material in the mats have strong influence on the precipitated carbonate morphology.

Table 15 presents wt % of different features determined by SEM-EDS analyses. Although Sr is very low in wt%, its presence corresponds to a lower Mg content in the mineral product compared to the mineral products where Sr show no presence. When it comes to Mg content, none is detected in analyzed shell clasts, whereas the initial precipitate within the organic matrix, not showing a clear crystalline texture (maybe ACC) have the highest Mg content.

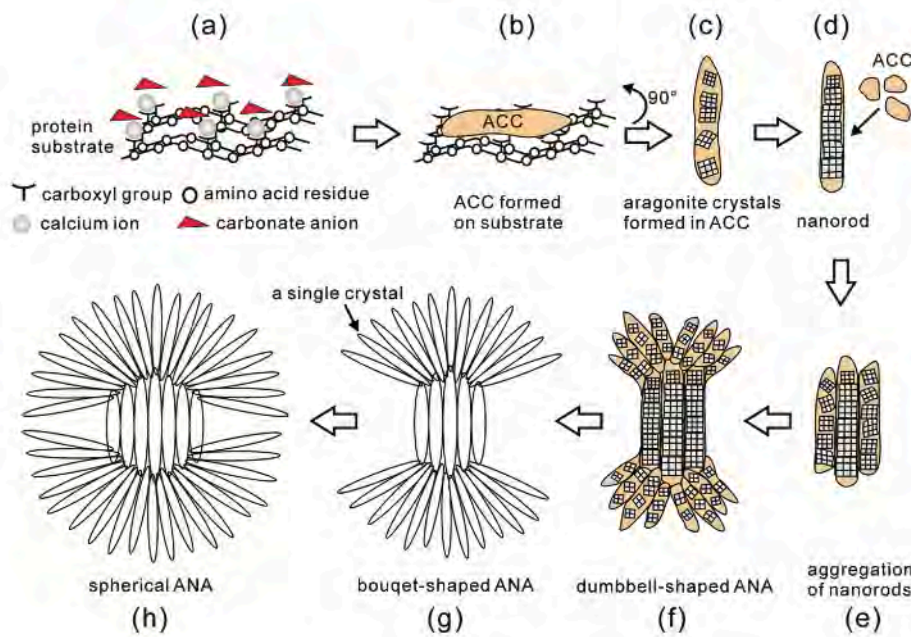


Figure 57: The possible formation process of aragonite rod aggregates (ANA) from amorphous calcium carbonate (ACC): (a) Ca^{2+} attach to carboxyl groups and gets chelated (b) The short-range order of carboxyl groups resemble aragonite crystal lattice create ACC with short-range order resembling aragonite crystals (c) ACC is transformed to nanocrystals of aragonite with random orientation; (d) the nanocrystals rotate to the same orientation as they grow and a single nanorod is formed; (e) ACCs attaches to the nanorod and transform into new nanorods; (f–h) further attachment of ACC, growing and fusing of nanocrystals, and aggregating, results in a gradual evolution of dumbbell-shaped into spherical morphologies (Huang & Zhang, 2012).

Table 15: Comparing different carbonate features. Normalized wt% where Au is subtracted. Mg content in analysed rods and spherulites in New Pond range between 3 and 8 wt% while in Big Pond amorphous calcium carbonate have 14,29 and rod cluster 11,61wt Mg. Shell parts have no Mg content. Sr is very low, 1wt% was used before normalization where detected.

Site	Fig.	Feature	Spectr.	Ca (wt%)	O (wt%)	Mg (wt%)	S (wt%)	Other (wt%)	Tot.
New Pond	41	spherulite	28	52,63	37,89	7,37	2,11		100
New Pond	35	rod	56	61,70	32,98	3,19	2,13		100
New Pond	33	spherulite	40	58,89	34,44	4,44	2,22		100
New Pond	29	rod	51	53,26	41,30	3,26	2,17		100
New Pond	27	rod	45	58,62	33,33	3,45	2,30	Si 2,30	100
New Pond	24	spherulite	42	56,10	37,80	3,66	2,44		100
New Pond	32	Spherulite cluster	54	71,13	25,77	1,03	1,03	Sr 1,03	100
New Pond	32	Spherulite cluster	55	55,79	37,89	3,16	2,11	Sr 1,05	100
New Pond	23	shell part	39	89,13	10,87	0,00	0,00		100
Big Pond	16	amorphous	6	47,45	36,73	14,29	1,02	Na 0,51	100
Big Pond	7	rod cluster	7	53,55	33,55	11,61	1,29		100

5.4 GDGTs

The top 4 mm contains the lowest concentration of GDGTs of < 100 ng/g freeze-dried sediment, but this goes up substantially with depth (Fig. 52). The most abundant GDGTs are the archaeal isoprenoid GDGT-0 (m/z 1302) and the branched GDGTs 1050e, 1022c and 1020a. The very low relative abundance of cyclized GDGTs (m/z 1018, 1032 and 1046) is congruent with earlier observations of low abundance in high pH and alkaline environments (Weijers et al., 2009, Schoon et al., 2013). An attempt to calculate alkalinity and pH from the distribution of GDGTs according to Schoon et al. (2013) ended up on the high, insensitive end of the calibration curve, i.e. >13 meq and pH >13 for all samples of both lakes. A more detailed analysis is needed to find out if other GDGT ratios would be sensitive to alkalinity changes at higher levels. However, since there was no analysis made on porewater from New Pond sediment, a direct comparison of DIC and measured total alkalinity of the lake surface water (including organic compounds) cannot be done for New Pond. Instead, other analyses need to be performed on samples from the lake sampling campaign, covering nearly 40 lakes with a wide range of salinity and alkalinity.

The correlations between the various GDGTs need further investigation before making any interpretations. The most common covariant is depth. The increase with depth of many GDGTs may be related to a relative enrichment of these lipid compounds, by selective removal of EPS. One obvious parameter that is lacking in the analysis is the Total Organic Carbon content, although visual and microscopic analysis indicates that the TOC content decreases with depth. The correlation with the heavy metals Zn, Mn and Pb might be coincidental, although both the organic and organic depth profiles could be caused by diagenesis.

5.5 Lake water chemistry vs recharge

There is a decreasing salinity from the south to the north end of Big Pond (Glunk et al. (2011), which indicates an inflow of ocean water in the northern part (Fig. 58). This is coinciding with the presence of the lowest part of the ridge (6-12 m high) at this point that shield Big Pond from the Atlantic Ocean, allowing waves to flow in more frequently. The lake is in addition fed by seawater seepage through the porous Pleistocene rock. Freshwater seepage (from freshwater lense) is also very frequent attested by abundant outflow spots close to the site 1a. Eleuthera has a measured thickness of freshwater lens/island width ratio of 0,39 % (Moore & Wade, 2013a). The island is between 1 500 and 2 000 m wide where Big Pond is located, which means that the fresh water lens is theoretically 6-8 m thick below Big Pond. By looking at elevation profiles (Google Earth), Big Pond seem to be at 2 m above sea level. These elevation profiles are not to be considered as entirely reliable since the lake area is relatively small and the profiles are not precisely detailed. If this assessment is correct, it suggests that it is less likely to have ocean water seepage through the Pleistocene because the flow should rather run in direction of the Ocean. However, the lake is hypersaline and gypsum is precipitating in the Southern part of the lake, which clearly indicates a recharge from the open ocean compensating the evaporation. An increasing salinity trend from <50 ppt in near ocean and lagoon shore lakes toward >125 ppt in inland lakes of equatorial Pacific Ocean atoll island of Kiritimati indicates that isolation from the ocean as one potential cause of extreme salinities (Saenger et al., 2006). There is a possibility that the underground connection with the ocean could have been filled up with sediment during early development of the lake or that this happened in the south part of the lake but not in the north. However, the N-S gradient of salinity indicates that refill by ocean water seem to

occur mainly from the north; from waves and/or seepage. A varying freshwater supply from rainfall (both direct in the lake and indirect via seasonal variation in groundwater supply) could explain the big difference in salinity between dry and wet season. Especially compared to New Pond which is located very nearby; if both lakes have frequent exchange with the ocean and evaporation alone would be the cause for the change in salinity; they would be expected to have more similar salinity the same time of year. Since Big Pond had twice the salinity of New Pond at the time of fieldwork for this study, it is probable that the two lakes at least to some degree have different water sources. No previous investigations of New Pond are available to compare seasonal variations.

The fresh water seepage indicates that there is a local gravity driven freshwater lens in the area west of Big Pond which have conduits releasing water at the bottom surface at site 1a. A map of the available drainage area approximated from elevation profiles (Google Earth, 2018c) show that the area west of site 1a is the widest part of the drainage area (Fig. 59). Since the underground flow of water is determined by how the very variable porosity in the Pleistocene carbonate rock is connected, it is difficult to estimate the size of this local freshwater supply. With phreatic cave development in mind, there could be a cave system in the nearby ridges that continuously feed Big Pond and keep the lake water level fairly constant during wet season. The Mg^{2+}/Ca^{2+} ratio in the bottom water of Big Pond is around 6. This is higher than the ocean shore water on south Eleuthera (Mg^{2+}/Ca^{2+} 3,1 2015) and agree

with refilling by diagenetically altered water through the dissolution of Mg-calcite. The ratio of Mg^{2+}/Ca^{2+} is 3,1 in ocean shore water on south Eleuthera and 0,39 in river water (Emerson & Hedges, 2008).

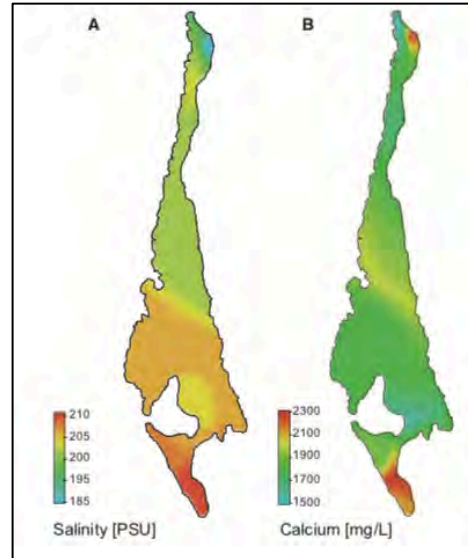


Figure 58: Distribution of salinity (A) and calcium (B) in Big Pond (Glunk et al., 2011)



Figure 59 Potential drainage basin for Big Pond, measured from elevation curves in Google Earth (2018-11-23).

5.6 Porewater and ITRAX

Fe correlates well with Ti in the ITRAX element data in both Big Pond and New Pond. The only way for these elements to end up in Bahamas is by wind since there are no other rocks than carbonates close. Dust carried by winds from Sahara to the Caribbean are connected to African drought (Itambi et al., 2009). A comparison of Ti ITRAX data from core C7A and drought event records in western Africa reveal possible correlations (Touchan et al., 2011), (Fig. 60).

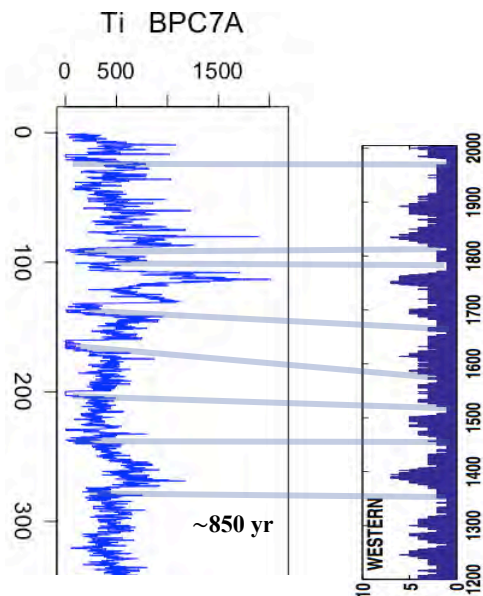


Figure 60: ITRAX Ti data compared to western Africa drought events year 1200-2000 (Touchan et al., 2011) and possible correlations between low Ti and low drought event frequency. Note that the values have opposite directions, making the peaks mirror

In the case of Cu, there was a decrease with depth and a significant positive correlation with Br ($r = 0,91$), in New Pond, and moderate correlation ($r=0,73$) in Big Pond. Br that is bound in organic complexes also form bonds with metals (Sforna et al., 2017). As organic matter gets degraded, Br is released and leached, decreasing the Br content in the core (Sforna et al., 2017). Substitution of Ca^{2+} by other cations is common in carbonate precipitation (Sforna et al., 2017). Sr show moderate correlation

with Ca in this study, $r = 0,65$ in Big Pond and $r=0,7$ in New Pond, but in the comparison between the graphs of Sr and Ca there are several coinciding peaks in both cores. Sr^{2+} have a larger ionic radius than Ca^{2+} and is therefore preferably incorporated in aragonite, in which Ca^{2+} have a coordination number of 9, while it is 6 in calcite (Sunagawa et al., 2007). Mg^{2+} is smaller than Ca^{2+} in ionic radius and cannot form 9 coordination but is easily incorporated in calcite (Sunagawa et al., 2007).

The distribution of elements in porewater has a different pattern in core C3 (2015) and B2 (2018). As an example, Sr in B2 does not vary much from top water (48 mg/l at 5 cm above sediment surface) to the bottom of the core (38 mg/l at 51 cm depth). In contrast, Sr in C3 varies from 48 mg/l at 0 cm to almost 80 mg/l a few cm below. It then drops back to similar values as the B2 curve at 10 cm and lower than B2 at the bottom of C3. All measured porewater values show this peak in the C3 core. This evolution could be explained by recent heavy rainfall before the C3 measurement. The water was turbid at the time of the C3 core sampling and clear at the time of B2 core sampling. Glunk et al., (2011) reported an increase in turbidity of the water after heavy rainfall. This would be in agreement with groundwater seepage refill of the lake, where pressure from below would flush up mobile elements and results in lower bottom values and a peak higher up. The uppermost top porewater is equilibrated with the lake water, giving equal values towards the top of the core. The Sr content in the elemental ITRAX data from core C7A (that was retrieved at the same time as C3) show a stronger variation at the level of the Sr porewater peak, and follow a fairly stable value below 10 cm.

In the porewater results, the Ca from core C3 is significantly higher than in B2, while the pattern of Sr and Mg starts lower. C3 Mg/Ca is mirroring the other values above the core C7A peak of Sr, while the values

follow each other fairly well below the Sr peak. Although the three cores are different in depth, they are retrieved within a small area of the lake, so their patterns of elements in sediment and porewater should be comparable. Assuming that B2 represents how the sediment profile look when the porewater is in balance with the lake water, a possible mechanism behind the C3 patterns could be that rainfall brings groundwater from below that is enriched in Ca and shows lower Sr and Mg values

compare to lake water. Sr-bearing aragonite and Mg-bearing calcite start to dissolve at depth. When the porewater reaches a Mg and Sr concentration that is higher than the carbonate in the core, these elements starts to re-precipitate and may be replacing Ca since the Ca peak comes a little bit above as highlighted by the bar at 15 cm depth in Figure 61. At around 7 cm depth, the Sr in the core is again higher and not in equilibrium with the pore water and Sr- and Mg-bearing carbonate continue dissolving.

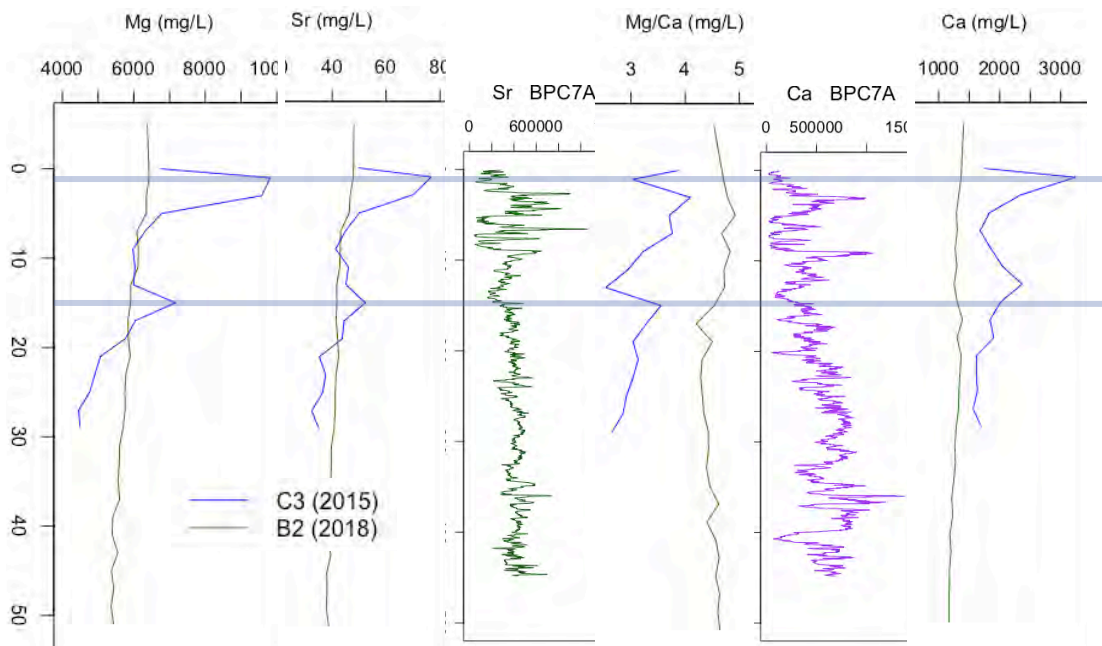


Figure 61: Mg, Sr, Mg/Ca and Ca pore water values from core C3 (2015) in blue and core B2 (2018) in green, and ITRAX Sr and Ca from core C7A (2015).

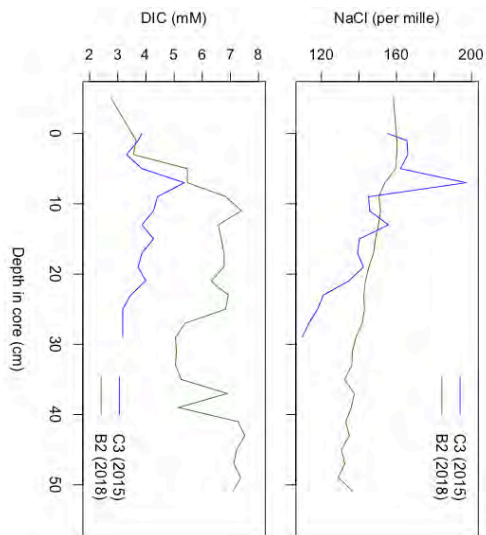


Figure 62: DIC and NaCl (calculated from Cl) in porewater from core C3 (2015) in blue and core B2 (2018) in green.

Note that the DIC in C3 is below the B2 values up until just below the sediment surface (Fig. 62). The DIC in equilibrium with the core in high pH do not dissolve carbonate, while fresh rainwater has lower pH will promote dissolution.

Just below the sediment surface, porewater Ca, Mg, and Sr values dip steep back to similar values as B2, indicating either that they quickly precipitate or equilibrate with the lake water at this depth. Knowing that the high Mg calcite crust forms at this depth, the former alternative seems to be what is happening. Porewater NaCl (calculated from Cl) in C3 is too high at the bottom to fit with freshwater input. However, this value is lower than the B2 porewater, which could be in agreement with inmix of freshwater diluting the porewater that is in equilibrium with the core/lake water.

5.7 The role of lake chemistry for precipitation

Table 16 presents the major ion content, DIC and Mg/Ca ratio of Big Pond seepage, bottom and surface water, New Pond surface water and Eleuthera ocean shore. River water is presented for comparison.

Big Pond bottom water has the overall highest concentrations of all except DIC. As evident from the pore water profiles, DIC is very high in the porewater, explaining the high DIC in seepage water. All New Pond values are lower than Big Pond and closer to ocean shore values. The Mg/Ca ratio is still higher than the ocean ratio, which suggests some input of high Mg groundwater, but the ocean/groundwater refill ratio is probably higher than for Big Pond. The different lake chemistries give different prerequisites for precipitation in the two lakes. The seasonal fluctuations in Big Pond give an SI for gypsum that is below supersaturation during wet season and the recharge from below seem to dissolve part of what have precipitated, leaving a porous sediment. New Pond seasonal variations are not known, though the presence of gypsum throughout the core depth and the growth of bigger rods/clusters with depth suggest a more stable porewater chemistry. There are overall more correlations of different elements in the New Pond ITRAX data than in Big Pond which could be a result of a more stable environment of sedimentation. Physical properties of the extracellular organic material in the mats affect the precipitation of carbonate by confining in situ CaCO_3 to the area below the mat surface. Despite CaCO_3 saturation in the lake water there is no precipitation in the mat-bottom water interface in Big Pond.

Though most Sr/Ca values is lower than any available values in the Sr/Ca- *Porites* paleothermometer (de Villiers et al., 1994, Fig.66), and that thermometer is based on coralline aragonite, one could consider higher Sr/Ca values as lower temperature episodes. The mean temperature on Bahamas has been rising the last 150 years (Fig.65), which coincides with a decrease in the Sr/Ca ration from the New Pond mat down to a depth of 5 cm (Fig. 64). This Sr/Ca decrease do not occur in the Big Pond top sediment, where there is a decrease from 10 to 1 cm but then a sudden increase in the

top 1 cm. Even though the New Pond Core is not dated and the depths vs ages might not correspond, the signal from the uppermost part in the two lakes at least would be expected to show a similar pattern if the air temperature vs surface temperature would be the key for change since the two lakes are very close to each other. Ti/Ca on the other hand coincides fairly well with the Sr/Ca pattern in each lake. Comparing to the time

series of hurricanes in the Caribbean by Caviedes (1991), there is an increase in hurricanes the last 250 years compared to the preceding 250 years (Fig.63). An increase in drastic weather events could give a relative decrease in porewater temperature, so that the Sr/Ca values could be used as a record of temperature in core at time of precipitation rather than surface water temperatures.

Table 16: Comparative table of concentrations of major ions in ocean water, river water, Big Pond bottom water (2015), Big Pond main, south and New Pond surface water (this study), seepage water (2015) and ocean water on Eleuthera south shore (2015). The bottom water value is the one decimal rounded mean value of top water (TW) from cores C1A, C3A and C5A and the surface and Bahamas ocean shore water values are the one decimal rounded mean of two samples each. *from Emerson & Hedges (2008).

Constituent	Na ⁺	Mg ²⁺	Ca ²⁺	K ⁺	Cl ⁻	SO ₄ ²⁻	DIC	Mg/Ca
River water* (mmol kg ⁻¹)	0,23	0,13	0,33	0,04	0,22	0,12	0,96	0,39
BP bottom (mmol l ⁻¹)	2973,30	287,20	45,80	56,00	2841,50	141,40	3,30	6,30
BP seepage (mmol l ⁻¹)	2197,10	214,50	43,40	43,10	2002,50	96,00	6,10	4,90
BP main surface (mmol l ⁻¹)	2472,90	237,94	33,49	45,97	2545,61	120,91		7,10
BP south surface (mmol l ⁻¹)	2813,09	270,74	36,16	52,36	2731,37	134,14		7,49
NP surface (mmol l ⁻¹)	1359,14	123,26	27,47	25,75	1360,18	68,23		4,48
Ocean shore (mmol l ⁻¹)	685,90	71,50	23,10	16,40	803,00	33,70	2,80	3,10

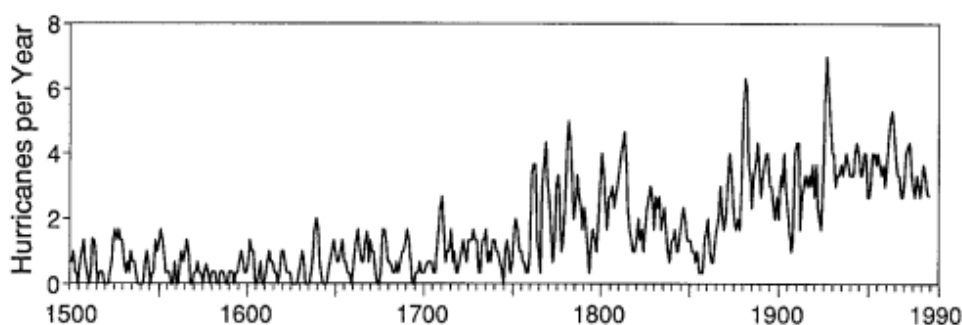


Figure 63: Time series of hurricanes in the Caribbean 1500-1990 (Caviedes, 1991).

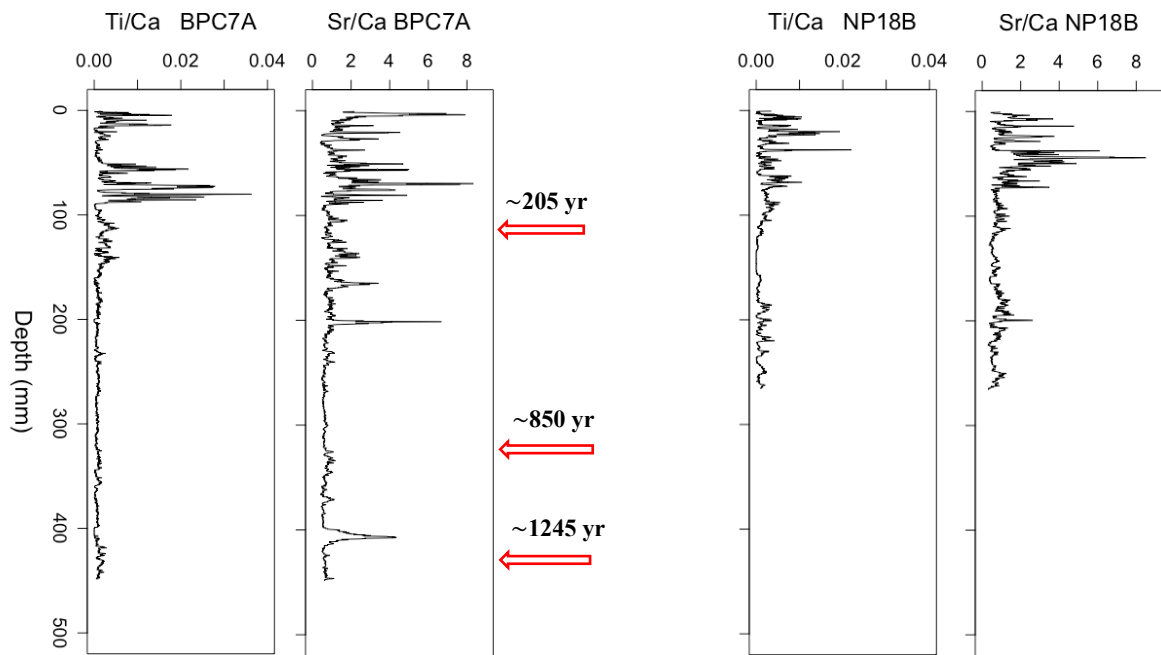


Figure 64: ITRAX Ti/Ca ratios for core C7A and NP18B. Carbon date ages for C7A is marked out.

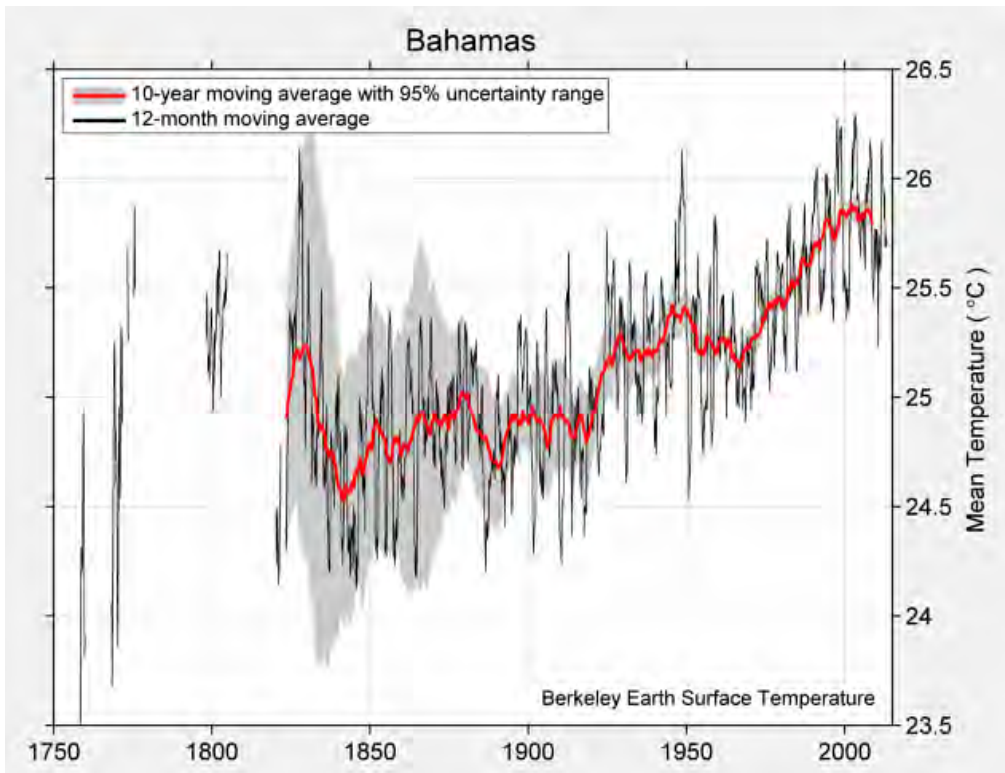


Figure 65: Mean temperature record on the Bahamas 1750 -present day. BerkeleyEarth (2019)

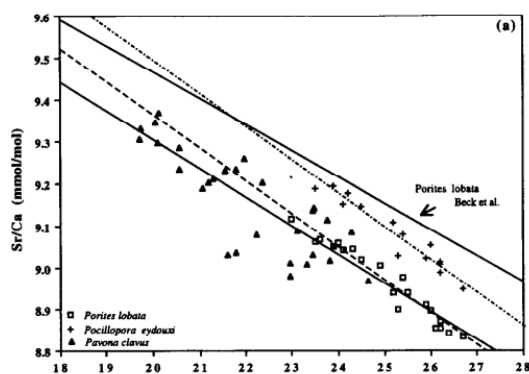


Figure 66: *Porites* paleothermometer (de Villiers et al., 1994).

6. Conclusions

One visually detectable diagenetic change present along the organosediment cores is that the organic material content decrease with depth. Both lakes have microbial mats that gives the prerequisites for in situ carbonate precipitation, rod- and spherulite formation. The morphologies and distribution of carbonate precipitates are affected by the organic material in the microbial mats. The microbial mats in Big Pond produce thin carbonate crusts a few mm under the sediment surface, rods are distributed in thicker but more porous layers and there are distinct layers with only organic material. In New Pond there are no crusts, but more even distribution of rods and spherulites within the organic material. The decrease of organic material with depth passively compacts the sediment. The more even distribution of rods, spherulites and clusters in New Pond let the old mat horizon keep the same thickness as at the top of the sediment, while in Big Pond the old mat horizons thin with depth due to lack of mineral support. There is similar porosity in the carbonate fraction at the top and bottom of the sediment in Big Pond while there is a trend towards denser carbonate cluster assembling downcore in New Pond. In general, this study seems to indicate that although the two lakes are geographically very close to each other and present similar

organosedimentary deposits, the evolution of the sediment at depth is relatively different. In Big Pond, no important alteration of the initial precipitate (at the top of the mat) seems to occur during the burial process (very early diagenesis). No dissolution, recrystallization, or additional precipitation have been observed at depth. In New Pond, the initial precipitation seems to have been influenced by further clustering of the initial crystals and further outgrowths during burial. The reason why the style of early diagenesis is different in between these lakes are not fully understood and will be the subject of further study. One possible explanation for differences in water chemistry and precipitation style, despite close proximity of the two lakes, could be different recharge ratio of ocean vs fresh water in the two lakes.

The lake water chemistry in Big Pond and New Pond differ, suggesting a different ratio of ocean/groundwater recharge for the two lakes. Porewater fluctuations with season in Big Pond indicate that porewater is mobile in the sediment and the relatively flat porewater profiles in core B2 suggests that pore water equilibrate with lake water. The difference in lake water chemistry give different prerequisites for precipitation in the sediment. SI for gypsum is below supersaturation during wet season in Big Pond and above during dry season, giving a situation of precipitation and dissolution periodically.

The recharge from ground water seepage in Big Pond might dissolve any precipitated gypsum and some of the carbonate at depth, while there are gypsum crystals occurring throughout the depth of the core in New Pond. There are overall more correlations of elements in the New Pond ITRAX data than in Big Pond, which could be a consequence of less seasonal fluctuations and/or less bottom seepage in New Pond than in Big Pond.

GDTDs were detected downcore in New Pond, a positive initial result for a large lake survey made for a proxy development pilot project with the aim to investigate to what extent the relative distribution of brGDGTs is related to alkalinity, pH, and possibly salinity, and might be useful in the interpretation of the sedimentary sequences. Approximately 40 lakes on Eleuthera Island and San Salvador were included in the survey. The lake survey results are not a part of this thesis.

Acknowledgements

Christophe Dupraz, Rienk Smittenberg, Susanne Sjöberg, Klara Hajnal, Malin Kylander, Carina Johansson, Carl-Magnus Mörth, Pär Hjelmquist, Petter Hällberg, Alasdair Skelton, Elin Tollefsen, Draupnir Einarsson, Krister Junghahn, Magnus Ivarsson, Therese Sallstedt, Iain Pitcairn, Volker Brüchert, Otto Hermelin, Arne Lif, Elisabeth Däcker, my fellow master students, my boyfriend Patrik Wall, my family and friends.

Funding of the 2018 Bahamas fieldtrip and GDGT analysis:
Bolin Center for Climate Research.

References

- Arp, G., Reimer, A., & Reitner, J. (2001). Photosynthesis-induced biofilm calcification and calcium concentrations in Phanerozoic oceans. *Science*, 292(5522), 1701-1704.
- BerkeleyEarth (2019) <http://berkeleyearth.lbl.gov/regions/bahamas> accessed 2019-04-30
- Bligh, E. G., & Dyer, W. J. (1959). A rapid method of total lipid extraction and purification. *Canadian journal of biochemistry and physiology*, 37(8), 911-917.
- Braissant, O., Decho, A. W., Dupraz, C., Glunk, C., Przekop, K. M., & Visscher, P. T. (2007). Exopolymeric substances of sulfate-reducing bacteria: interactions with calcium at alkaline pH and implication for formation of carbonate minerals. *Geobiology*, 5(4), 401-411.
- Caviedes, C. N. (1991). Five hundred years of hurricanes in the Caribbean: their relationship with global climatic variabilities. *GeoJournal*, 23(4), 301-310.
- Croudace, I. W., & Rothwell, R. G. (Eds.). (2015). *Micro-XRF Studies of Sediment Cores: Applications of a non-destructive tool for the environmental sciences* (Vol. 17). Springer.
- Damsté, J. S. S., Hopmans, E. C., Pancost, R. D., Schouten, S., & Geenevasen, J. A. (2000). Newly discovered non-isoprenoid glycerol dialkyl glycerol tetraether lipids in sediments. *Chemical Communications*, (17), 1683-1684.
- De Jonge, C., Hopmans, E. C., Zell, C. I., Kim, J. H., Schouten, S., & Damsté, J. S. S. (2014). Occurrence and abundance of 6-methyl branched glycerol dialkyl glycerol tetraethers in soils: Implications for palaeoclimate reconstruction. *Geochimica et Cosmochimica Acta*, 141, 97-112.
- de Villiers, S., Shen, G. T., & Nelson, B. K. (1994). The SrCa-temperature relationship in coralline aragonite: Influence of variability in (SrCa) seawater and skeletal growth parameters. *Geochimica et Cosmochimica Acta*, 58(1), 197-208.
- Dupraz, C., Reid, R. P., Braissant, O., Decho, A. W., Norman, R. S., & Visscher, P. T. (2009). Processes of carbonate precipitation in modern microbial mats. *Earth-Science Reviews*, 96(3), 141-162.
- Dupraz, C., Reid, R. P., & Visscher, P. T. (2011). Microbialites, modern. In *Encyclopedia of geobiology* (pp. 617-635). Springer, Dordrecht.
- Emerson, S., & Hedges, J. (2008). *Chemical oceanography and the marine carbon cycle*. Cambridge University Press. P.38-39, 77-80
- Gallagher, K. L., Kading, T. J., Braissant, O., Dupraz, C., & Visscher, P. T. (2012). Inside the alkalinity engine: the role of electron donors in the organomineralization potential of sulfate-reducing bacteria. *Geobiology*, 10(6), 518-530.
- Glunk, C., Dupraz, C., Braissant, O., Gallhager, K.L., Verrecchia, E.P., & Visscher, P.T. (2011). Microbially mediated carbonate precipitation in a hypersaline lake, Big Pond (Eleuthera, Bahamas). *Sedimentology*, (2011) 58, 720–738
- Google Earth, images retrieved 2018-10-10 (2018a), 2018-11-21 (2018b), 2018-11-23 (2018c), 2019-01-08 (2019a), 2019-01-15 (2019b), 2019-01-16 (2019c)
- Huang, Z., & Zhang, G. (2012). Biomimetic synthesis of aragonite nanorod aggregates with unusual morphologies using a novel template of natural fibrous proteins at ambient condition. *Crystal Growth & Design*, 12(4), 1816-1822.

- Ingalls, A. E., Huguet, C., & Truxal, L. T. (2012). Distribution of intact and core membrane lipids of archaeal glycerol dialkyl glycerol tetraethers among size-fractionated particulate organic matter in Hood Canal, Puget Sound. *Applied and environmental microbiology*, 78(5), 1480-1490.
- Itambi, A. C., Von Dobeneck, T., Mulitza, S., Bickert, T., & Heslop, D. (2009). Millennial-scale northwest African droughts related to Heinrich events and Dansgaard-Oeschger cycles: Evidence in marine sediments from offshore Senegal. *Paleoceanography and Paleoclimatology*, 24(1).
- James, L. C. (1997). Geology of the Bahamas. *Geology and hydrogeology of carbonate islands*, 54, 91.
- Kindler, P., & Hearty, P. J. (1996). Carbonate petrography as an indicator of climate and sea-level changes: new data from Bahamian Quaternary units. *Sedimentology*, 43(2), 381-399.
- Kindler, P., & Hearty, P. J. (1997). Geology of the Bahamas: architecture of Bahamian Islands. *Geology and Hydrogeology of Carbonate Islands, Developments in Sedimentology*, 54, 141-160.
- Loomis, S. E., Russell, J. M., Verschuren, D., Morrill, C., De Cort, G., Damsté, J. S. S., ... & Kelly, M. A. (2017). The tropical lapse rate steepened during the Last Glacial Maximum. *Science advances*, 3(1), e1600815.
- McHugh CMG, Gurung D, Giosan L, Ryan WBF, Mart Y, Sancar U, Burckle L, Cagatay MN (2008) The last reconnection of the Marmara Sea (Turkey) to the World Ocean: A paleoceanographic and paleoclimatic perspective. *Mar Geol* 255:64–82. doi:10.1016/j.margeo.2008.07.005
- Miller, G. R., & Kester, D. R. (1976). Sodium fluoride ion-pairs in seawater. *Marine Chemistry*, 4(1), 67-82.
- Milne, G. A., Long, A. J., & Bassett, S. E. (2005). Modelling Holocene relative sea-level observations from the Caribbean and South America. *Quaternary Science Reviews*, 24(10-11), 1183-1202.
- Moore, C. H., & Wade, W. J. (2013). Meteoric Diagenetic Environment. In *Developments in Sedimentology* (Vol. 67, pp. 165-206). Elsevier.
- Mylroie, J. E., & Carew, J. L. (1995). Geology and karst geomorphology of San Salvador Island, Bahamas. *Carbonates and Evaporites*, 10(2), 193-206.
- Naafs, B. D. A., Inglis, G. N., Zheng, Y., Amesbury, M. J., Biester, H., Bindler, R., Blewett, J., Burrows, M.A., del Castillo Torres, D., Chambers, F.M., Cohen, A.D., Evershed, R.P., Feakins, S.J., Gałka, M., Gallego-Sala, A., Gandois, L., Gray, D.M., Hatcher, P.G., Honorio Coronado, E.N., Hughes, P.D.M, Huguet, A., Könönen, M., Laggoun-Défarge, F., Lähenteoia, O., Lamentowicz, M., Marchant, R., McClymont, E., Pontevedra-Pombal, X., Ponton, C., Pourmand, A., Rizzuti, A.M., Rochefort, L., Schellekens, J., De Vleeschouwer, F., Pancost, R.D. (2017). Introducing global peat-specific temperature and pH calibrations based on brGDGT bacterial lipids. *Geochimica et Cosmochimica Acta*, 208, 285-301.
- Noffke, N., Christian, D., Wacey, D., Hazen, R.M., 2013, Microbially Induced Sedimentary Structures Recording an Ancient Ecosystem in the ca. 3.48 Billion-Year-Old Dresser Formation, Pilbara, Western Australia, *Astrobiology*, volume 13, number 12, doi:10.1089/ast.2013.1030
- Pitcher, A., Hopmans, E. C., Schouten, S., & Damsté, J. S. S. (2009). Separation of core and intact polar archaeal tetraether lipids using silica columns: insights into living and fossil biomass contributions. *Organic Geochemistry*, 40(1), 12-19.
- Russell, J. M., Hopmans, E. C., Loomis, S. E., Liang, J., & Damsté, J. S. S. (2018). Distributions of 5- and 6-methyl branched glycerol dialkyl glycerol tetraethers (brGDGTs) in East African lake sediment:

- Effects of temperature, pH, and new lacustrine paleotemperature calibrations. *Organic Geochemistry*, 117, 56-69.
- Saenger, C., Miller, M., Smittenberg, R. H., & Sachs, J. P. (2006). A physico-chemical survey of inland lakes and saline ponds: Christmas Island (Kiritimati) and Washington (Teraina) Islands, Republic of Kiribati. *Saline Systems*, 2(1), 8.
- Schoon, P. L., de Kluijver, A., Middelburg, J. J., Downing, J. A., Damsté, J. S. S., & Schouten, S. (2013). Influence of lake water pH and alkalinity on the distribution of core and intact polar branched glycerol dialkyl glycerol tetraethers (GDGTs) in lakes. *Organic geochemistry*, 60, 72-82.
- Schopf, J. W., Kitajima, K., Spicuzza, M. J., Kudryavtsev, A. B., & Valley, J. W. (2018). SIMS analyses of the oldest known assemblage of microfossils document their taxon-correlated carbon isotope compositions. *Proceedings of the National Academy of Sciences*, 115(1), 53-58.
- Schouten, S., Hopmans, E. C., Schefuß, E., & Damsté, J. S. S. (2002). Distributional variations in marine crenarchaeotal membrane lipids: a new tool for reconstructing ancient sea water temperatures?. *Earth and Planetary Science Letters*, 204(1-2), 265-274.
- Schouten, S., Hopmans, E. C., & Damsté, J. S. S. (2013). The organic geochemistry of glycerol dialkyl glycerol tetraether lipids: a review. *Organic geochemistry*, 54, 19-61.
- Sforna, M. C., Daye, M., Philippot, P., Somogyi, A., Van Zuilen, M. A., Medjoubi, K., Gérard, E., Jamme, F., Dupraz, C., Braissant, O., Glunk, C. & Visscher, P.T. (2017). Patterns of metal distribution in hypersaline microbialites during early diagenesis: implications for the fossil record. *Geobiology*, 15(2), 259-279.
- Sunagawa, I., Takahashi, Y., & Imai, H. (2007). Strontium and aragonite-calcite precipitation. *Journal of Mineralogical and Petrological Sciences*, 102(3), 174-181.
- Tierney, J. E., Russell, J. M., Huang, Y., Damsté, J. S. S., Hopmans, E. C., & Cohen, A. S. (2008). Northern hemisphere controls on tropical southeast African climate during the past 60,000 years. *Science*, 322(5899), 252-255.
- Tierney, J. E., & Russell, J. M. (2009). Distributions of branched GDGTs in a tropical lake system: implications for lacustrine application of the MBT/CBT paleoproxy. *Organic Geochemistry*, 40(9), 1032-1036.
- Touchan, R., Anchukaitis, K. J., Meko, D. M., Sabir, M., Attalah, S., & Aloui, A. (2011). Spatiotemporal drought variability in northwestern Africa over the last nine centuries. *Climate Dynamics*, 37(1-2), 237-252.
- Warren, J. K. (2016). *Evaporites – A geological compendium*, second edition, Springer International Publishing Switzerland, ISBN 978-3-319-13512-0 (eBook), doi 10.1007/978-3-319-13512-0,
- Whitaker, F. F., & Smart, P. L. (1997). Hydrogeology of the Bahamian archipelago. *Geology and hydrogeology of carbonate islands: Amsterdam, Elsevier*, 183-216.
- Visscher, P. T., & Stolz, J. F. (2005). Microbial mats as bioreactors: populations, processes, and products. In *Geobiology: Objectives, Concepts, Perspectives* (pp. 87-100).
- Weber, Y., Sinninghe Damsté, J. S., Hopmans, E. C., Lehmann, M. F., & Niemann, H. (2017). Incomplete recovery of intact polar glycerol dialkyl glycerol tetraethers from lacustrine suspended biomass. *Limnology and Oceanography: Methods*, 15(9), 782-793.

Weijers, J. W., Schouten, S., van den Donker, J. C., Hopmans, E. C., & Damsté, J. S. S. (2007). Environmental controls on bacterial tetraether membrane lipid distribution in soils. *Geochimica et Cosmochimica Acta*, 71(3), 703-713.

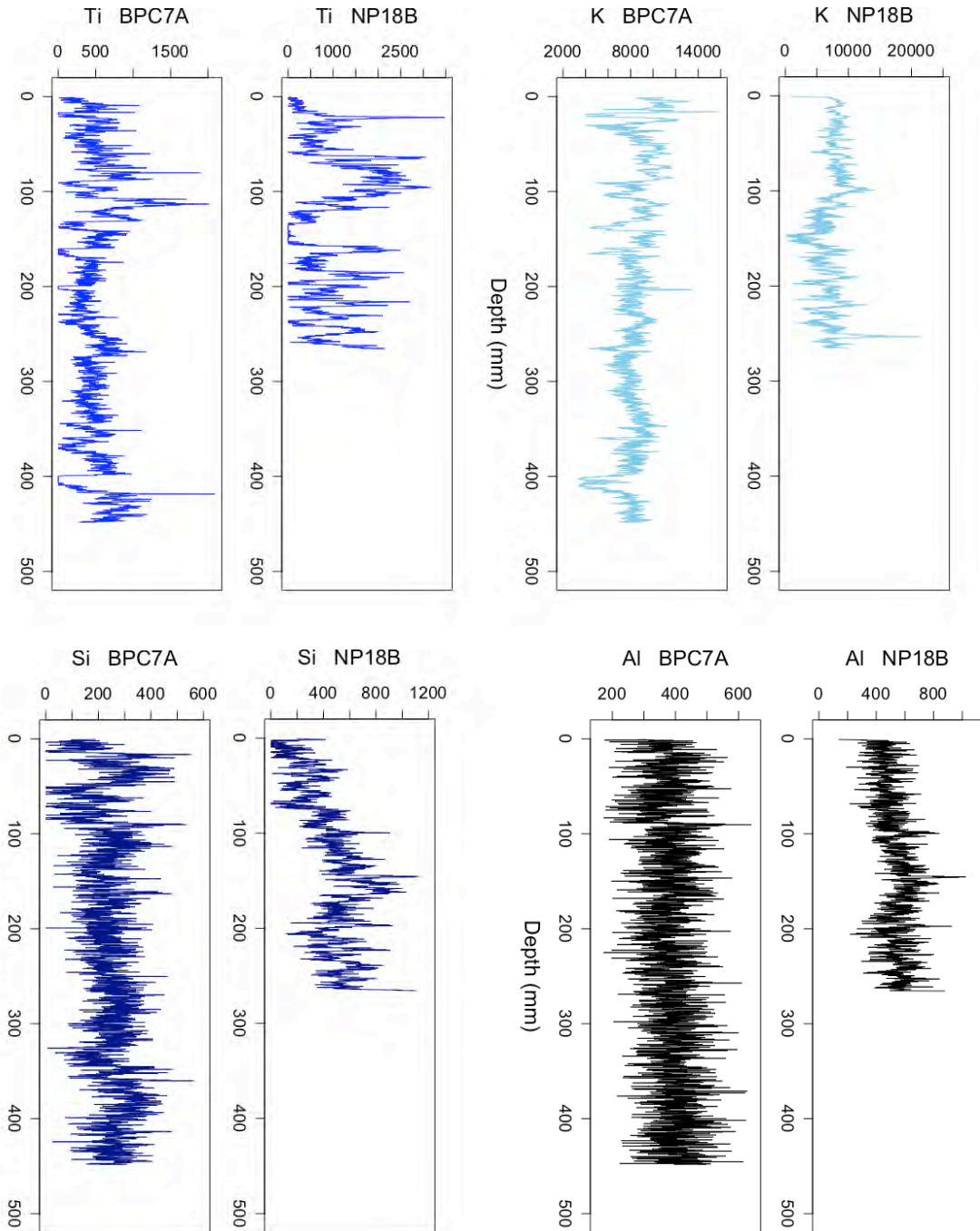
Weijers J. W. H., Panoto E., van Bleijswijk J., Schouten S., Rijpstra W. I. C., Balk M. and Stams A. J. M., et al. (2009) Constraints on the biological source(s) of the orphan branched tetraether membrane lipids. *Geomicrobiol. J.* 26(6), 402–414.

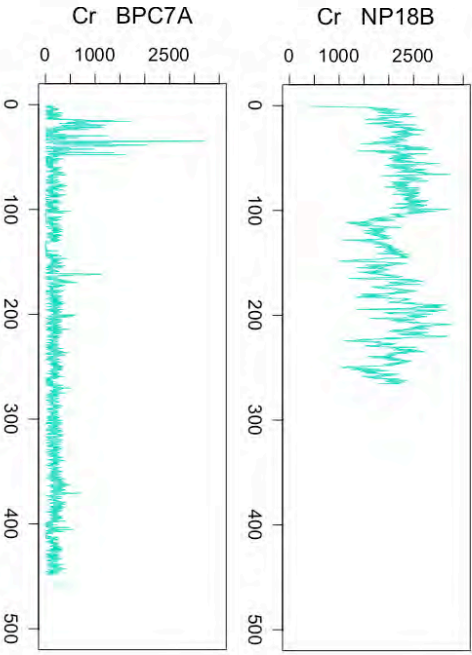
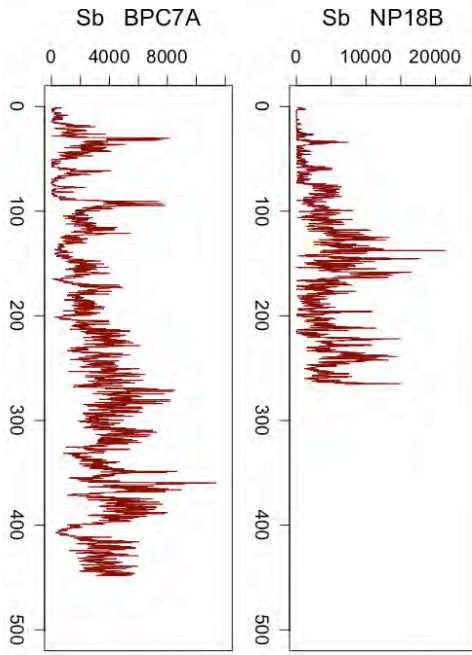
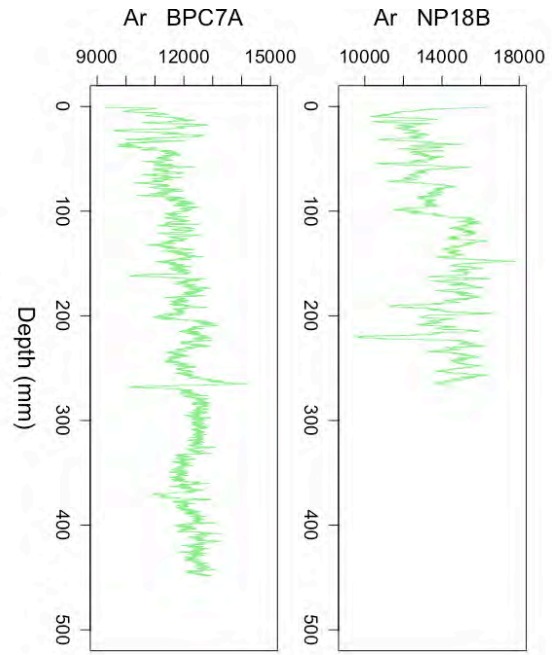
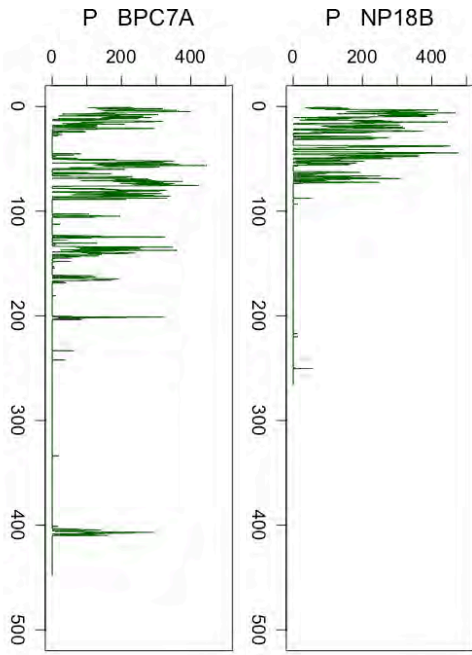
Wolkersdorfer, C. (2008). *Water management at abandoned flooded underground mines: fundamentals, tracer tests, modelling, water treatment*. Springer Science & Business Media.

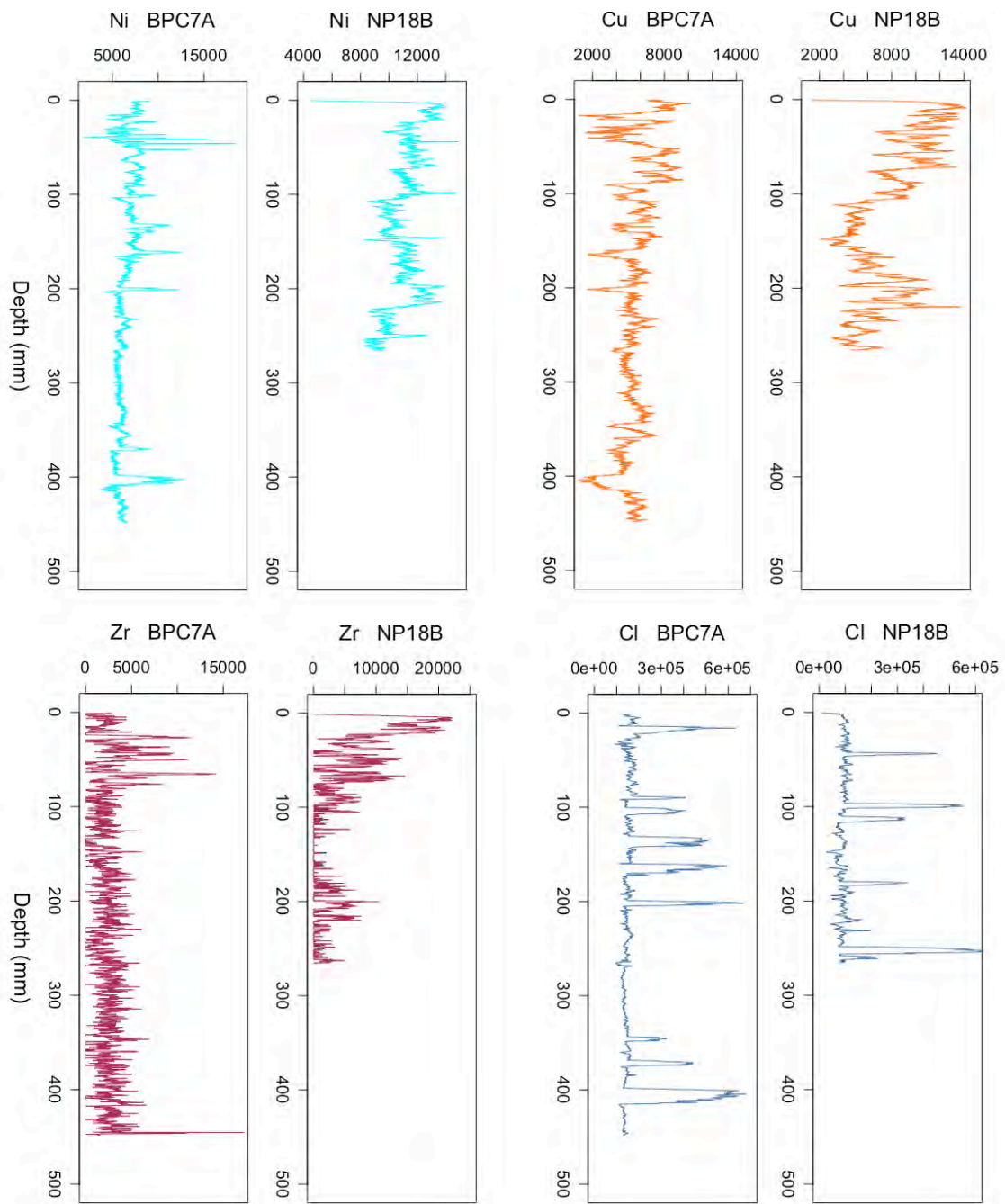
Xu J, Holbourn A, Kuhnt W, Jian Z, Kawamura H (2008) Changes in the thermocline structure of the Indonesian outflow during Terminations I and II. *Earth Planet Sci Lett* 273:152–162

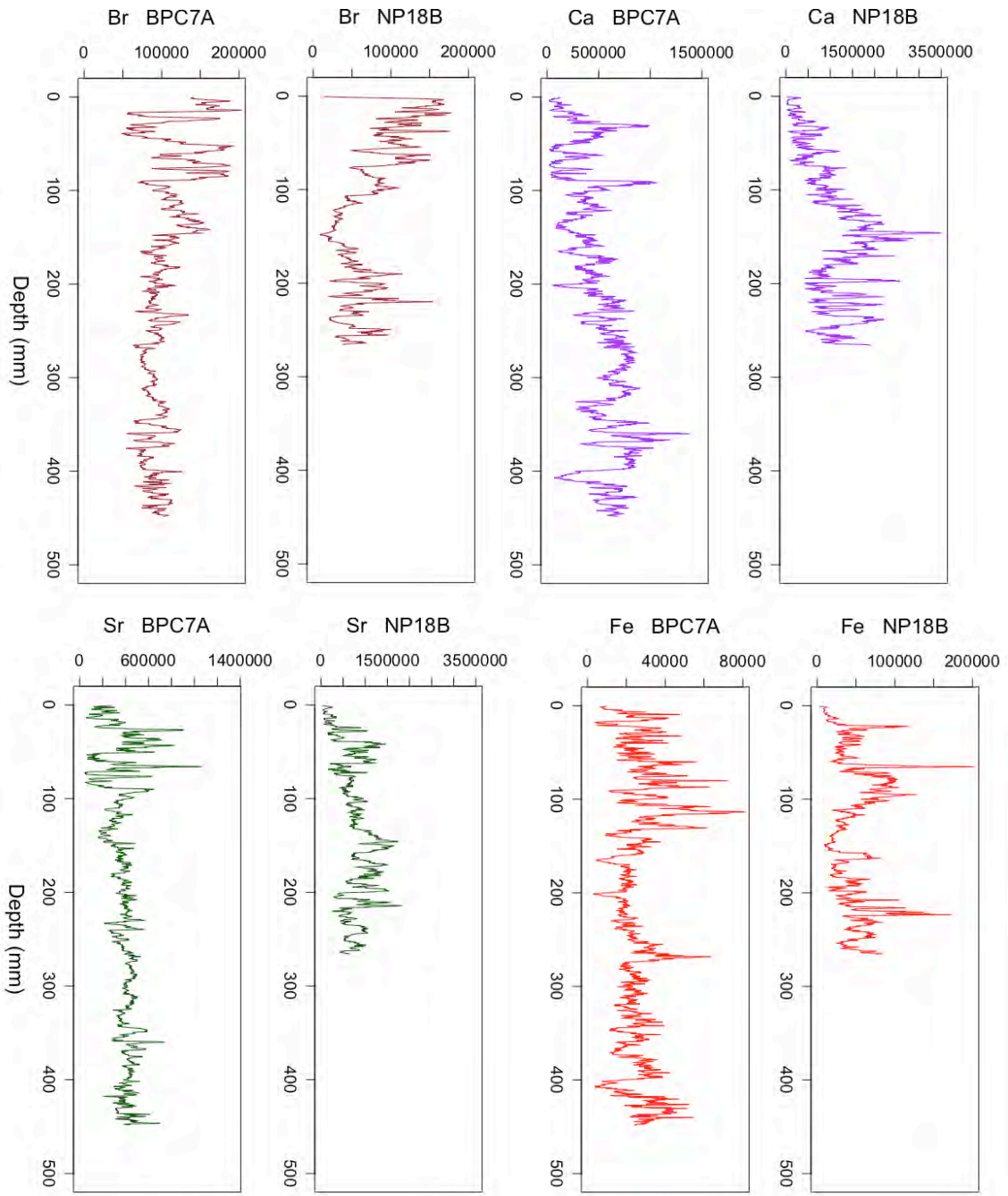
Yannarell, A. C., Steppe, T. F., & Paerl, H. W. (2007). Disturbance and recovery of microbial community structure and function following Hurricane Frances. *Environmental microbiology*, 9(3), 576-583.

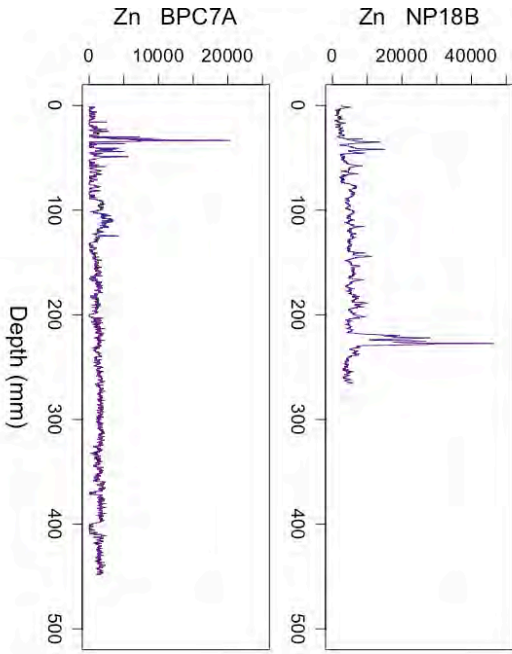
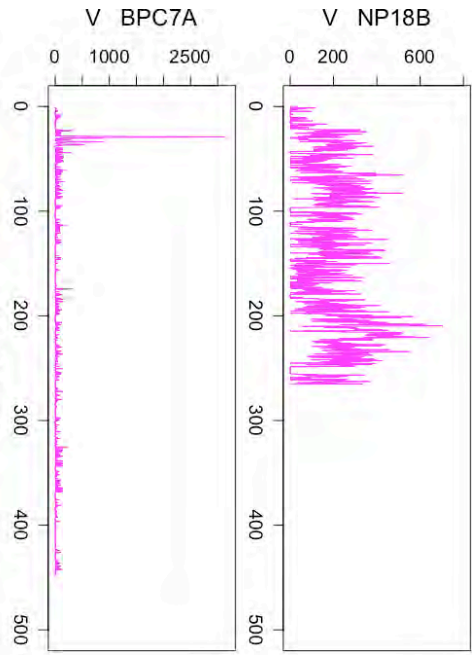
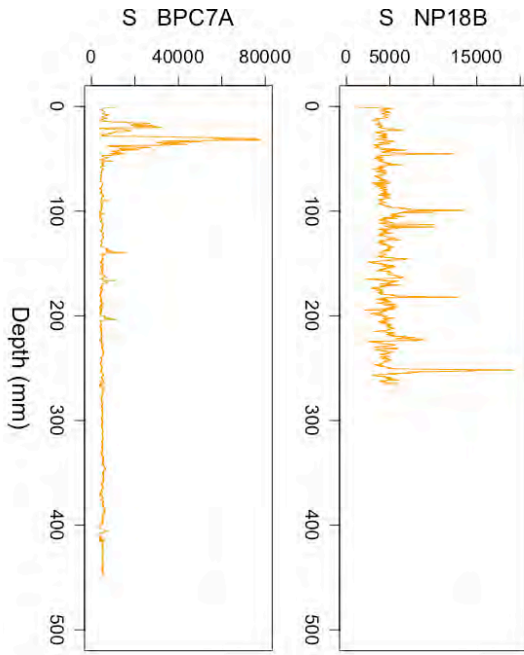
Elemental ITRAX data from Big Pond (BPC7A) and New Pond (NP18B)

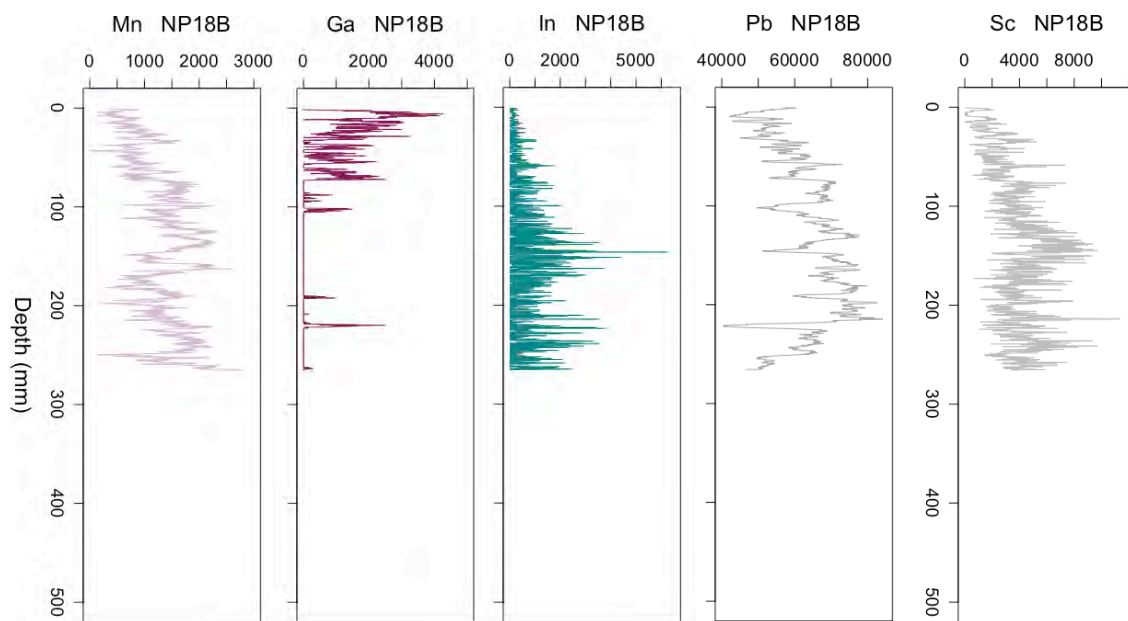












Complementary backscatter electron images from core NP18A

Figure 67, below: Backscatter electron images of sample S1. All cloth- and threadlike grey material is organic matter. A) Carbonate rods, size of rod in middle $\sim 3 \mu\text{m}$. B) Carbonate rods with rounded ends, size of rods in middle $\sim 10 \mu\text{m}$. C) Cluster of carbonate spherulites, size of single spherulites $\sim 6 \mu\text{m}$.

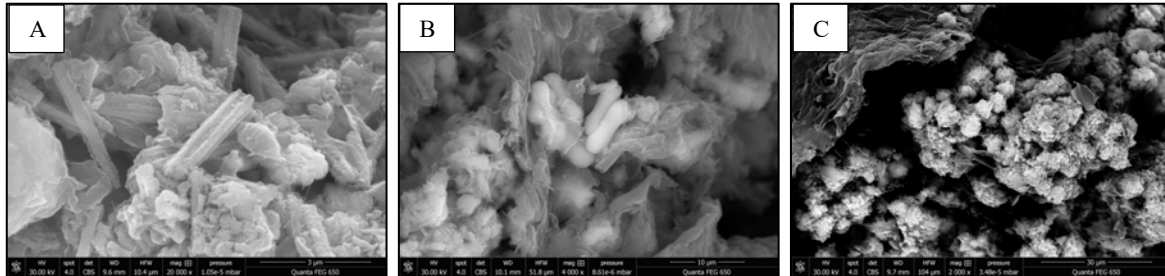


Figure 68, below: Backscatter electron images from sample S2. A) Cluster of carbonate spherulites, size of cluster $\sim 120 \mu\text{m}$. B) Close-up on spherulites from 32A), size of spherulites $\sim 5 - 10 \mu\text{m}$. C) Close-up on spherulite from 32B), size of triangular edges $< 1 \mu\text{m}$. D) Irregular multi-cluster of dumbbell-shaped carbonate, size of multi-cluster $\sim 350 \mu\text{m}$. E) Close-up on dumbbells from 32D), size of dumbbells $\sim 1 - 25 \mu\text{m}$. F) Dumbbell with perpendicular out growth, size $\sim 15 \mu\text{m}$.

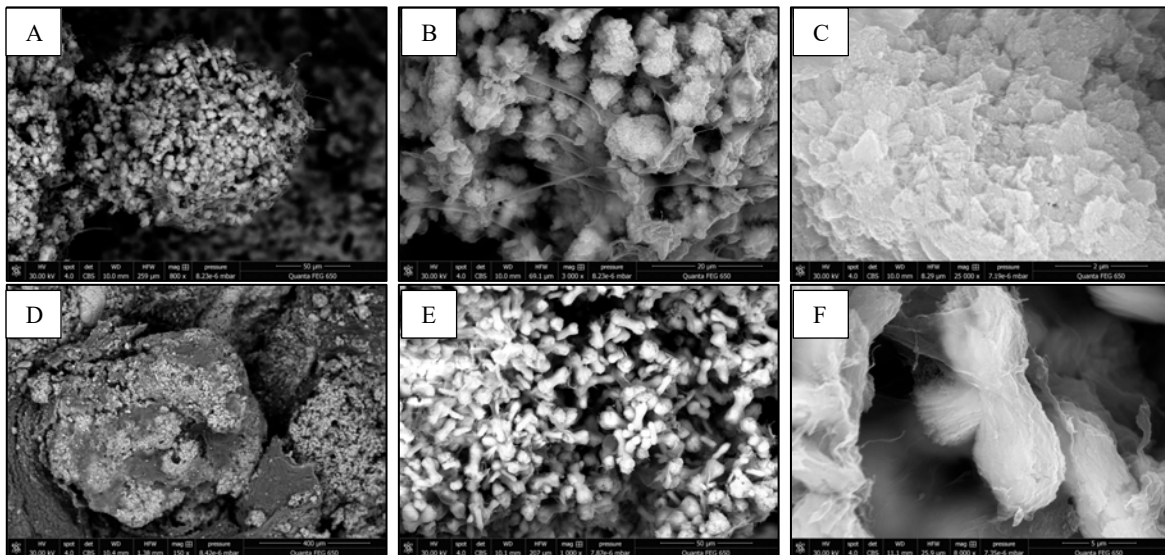


Figure 69, below: Backscatter electron images from sample S3. A) Needle gypsum cross bundles, size $\sim 35 \mu\text{m}$. B) Needle gypsum bundle, size $\sim 40 \mu\text{m}$. C) Carbonate rods/dumbbells, unevenly dispersed on organic material. D) Close-up on dumbbells from 33B), size of dumbbell in lower right corner $\sim 20 \mu\text{m}$. E) Dumbbells, some with multiple outgrowths. F) Close-up of outgrowth with triangular endings (image distorted by charge in SEM). G) Area with high density of dumbbells, and some needle gypsum bundles. H)

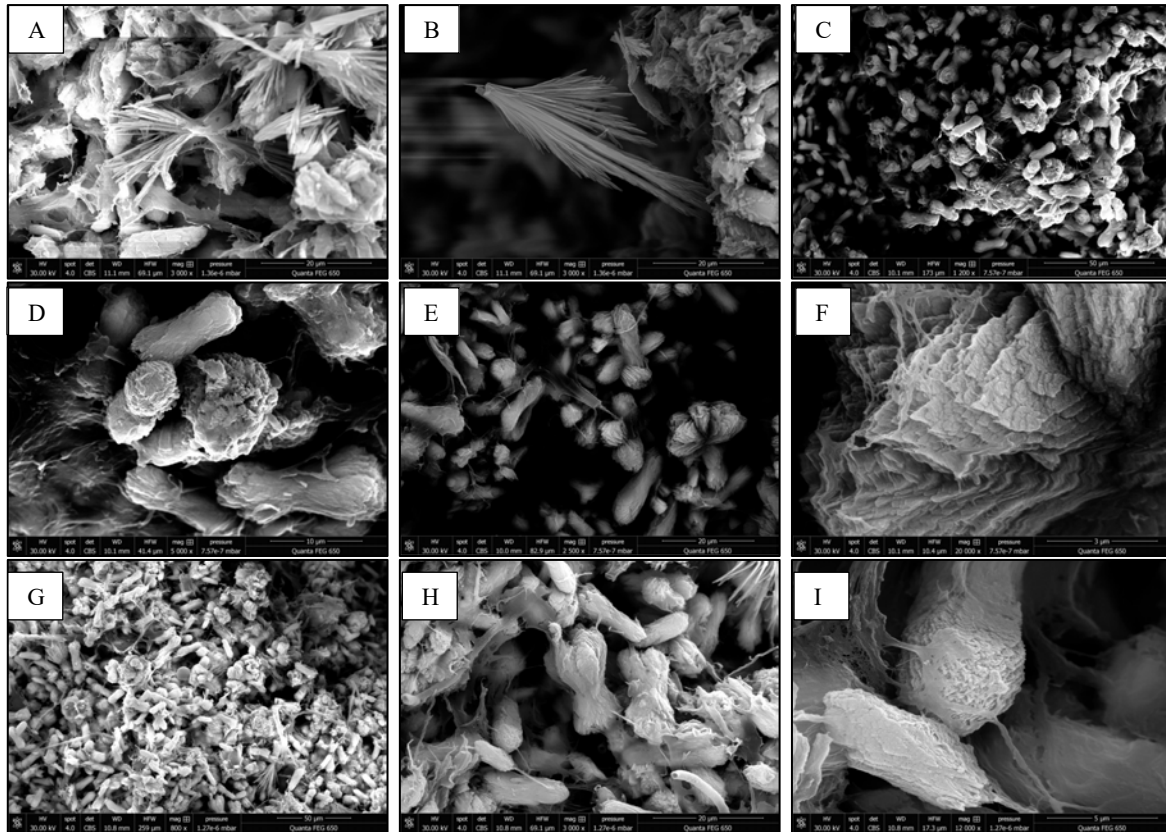


Figure 70, below: Backscatter electron images from sample S4. A) Precipitates randomly distributed in organic material. B) Rounded carbonate grains encapsulated in OM. C) Close-up on carbonate grains with rim of OM, diameter of encapsulated grain in middle $\sim 2,5 \mu\text{m}$.

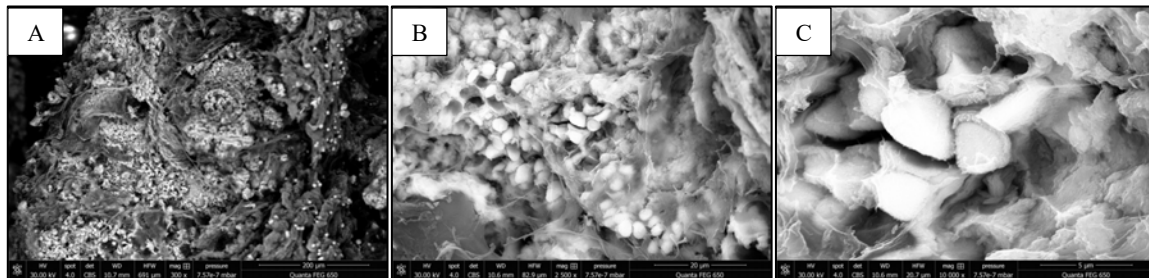


Figure 71, below: Backscatter electron images from sample S5. A) Framboidal pyrite sphere, size of sphere $\sim 4 \mu\text{m}$. B) Organic material with empty holes. C) Close-up of holes, diameter of holes $\sim 2 - 5 \mu\text{m}$. D) Four individual dumbbell/rods that have attached to each other. E) Close-up of the four rods, size of each rod $\sim 15 \mu\text{m}$. F) Close-up on attachment of rods.

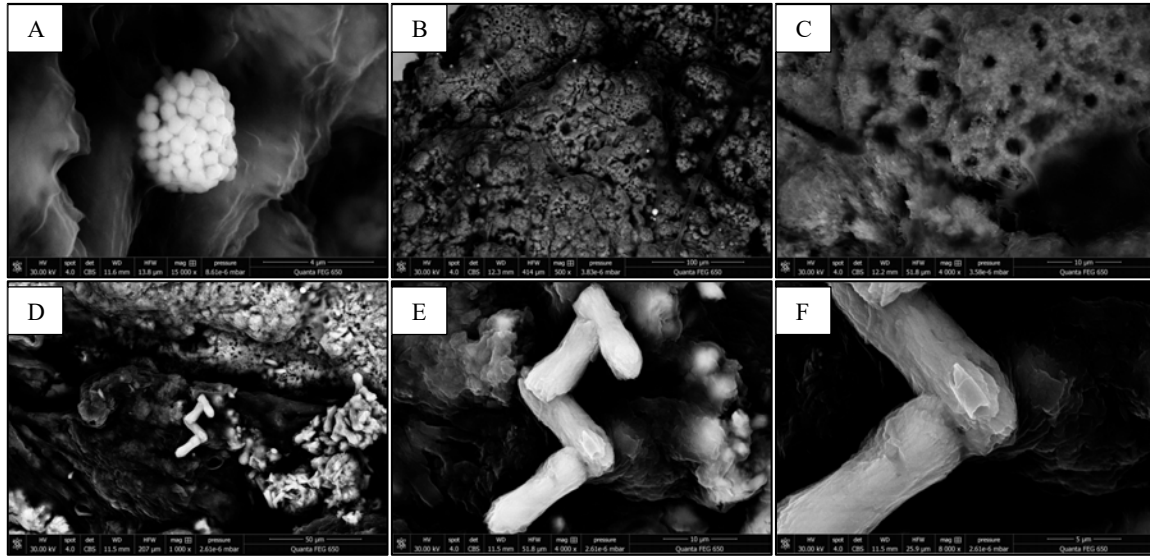


Figure 72, below: Backscatter electron images from sample S6. A) Needle gypsum bundle cross on gypsum crystal, length of needles $\sim 25 \mu\text{m}$. B) Gypsum crystal with penetrating twin, length of twin $\sim 65 \mu\text{m}$. C) Irregular carbonate 'star', size $\sim 10 \mu\text{m}$. D) Randomly distributed rods in organic material. E) Rods and starry spherulites, size $\sim 15 \mu\text{m}$. F) Close-up of starry spherulite with an adjacent small spherulite.

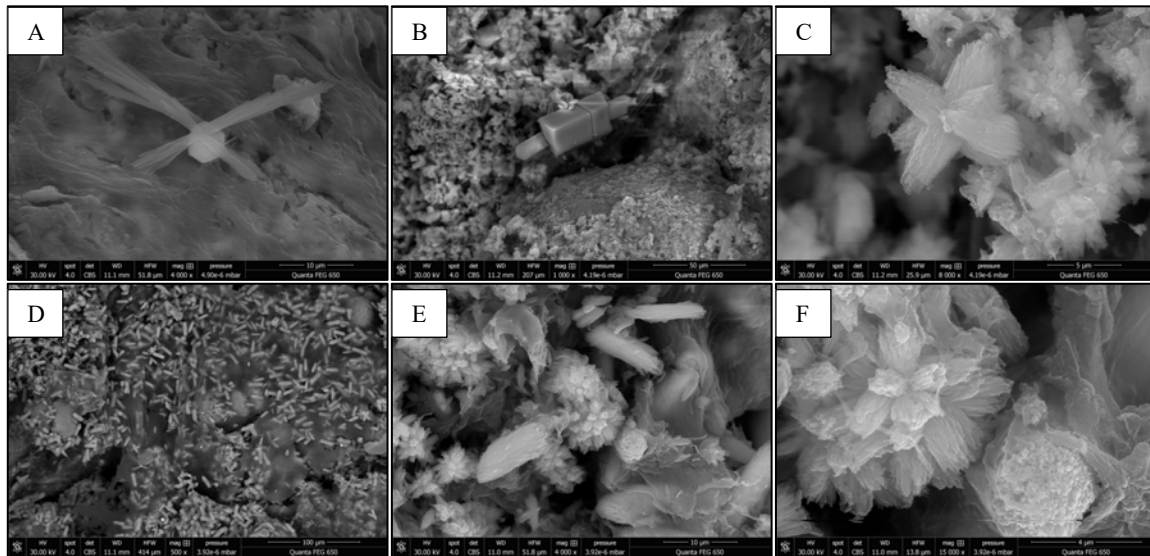


Figure 73, below: Backscatter electron images from sample S7. A) Irregularly shaped calcium carbonate rods and a spherulite with rod-like outgrowths, draped in organic material. B) Swallow-tail gypsum crystal, size $\sim 20 \mu\text{m}$. C) Another swallow-tail gypsum crystal, $\sim 15 \mu\text{m}$. D) Organic donut-shape with a framboidal pyrite sphere attached inside. E) Close-up of the framboidal pyrite sphere, size $\sim 6 \mu\text{m}$. F) Carbonate rods, two attached in the ends and two forms a small cross. Size of largest rod $\sim 20 \mu\text{m}$.

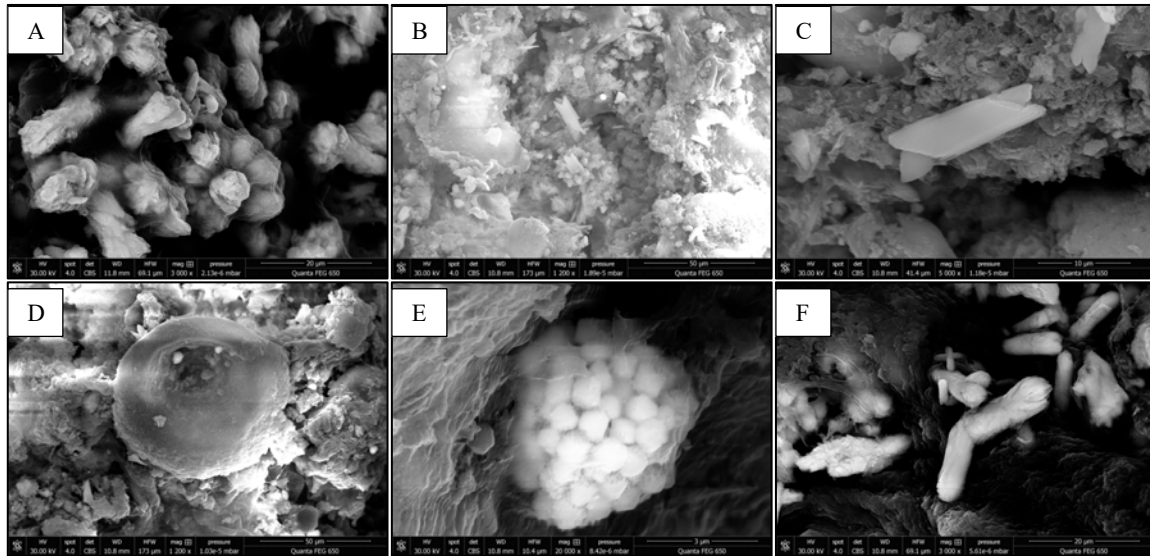


Figure 74, below: Backscatter electron images from sample S8. A) Framboidal pyrite tubes. B) Close-up of tube. C) Three framboidal pyrites on organic material (in upper part of image). D) Close-up of framboidal pyrites, size of individual crystal $\sim 3 \mu\text{m}$. E) Cluster of randomly oriented calcium carbonate rods with irregular on-growths. F) Close-up of individual rod, length $\sim 8 \mu\text{m}$. The rod is made up of very small grains of which most are aligned in the same direction, beginning to make up one whole crystal.

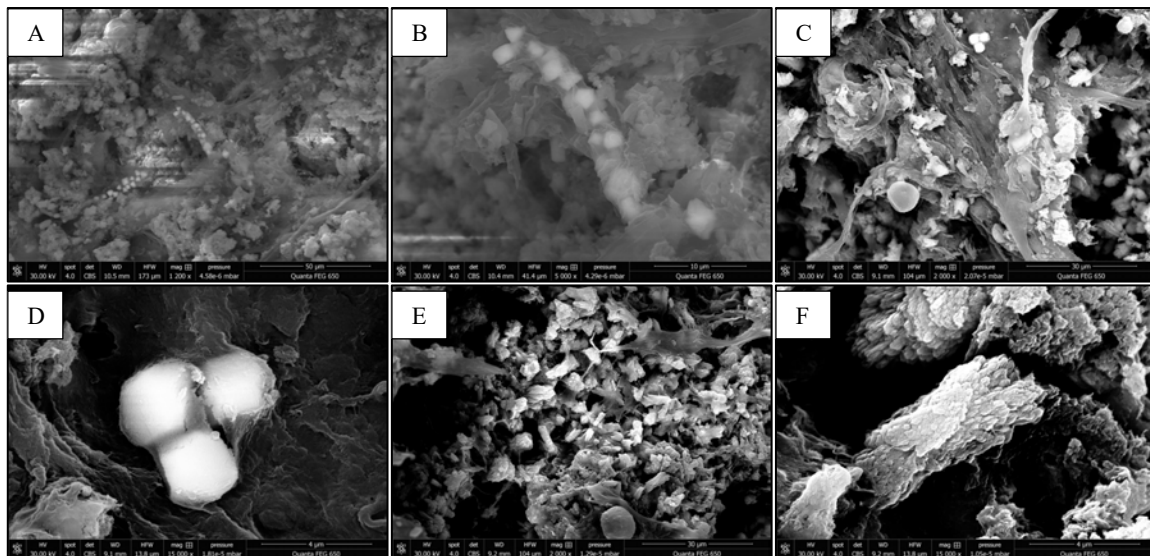


Figure 75, below: Backscatter electron images from sample S9. A) Area with dense carbonate cluster with individual crystals of various shapes. B) Carbonate cluster grains, size of grain in middle $\sim 300 \mu\text{m}$. C) Close-up of cluster grain, displaying individual rods with multiple small on-growths. D) Close-up on some of the rods, size $\sim 20 \mu\text{m}$. E) Close-up of individual rod, size of outgrowths $\sim 2 - 3 \mu\text{m}$. Close-up of rod where the outgrowths are equal in size with the dumbbell ends, making up a half spherulite, size $\sim 20 \mu\text{m}$.

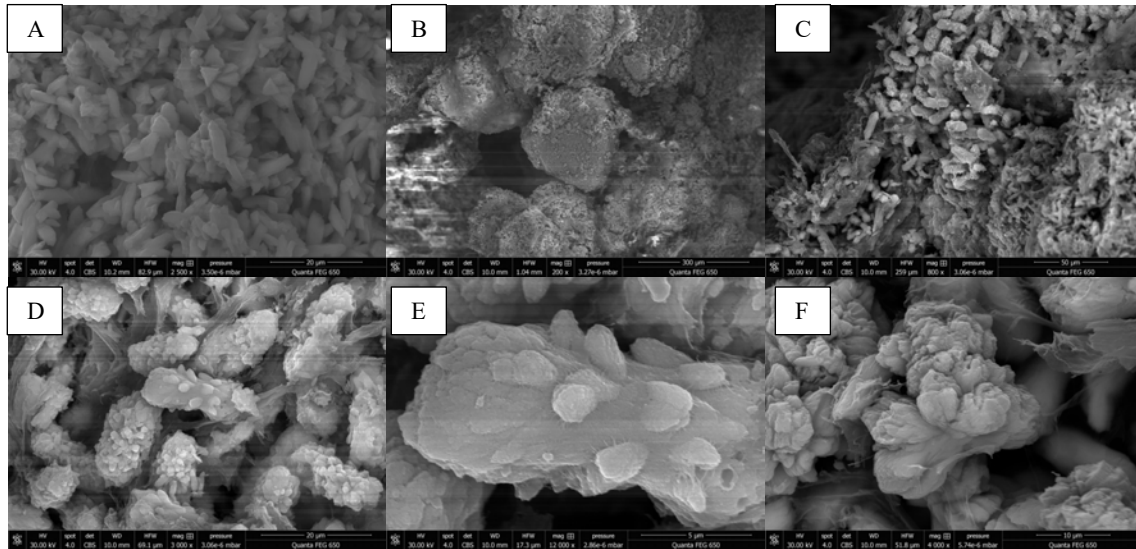


Figure 76, below: Backscatter electron images from sample S10. A) Diagonal band of organic matter (originally a horizontal mat) with individual minerals randomly distributed, above and below areas with clusters and less organic material. B) Individual calcium carbonate rods in organic matter. C) Close-up on dumbbell half and crystals with on-growths mostly buried in organic matter.

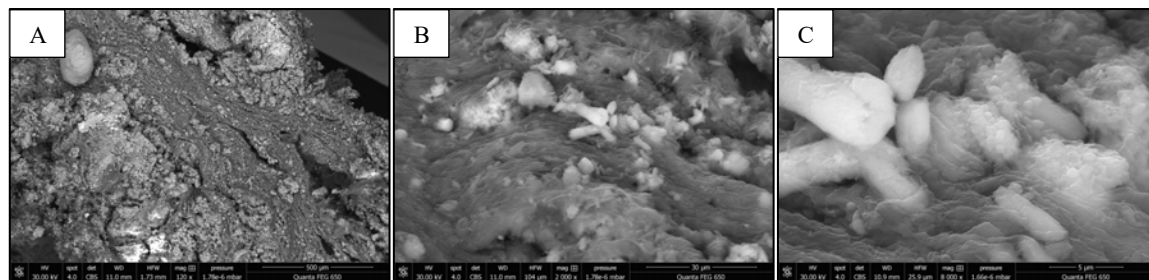


Figure 77, below: Backscatter electron images of sample S11. A) Cluster of carbonate rods. B) Close-up of double-rod with feathery endings, size $\sim 10 \mu\text{m}$. C) Close-up of feathery endings. D) Carbonate rod low density clusters around a foreign grain. E) Carbonate rods and spherulites. F) Close-up of starry spherulite comprised of small rods.

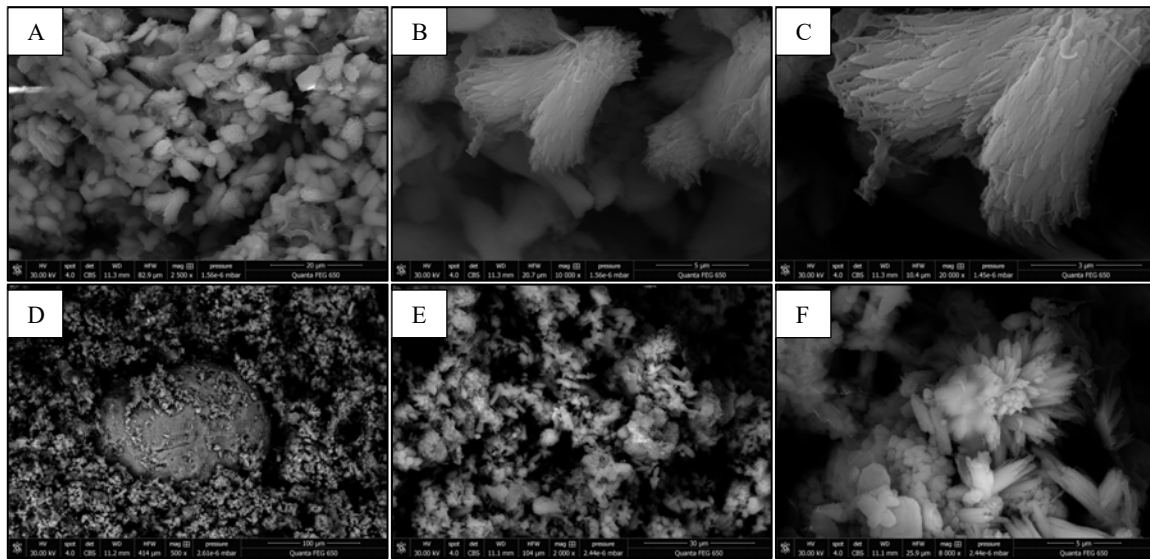
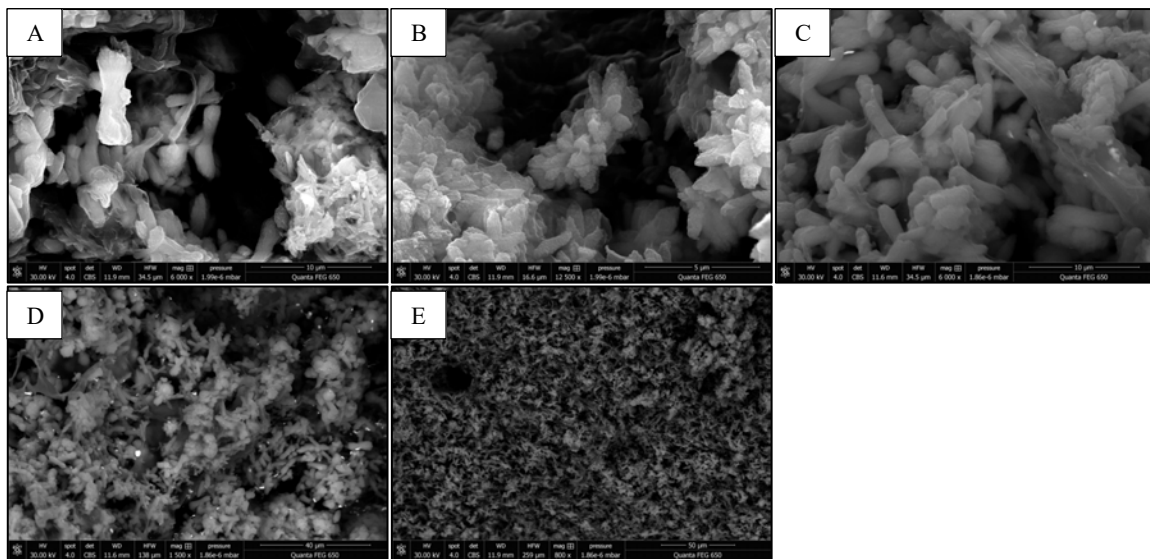


Figure 78, below: Backscatter electron images from sample S12. A) Carbonate dumbbells. B) Rod with on-growths, size $\sim 6 \mu\text{m}$. C) Cluster of small rods, size $\sim 6 \mu\text{m}$. D) Spherulites and rods, low density cluster style. E) Low density area.



The alkalinity engine

The sum of species in a solution that can be titrated with strong acid is defined as alkalinity (Gallagher et al., 2012). Total alkalinity (TA) in seawater includes ions of bicarbonate, carbonate, borate, hydroxide, phosphate and silicate (Dupraz et al., 2011) and can be calculated by equation 1 (Gallagher et al., 2012):

$$TA_{sw} = [HCO_3^-] + 2[CO_3^{2-}] + [B(OH)_4^-] + [OH^-] + [HPO_4^{2-}] + 2[PO_4^{3-}] + [H_3SiO_4^-] + [NH_3] + [HS^-] - [H^+]_{free} - [HSO_4^-] - [HF] - [H_3PO_4] \quad (Eq.1)$$

Since the concentrations of bicarbonate and carbonate are the dominant species and seawater is buffered by the carbonate system; seawater carbonate alkalinity (CA) can be used to express seawater total alkalinity, see equation 2 (Gallagher et al., 2012).

$$TA_{sw} \approx CA_{sw} = [HCO_3^-] + 2[CO_3^{2-}] \quad (Eq.2)$$

The presence of organic acids and sulfide need to be counted for in the total alkalinity of microbial mats, see equation 3 (Gallagher et al., 2012).

$$TA = CA + [\text{organic acid anions}] + [OH^-] + [HS^-] - [H^+] \quad (Eq.3)$$

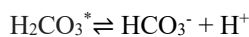
The capacity of carbonate precipitation is governed by how saturated the water is with respect to carbonate, the availability of free calcium cations and access of nucleation sites for mineral crystals to start forming. Saturation conditions are expressed by the saturation index (SI) which for carbonate includes the activity of Ca^{2+} and CO_3^{2-} , see equation 4 (Arp et al., 2001, Dupraz et al., 2009).

$$SI_{sp} = \log (IAP/K_{sp}) \quad (Eq.4)$$

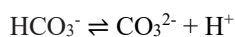
(sp = solid phase; IAP = ion activity product which is what is measured and K_{sp} = solubility product of the corresponding mineral (solid phase) which is the experimentally derived expected activity of the ions and is a number that is found in literature.)

$$\text{For calcite: } SI_{cc} = \log (\{Ca^{2+}\} \times \{CO_3^{2-}\}_{measured} / \{Ca^{2+}\} \times \{CO_3^{2-}\}_{expected}) \quad (Eq.5)$$

Activity is denoted $\{ \}$, and equals concentration multiplied with the activity coefficient (Dupraz et al., 2009). The solubility product for carbonates (K_{cc}) is dependent on the dissolved inorganic carbon (DIC) concentration (Arp et al., 2001). The DIC concentration is controlled by the partial pressure of CO_2 in the atmosphere (pCO_2) (Dupraz et al., 2009). CO_2 dissolves to form carbonic acid (H_2CO_3) in water at a certain proportion governed by Henry's law and is temperature- and pressure-dependent; lower T and higher P \rightarrow more CO_2 dissolved (Dupraz et al., 2009). The carbonate equilibrium is dependent on pH and salinity:



$$(pK 5.9 \text{ at } 25^\circ\text{C, 1 bar atmospheric pressure and 35 PSU salinity}) \quad (Eq.6)$$



(pK 8.9 at 25°C, 1 bar atmospheric pressure and 35 PSU salinity)

(Eq.7)

Supersaturation for ions in solution is achieved when $IAP > K_{sp}$ (i.e. $SI > 0$). At 25°C, 1 bar atmospheric pressure and 35 PSU salinity (seawater), the solubility product (K_{sp}) for calcite is $10^{-6.37}$ and for aragonite $10^{-6.19}$ (Dupraz et al., 2009).

From measurements of 9.5-15-fold supersaturation in present day calcifying cyanobacterial biofilms, an approximate 10-fold supersaturation for $CaCO_3$ of the ambient water in non-marine settings can be considered required ($SI_{Cc}=1.0$) for cyanobacterial calcification (Arp et al., 2001).

Removal of CO_2 promotes precipitation of $CaCO_3$ where sufficient free calcium is available by driving the buffering equation of carbonate to the right, see equation 8 (Dupraz et al., 2011).



CO_2 removal can occur abiotically by degassing, for example at cascades and waterfalls, but can also be affected by photosynthesis (Dupraz et al., 2011). Disproportionation of bicarbonate where photosynthesizing organisms fix CO_2 lead to increased CO_3^{2-} concentration promoting carbonate precipitation, provided that free calcium is available (Arp et al., 2001):



The SI equation show that an increase of carbonate ions will make the IAP greater than the K_{Cc} . Since K is depending on the initial DIC, the lower DIC is to start with, the greater impact CO_2 removal make SI (Arp et al., 2001).

Different types of metabolism have either a positive or negative effect on carbonate saturation index (Visscher & Stolz, 2005). A brief summary on the effects of metabolic processes on carbonate precipitation states that photosynthesis and sulfate reduction are processes that increase SI while aerobic heterotrophy, sulfide oxidation and fermentation decrease SI (Dupraz et al., 2009). However, the need of oxygen by aerobic heterotrophs requires close proximity to where and when oxygen is produced by photoautotrophs, causing the carbonate precipitation promoting effect of photosynthesis to be neutralized by the dissolutive effect of aerobic respiration (Visscher & Stolz, 2005). In the case of the couple of sulfate reduction and sulfide oxidation there is no such need for proximity, which allows for local areas of precipitation where sulfate reduction prevails (Visscher & Stolz, 2005). Further details on the metabolic processes are referred to Dupraz et al. 2009 and Visscher & Stolz, 2005.

The binding capacity of the organic matrix is initially inhibiting carbonate precipitation by making calcium non-available (Dupraz et al., 2011). When the EPS is degraded by heterotrophs, bound Ca^{2+} is released and inorganic carbon is produced; that is bicarbonate ions in normal seawater pH (Dupraz et al., 2011) The freed calcium and increased alkalinity raise the local carbonate saturation index, promoting carbonate precipitation (Dupraz et al., 2011).

Islay freshwater stromatolite

Islay is an island located outside the west coast of Scotland, 55°48'41.91"N 6°27'24.73"W (Fig. 1). The climate is mild, with an average annual temperature of 6-12 °C (see Fig. 2 for monthly averages and Table 1 for annual climate averages 1981-2010).



Figure 79: A) Inset showing the location of Islay on the west coast of Scotland. B) Location of Saligo Bay on Islay (Google Earth).

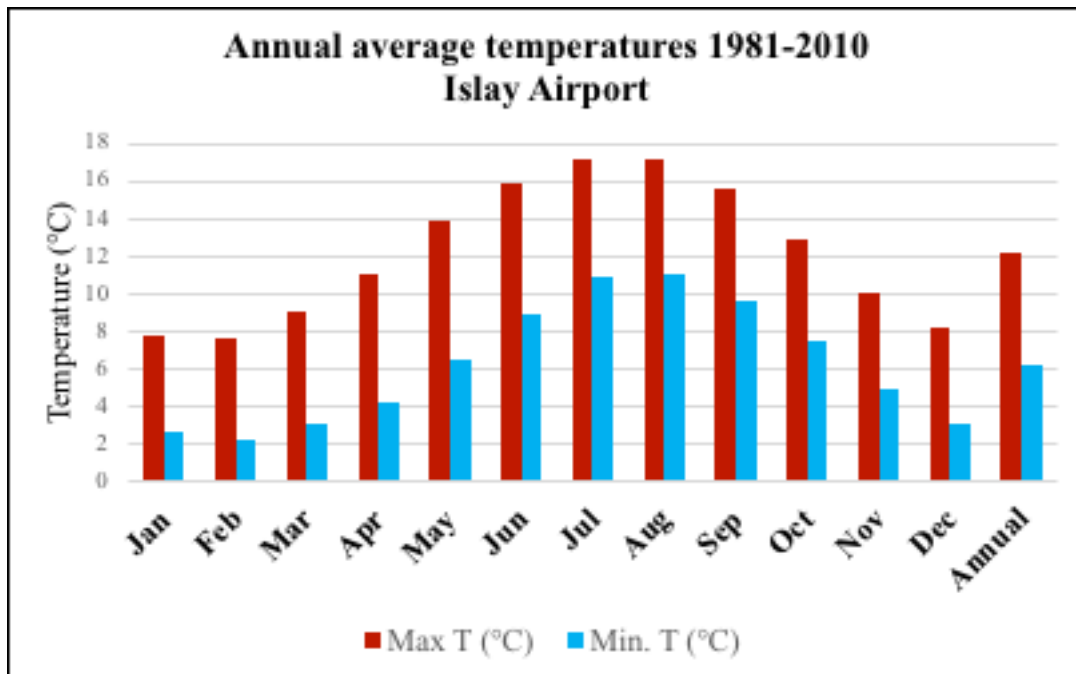


Figure 80: Average maximum and minimum temperatures for each month and annually 1981-2010. Data from Metoffice (2019).

Table 1: 1981-2010 climate averages at Islay Airport climate station (Metoffice 2019).

Month	Max. temp (°C)	Min. temp (°C)	Days of air frost	Rainfall (mm)	Days of rainfall ≥ 1 mm/day	Mean wind speed at 10m (knots)
Jan	7,8	2,6	6,7	138,2	19,9	15,2
Feb	7,6	2,2	6,7	98,2	14,8	14,4
Mar	9,1	3,1	4,8	118,8	17,8	14
Apr	11	4,2	2,6	77,9	13,3	12,2
May	13,9	6,4	0,5	62,4	11,6	11,8
Jun	15,8	8,9	0	73,3	11,4	10,5
Jul	17,1	10,9	0	78,8	13,8	10,1
Aug	17,1	11	0	106,7	15,4	10,4
Sep	15,6	9,6	0	114,6	15,5	11,7
Oct	12,9	7,5	0,9	148,7	19,7	13,2
Nov	10	4,9	3,1	132,3	19,3	13,7
Dec	8,2	3	6,5	132,9	18,6	13,4
Annual	12,2	6,2	31,9	1282,7	191,1	12,5

Depressions on the cliffs at the beach of Saligo Bay, western Islay, collect groundwater from the area above in two narrow and shallow pools before the water runs out on the beach. In these small pools, cyanobacterial microbial mats form miniature stromatolites. A travertine deposit showing an almost vertical morphology has developed at the outlet of the lower pool. Hand samples torn away from the deposit show beautiful microbial mat lamination (Fig. 2). The cliffs, where the pools are located, are 1-2 m high and the stromatolite pool is approximately 3 m long, no more than 1 m at its widest part and approximately 5 cm deep. The bedrock is 750 My old metamorphosed turbidites that are strongly folded and hosts abundant joint-filling calcite veins. The ocean shore is only 10-20 m away from the cliff and there is sand in the pools that has been transported by the waves or the wind on the cliff.



Figure 81: The cliffs at Saligo Bay where the two pools run out on the beach. The pool surfaces are marked out with blue arrows. The red dashed line marks the outlines of the travertine/microbial mat deposit at the outlet of the lower pool. The white inset mark the position of the right image where a piece of the deposit is torn away, showing crude vertical lamination.

In the higher pool the stromatolites grow mainly along the edges with some exception where isolated miniature “reefs” grow. The surface of the mat is knobby and displays horizontal lamination in cross-section. In the lower pool microbial mats cover the bottom and display “snakelike” ridges (Fig. 4).



Figure 82: Beach view from the outlet of the lower pool (left) with snakelike microbial mat ridges on the bottom and knobby stromatolitic microbial mats growing along the edges in the higher pool (right).

One piece of the knobby mats that had been torn away from the edge was found upside down in the sandy bottom of the higher pool, see figure 5. This piece was brought back as a sample to Stockholm University.



Figure 83: The knobby stromatolitic microbial mats in the upper pool with a torn off piece upside down in the middle (left); close-up on the torn-off piece that got brought back to Stockholm University together with an in situ right-side-up piece (middle); the area along the close side have several pieces torn off, close-up of area with missing piece to the right.

The large torn-off piece was approximately 10 x 7 cm. The knobs are growing irregularly and show a lamination that is very distinct, especially in the topmost layers. The average thickness of the stromatolite is approximately 7 mm with altering green and yellowish white laminae. The lowest green layer is very dark, the middle is light green and also display vague perpendicular features. The surface is brown-green and has a mossy appearance. The piece is coherent and has a leathery feeling when being handled. Figure 6 shows images of the piece from below, above, torn side and cut side view.



Figure 84: The torn-off piece from below in the field (top left) and sideview (bottom left) where horizontal lamination and perpendicular features are seen. View from above in the laboratory at Stockholm University (top right) and cut sideview (bottom right) where the horizontal lamination appears more distinct than in the torn view.

Sample preparation

A cross-section sample was cut out through the microbial mat lamination into an approximately 7 x 10 x 2 mm piece. Another approximately 5 x 5 cm piece was cut off, embedded in agar, covered with water and exposed under UV-light in the laboratory for future analyses. Subsamples were prepared for scanning electron microscope analysis using chemical drying. A series of alcohol baths (50%, 70%, 80%, 90%, 95%, and 100%) was used to progressively replace the water in the samples in order to preserve as much as possible the original morphology of the sample. Before imaging, the sample was placed in a final bath of tetramethylsilane (TMS), followed by full evaporation under fume hood. The sample was mounted on a stub with silver paint and gold coated.

SEM analysis and results

The chemically dried sample was analyzed using a Scanning Electron Microscope Quanta FEG 650 equipped with an Oxford instruments X-max backscatter electron (BSE) CBS detector at the Department of Geological Sciences, Stockholm University. The software used was AZTEC. The sample was imaged in high vacuum, with accelerating voltage 30.00 kV and chemically analyzed using an X-Max Large Area EDS Silicon Drift Detector from Oxford equipped with the AZtecOne EDS software.

The SEM analysis showed that the yellowish white laminae consists of calcium carbonate. The green laminae are filamentous cyanobacteria. A few trapped sand grains of silica and of other composition are randomly dispersed in the laminae sequence. Morphology of the precipitates follows the morphology of the cyanobacteria. The cyanobacteria often display a vertical or semi-vertical orientation. The sample display an alternation between layers with high and low carbonate content. The carbonate nucleates within the organic material. It displays various microstructures: no visible crystalline structure on micrometer scale, and a microcrystalline, elongate or rhombic precipitation style. The individual rhombic crystals are around 1 micrometer. The precipitates form around the bacteria filaments and form aggregates. Figures 7 to 14 display backscatter electron images where some of the observed features are marked out. The composition of carbonate is similar in all analyzed aggregates; with approximately 67 wt% Ca, 31 wt% O and 2 wt% Mg. Table 2 presents normalized wt% of calcium, oxygen and magnesium in seven different calcium carbonate aggregates. The distribution of Ca, C, O, Si, S, P and Mg in a part of the sample is presented in figure 15.

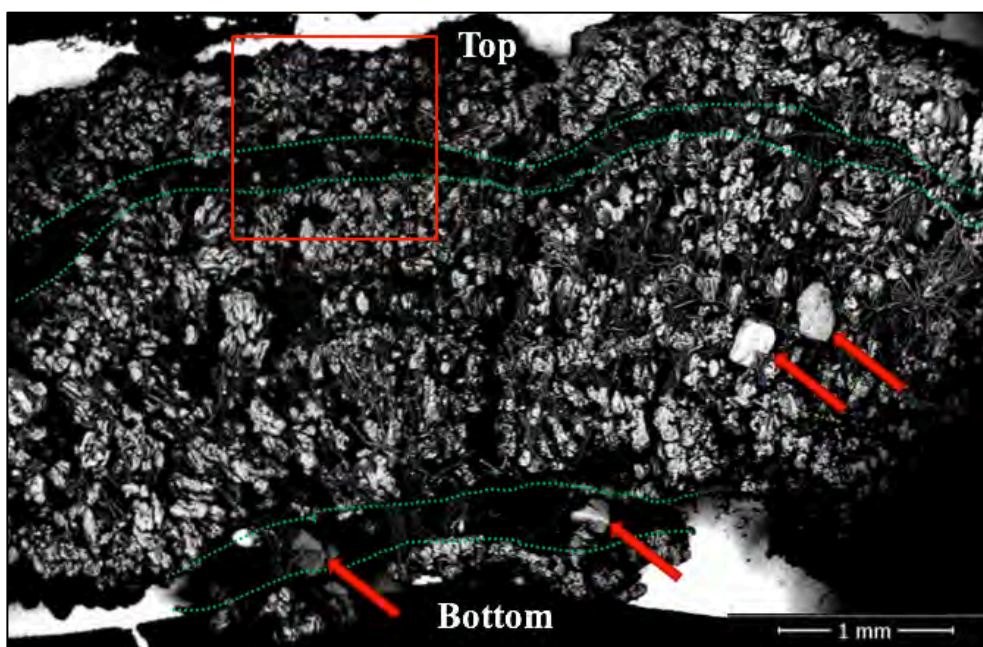


Figure 85: Backscatter electron image of the crosscut and chemically dried stromatolite sample. Note that the original thickness of the sample was approximately twice that of the chemically dried sample which is now 3 mm thick at the thickest part. Red arrows mark sand grains. Green dashed lines mark out two laminae with distinctly lower calcium carbonate content. The red frame marks the location of figure 8, the yellow frame marks the position of figure 11 and the green frame marks the position of figure 13. The majority of the light-colored features that are smaller than the sand grains are carbonate. The thread-like features are cyanobacteria.

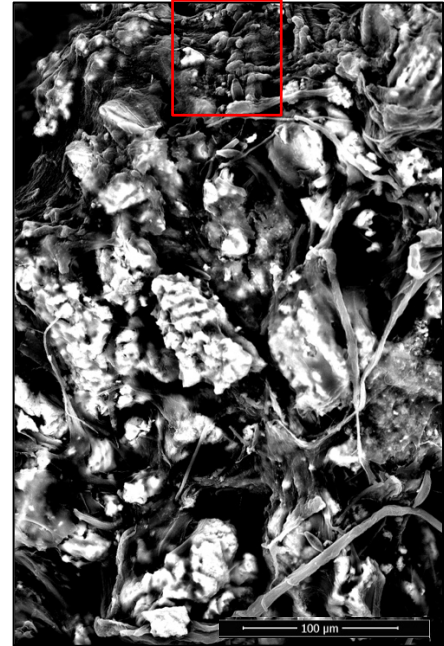
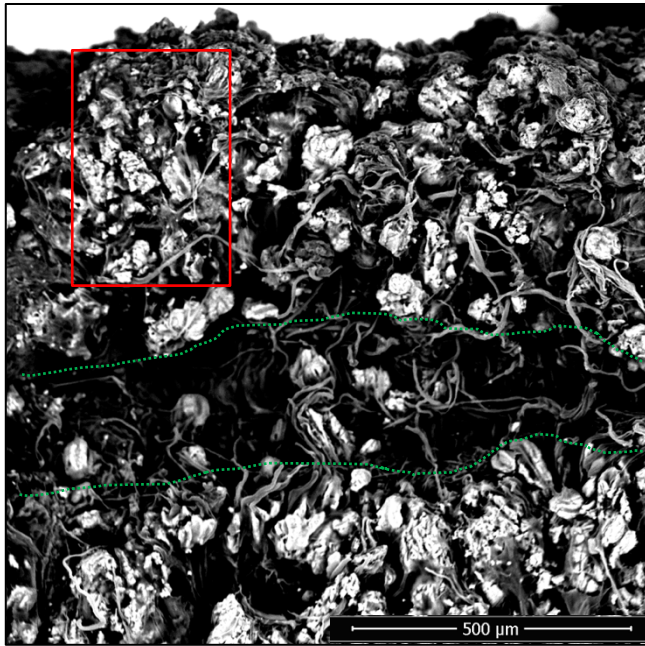


Figure 86: Top 1 mm of the sample (left). Dashed green lines mark the upper of the two marked layers with low density of calcium carbonate. Much of this area in the chemically dried sample consists of empty space. The red frame in the left image marks out the position of the right image. The red frame in the right image marks out the position of figure 9.

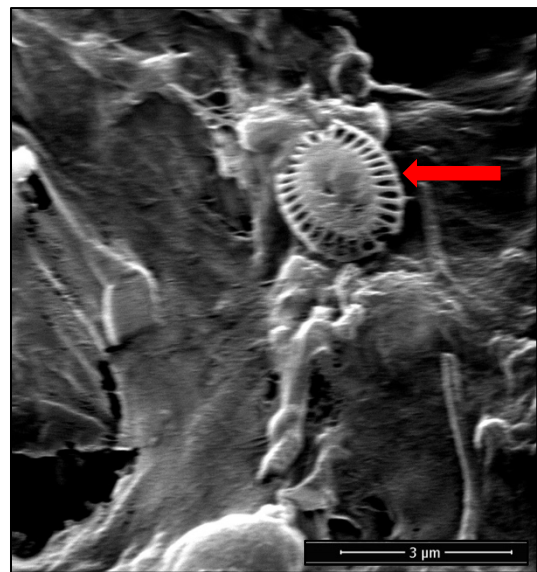
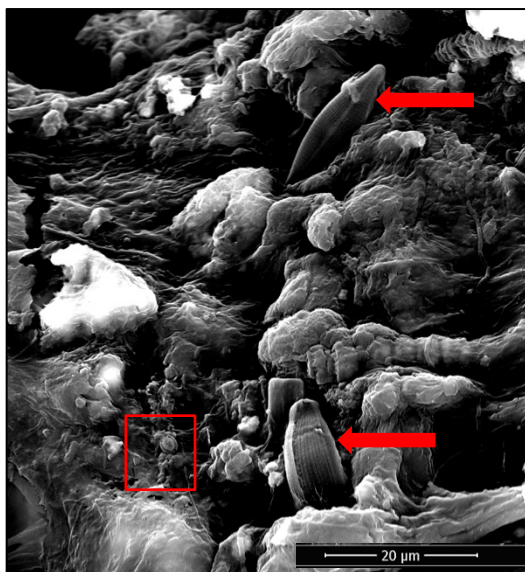


Figure 87: Red arrows mark out diatoms in the top part of the stromatolite. Red frame in left image marks the position of the right image, displaying a smaller diatom.

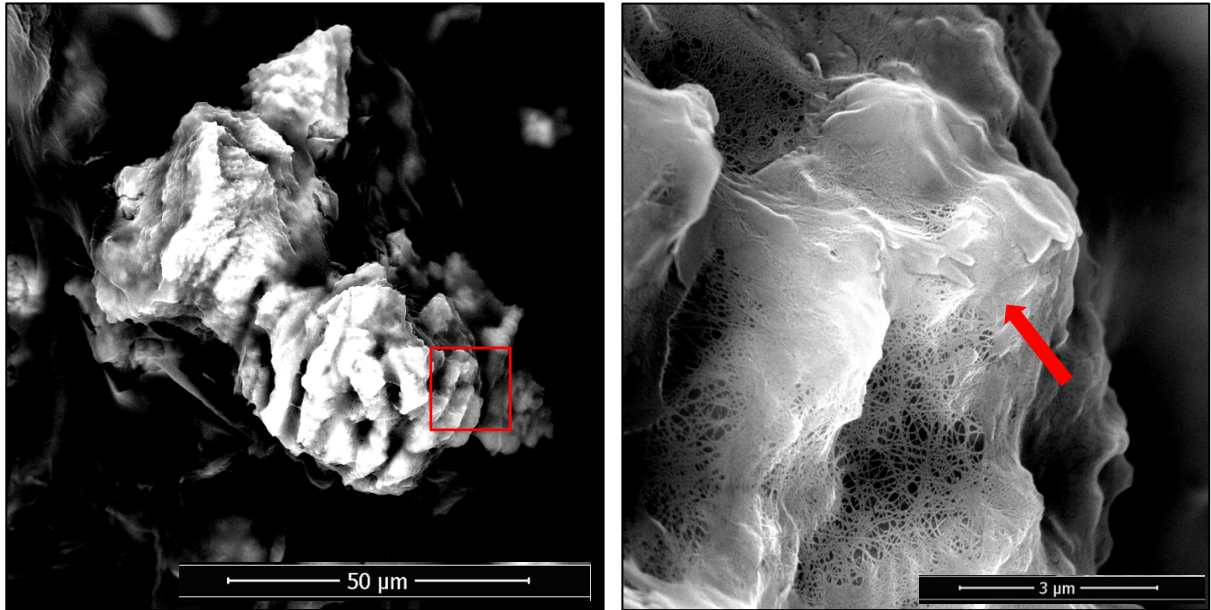


Figure 88: A calcium carbonate aggregate with elongate pattern. The red frame shows the position of the right image, an enlargement of the calcium carbonate precipitate which is draped in a network of organic material. The precipitate has some vague elongate shapes (marked with red arrow) but otherwise no visible crystal structure in micrometer scale.

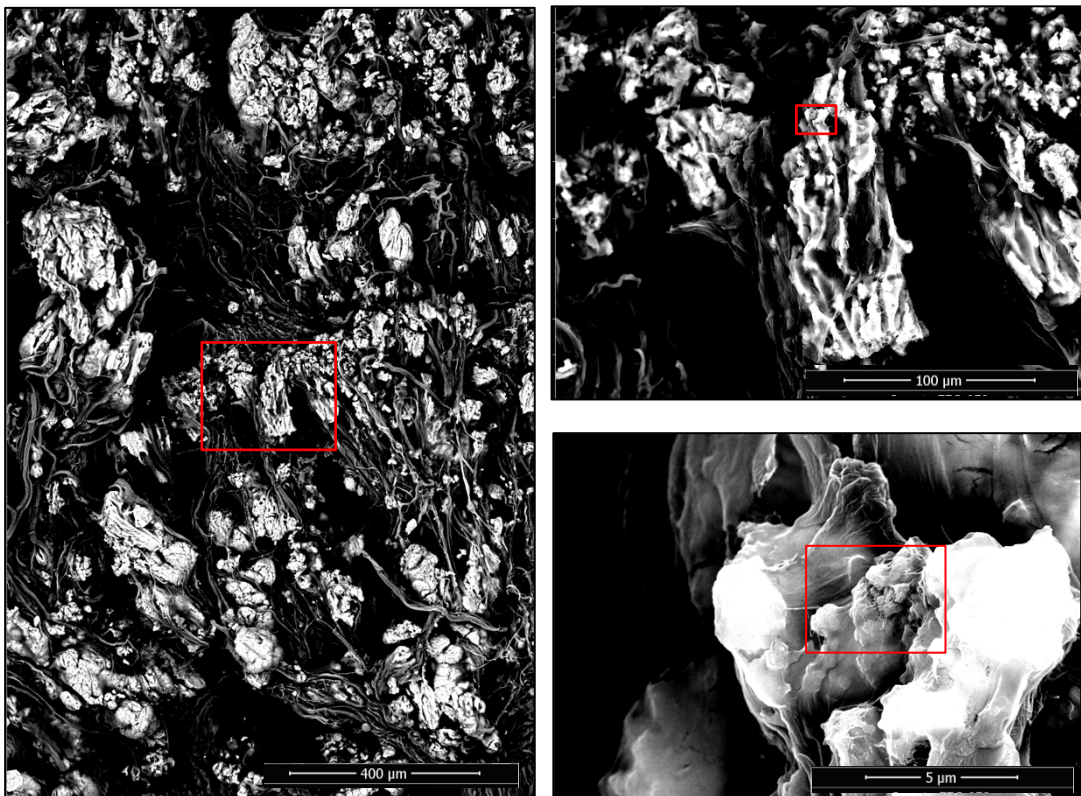


Figure 89: Middle part of stromatolite (left). Red frame in left image marks position of upper right image, red frame in upper right image marks the position of lower right image. Red frame in lower right image marks the position of figure 12.

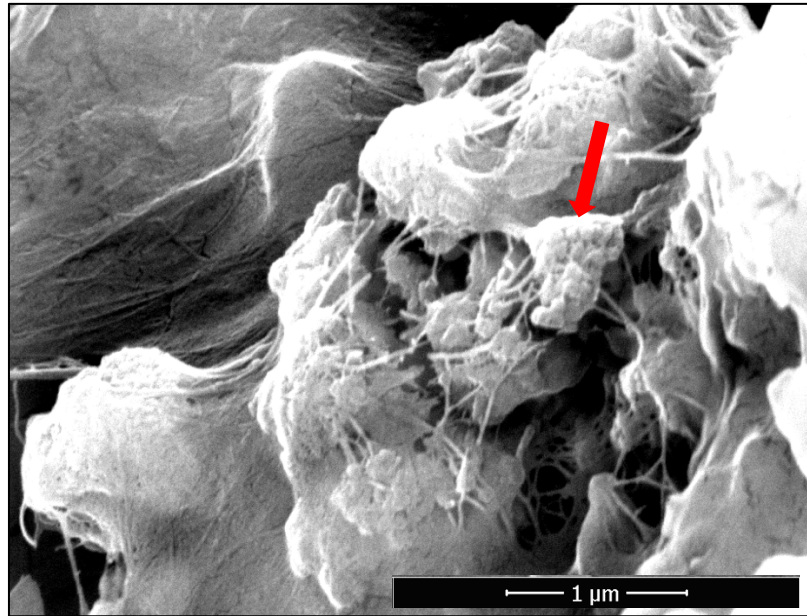


Figure 90: Close-up of calcium carbonate precipitate. The red arrow marks out an area with nanoscale grain cluster.

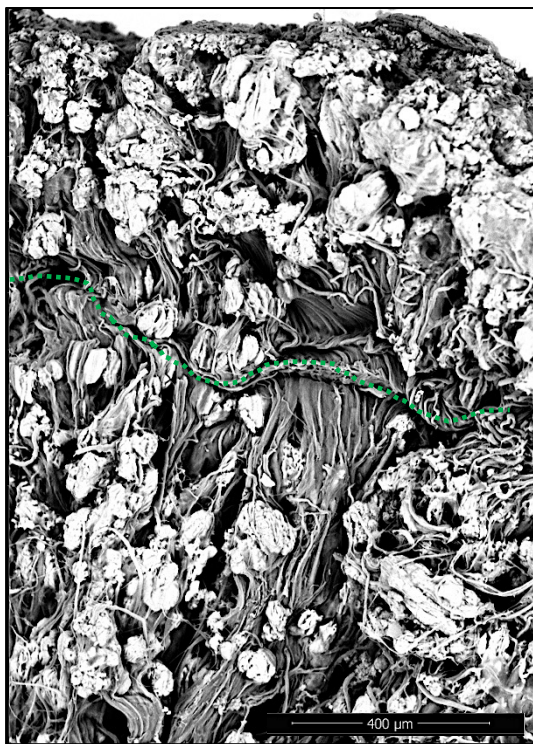


Figure 91, left: Cyanobacteria with a mainly vertical alignment that seem interrupted horizontally, marked by green dashed line. Aggregates of calcium carbonate enclose parts of the cyanobacteria. Right: Aggregate with vertical alignment. Individual crystals can be distinguished within the organic material.



Figure 92: Filamentous cyanobacteria with walls of calcium carbonate precipitate. Red frame marks position of the image to the right. In the close-up to the right, individual rhombic crystals can be seen along the edge.

CaCO ₃	Ca (wt%)	O (wt%)	Mg (wt%)
Aggregate 1	67,4	30,5	2,1
Aggregate 2	67,3	30,8	1,9
Aggregate 3	68,2	30,1	1,7
Aggretate 4	65,2	33,3	1,5
Aggregate 5	67,6	30,7	1,7
Aggregate 6	66,7	32,2	1,1
Aggretate 7	68,0	30,3	1,7

Table 2: Normalized wt% values of Ca, O and Mg in seven different calcium carbonate aggregates. All aggregates have similar composition with approximately 67 wt% calcium, 31 wt% oxygen and 2 wt% Mg.

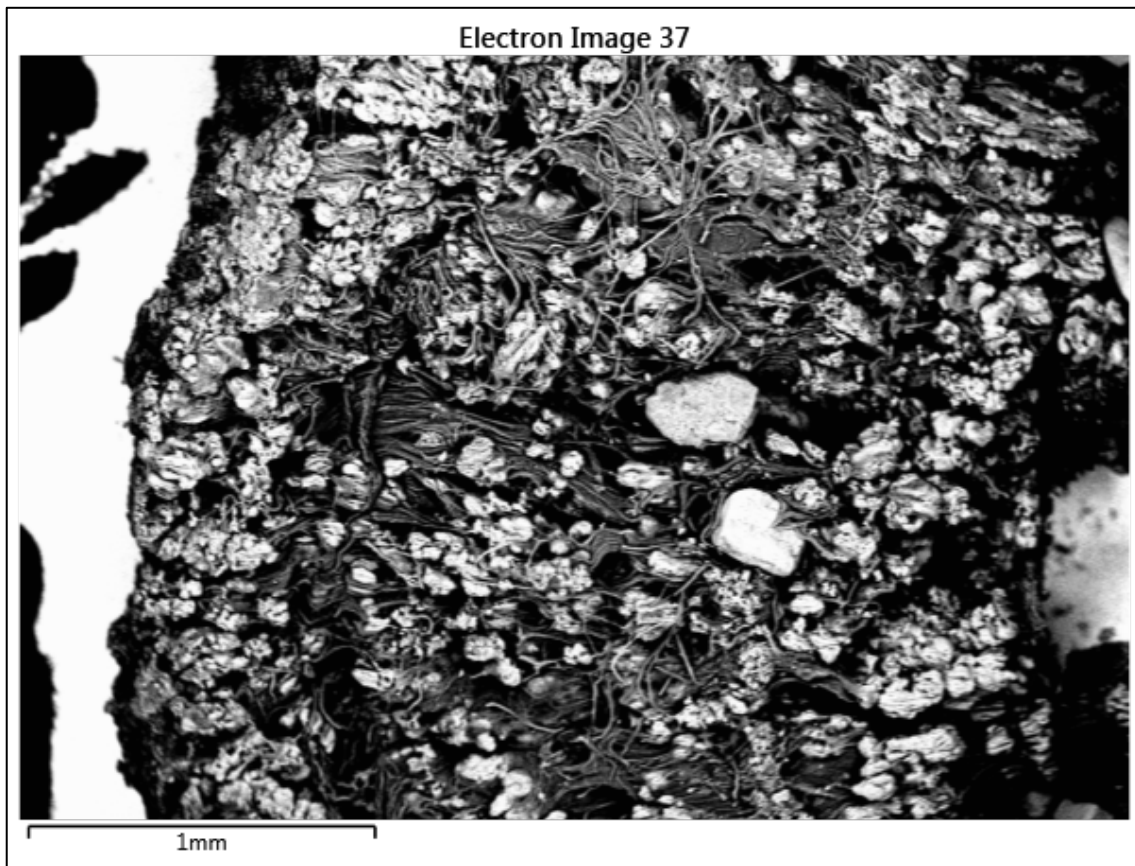
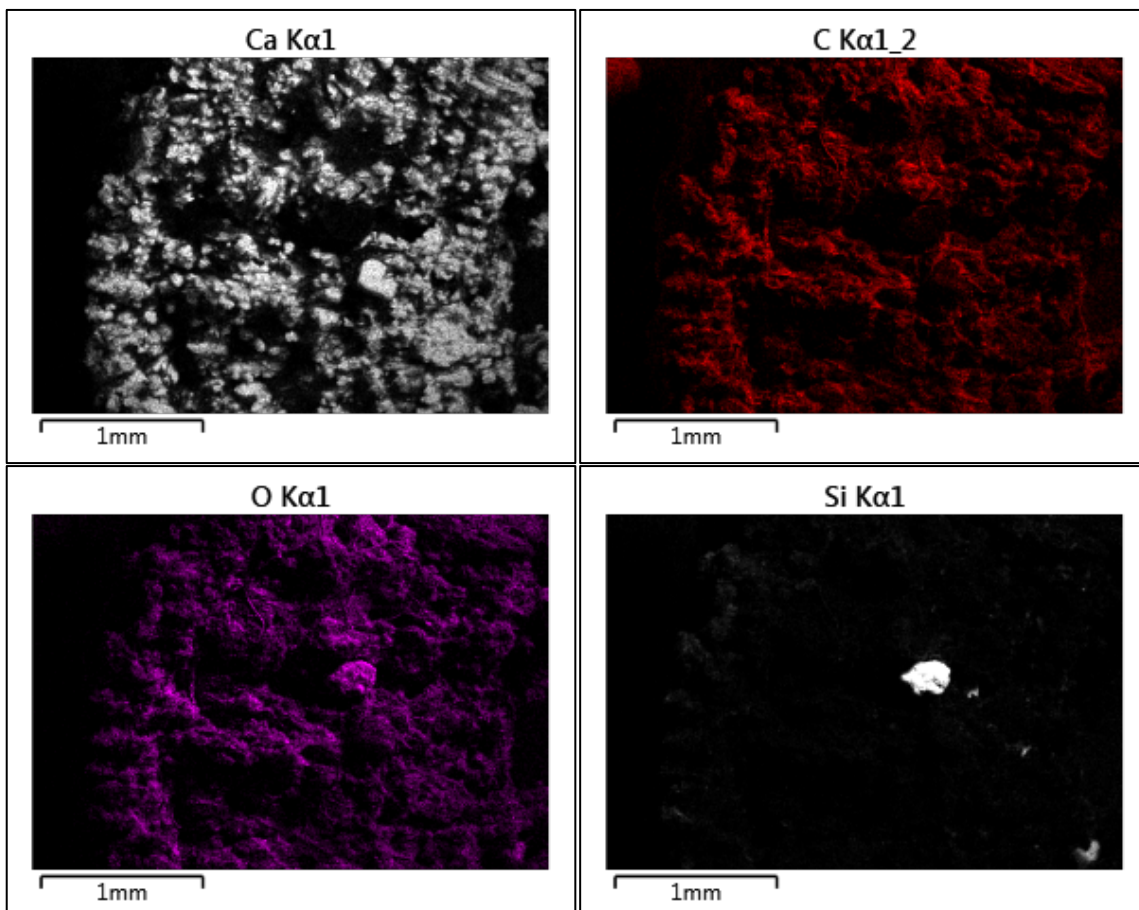
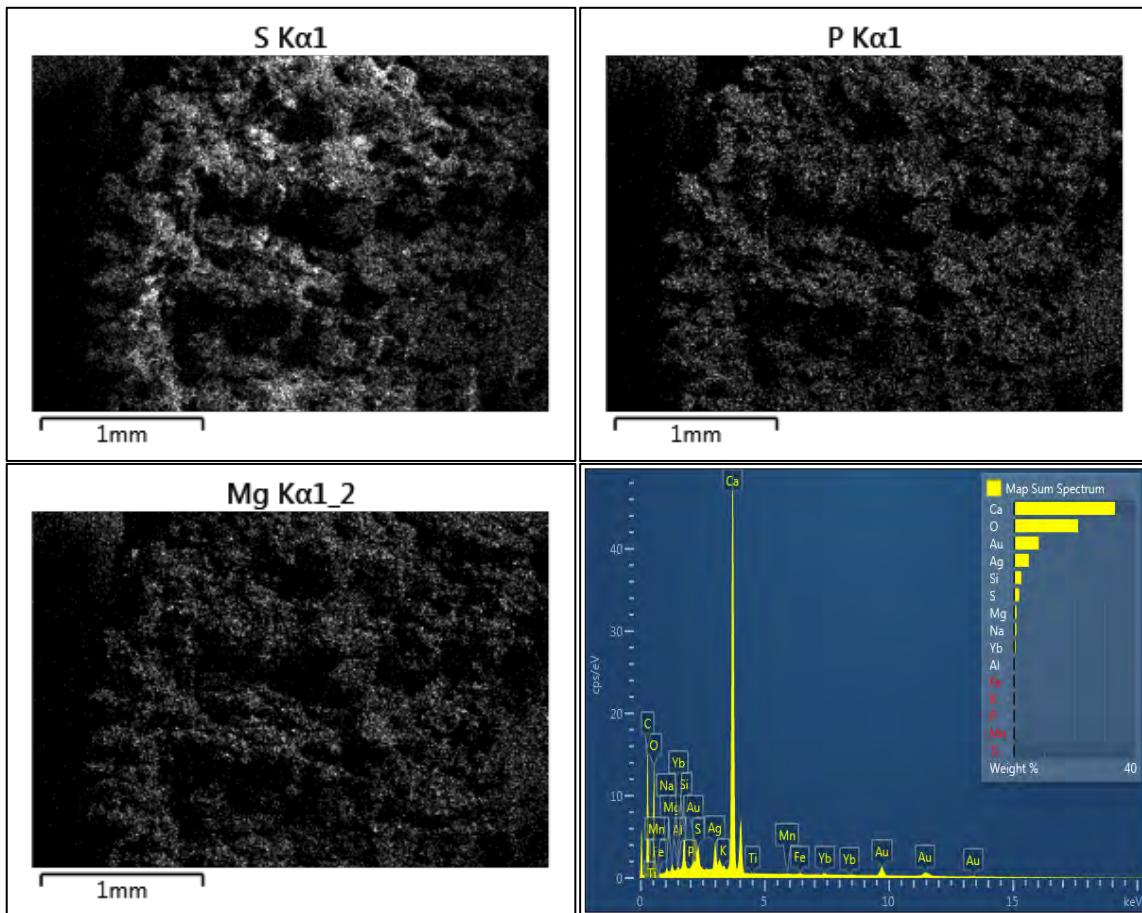


Figure 93, above: The stromatolite in profile, top to the left and bottom to the right. Below: Maps of Ca, C, O, Si, S, P, Mg and map sum spectrum.





References, Islay Freshwater Stromatolite

Google Earth (2019) accessed 2019-05-02

Metoffice (2019) <https://www.metoffice.gov.uk/public/weather/climate/gcgc8kt2> accessed 2019-05-02